Solid-State Electrochemical Protonation/Redox Reaction Induced Control of Physical Properties of $SrCoO_x$ and $SrFeO_x$

Qian Yang

Thesis submitted as a requirement for the degree of Doctor of Philosophy

in the field of Engineering

Graduate School of Information Science and Technology

Hokkaido University

March 2022

Table of Contents

List of Figures

List of Table

List of Acronyms

ReRAM	Resistive random access memory
LRS	Low resistance state
HRS	High resistance state
TMOs	Transition metal oxides
PLD	Pulsed laser deposition
CAN	Mesoporous amorphous $12CaO \cdot 7Al_2O_3$
YSZ	Yttria-stabilized zirconia
GDC	Gd-doped CeO_2
BM	Brownmillerite
PV	Perovskite
PVD	Physical vapor deposition
RHEED	Reflection high-energy electron diffraction
XRD	X-ray diffraction
HRXRD	High-resolution X-ray diffraction
XRR	X-ray reflectivity
FWHM	Full width half maximum
HAADF	High-angle annular dark-field
STEM	Scanning transmission electron microscopy
ADF	Annular dark-field
LAADF	Low-angle annular dark-field
EELS	Electron energy-loss spectroscopy
EDS	Energy dispersive spectroscopy
AFM	Atomic force microscopy
UV-VIS-NIR	Ultraviolet-visible-near infrared
XPS	X-ray photoelectron spectroscopy

XAS	X-ray absorption spectroscopy
DOS	Density of states
DFT	Density functional theory
TEMF	Thermo-electromotive force
RSM	Reciprocal space mapping
EY	Electron yield
T_A	Annealing temperatures
SIMS	Secondary ion mass spectrometry

List of Symbols

S	Thermopower
λ	Wavelength of the X-ray
n	Diffraction order
d_{hkl}	Interplanar distance
θ	Diffraction angle
ω	Incident angle in out-of-plane direction
2θ	Diffraction angle in out-of-plane direction
φ and χ	Euler angles in-plane direction
Z	Atomic number
α	Absorption coefficient
E_{F}	Fermi energy
k_{B}	Boltzmann constant
e	Electron charge
n	Carrier concentration
μ	Carrier mobility
ΔT	Temperature difference
ΔV	Thermo-electromotive force, TEMF
R	Sheet resistance
ρ	Resistivity
f	Geometrical factors
t	Film thickness
T_{c}	Transition temperature
J	Current density
y	Conversion rate
ϕ	Conversion rate

ϕ_c	Percolation threshold
D	Grain size
Q	Electron density
I	Current
V	Volume
E_a	Activation energy

Chapter 1. General Introduction

1.1 Background of this study

Due to the rapid advancement of information technology in recent years, the era of data is imminent to human society. Nowadays, computers and smartphones have become smaller and faster as the transistors became more efficient. This is well-reflected in the Moore's law, stating that the number of transistors in an integrated circuit doubles every two years. Accordingly, the demand for data-storage memory with high performance is exponentially increasing.

Memory can be classified into two types: volatile and non-volatile memory devices. Volatile memory devices retain the information only when the power is continually supplied. Otherwise, they will lose the stored data. Since continual supply of power comes with power consumption and instability, their application is limited to calculations.[1,2] Therefore, the non-volatile data-storage memory device is essential for practical storage applications since they can keep the information even without an active power source.[3-5] Among the non-volatile data-storage memory devices, flash memory[6] and resistive random access memory (ReRAM)[7] are explored intensively due to their low operation power and scalability. The market size of non-volatile memory devices is increasing year by year (**Figure 1-1**), worth USD 73 billion in 2020 and is expected to reach USD 120 billion in 2026.[8]

Flash memory, a type of floating-gate memory invented by Toshiba in 1980, is widely used for data storage in electronics today as it makes the devices compatible with electrical erasing and rewriting ability.[9] Flash memory is faster and more reliable than other non-volatile memory devices since it can erase data in blocks rather than by individual bits. There are two common flash memories: NOR and NAND Flash.[3,10,11] NOR Flash has lower density and is the component of cell phones. In contrast, NAND Flash offers higher density, which is suitable for different applications such as USB drives.

However, one limitation of floating-gate flash memory is the charge retention issue, of which the mechanisms have been widely investigated.[12-14] One mechanism is the stored charge leak out from the floating gate through the gate oxide or interpoly dielectrics, leading to data reliability problems.[14] Therefore, non-charge based memory like ReRAM that utilizes resistance change instead of charge for storing the information became attractive due to its leakage-free aspect and more scalable features. ReRAM [7,15-17] is operated by modulating the resistance of active layers like metal oxides, where the metal oxides can be electrically controlled from an insulator to a conductor through the formation of a filament or conductive path by applying a voltage. For the formation of conductive filament, there are different mechanisms like the migration of oxygen vacancy or metal ions. When the conductive filament arises and connects to the electrode, a low resistance state (LRS) is obtained. Conversely, a high resistance state (HRS) is formed with the dissolution of the filament.[18] Due to its simple structure and data reliability,

ReRAM is regarded as a better alternative for flash memory. Nevertheless, the lack of high-precision assembly in fabrication and the high bit error rate caused by random switching of produced ReRAM devices still cannot meet the industry standards for applications like automotives and smart devices.[19,20]

Both the flash memory and ReRAM use electric charge to encode data, and therefore, suffer from issues associated with controlling charge. In this regard, some advanced memory devices such as the electrochromic device use the optical property instead,[21-23] while spintronic devices use the intrinsic spin of electrons.[24-26] The coexistence and cross-coupling between these functional properties extend the potential of advanced memory devices by storing information as changes in electrical, optical, and magnetic properties as illustrated in **Figure 1-2**. For example, smart windows based on electrochromic devices have already been applied to airplane windows (Boeing 787 Dreamliner) as the electronic curtain utilizing electrochemical control of color change from transparent to opaque, which is significantly advanced compared to the traditional pull-down window. Tungsten trioxide (WO_3) is the most famous active material for electrochromic devices for this application, which exhibits a reversibly switchable color transition from colorless transparent insulator to blue conductor with protonation/deprotonation (H^+).[27] WO_3 is an example of transition metal oxides (TMOs) utilized in advanced memory applications. TMOs, as one of the advanced materials, are composed of transition metal (TM) and oxide ions. The valence versatility of the metal ions from non-stoichiometry (associated

with the formation of defects) or stoichiometry of oxide ions can induce variations in functional properties. This phenomenon is attributed to the outer d electrons. Electron gain or loss in d orbitals cause a significant difference in the electronic structure of TMOs, which can even change the preferred crystal structures. Through controlling the crystal structure, TMOs exhibit a rich variety of magnetic, electrical, and optical properties. Thus, TMOs show an excellent potential for application in advanced memory devices. In fact, TMOs that exhibit electrical, superconducting, and magnetic switching phenomena, have been studied for advanced applications.[28-31]

1.2 Defect engineering in TMOs for memory applications

In general, defects significantly affect the physical properties of materials. This is especially common in TMO systems. Controlling the oxygen vacancy is the most common approach, but in addition to oxygen vacancies, Li^+, H^+, and Na^+ ions also can be inserted or removed from the lattice of TMOs to tune their crystal structure and functional properties.[32-36] To trigger such transitions, chemical or electrochemical approach has been traditionally studied to manipulate the valence state of TM, of which the versatility is accompanied by changes in the crystal structure or composition of TMOs. For example, in 2012, Ichikawa *et al*.[37] tried to reduce and oxidize the $SrCoO_{2.5}$ film into $SrCoO_2$ and $SrCoO_3$ by using strong reducing (CaH_2) and oxidizing (NaClO) agents, respectively. The $SrCoO_3$ epitaxial thin films were obtained topotactically at room temperature by the oxidation treatment. However, they could not observe any sign of $SrCoO_2$ crystal

formation. All X-ray diffraction peaks disappeared, and therefore, it was concluded that the $SrCoO_{2.5}$ crystal was destroyed by the reduction treatment. This indicates that CaH_2 is not appropriate as the reducing agent, which is probably due to difficulties in controlling the amount or speed of reduction. In addition, in 2017, Khare *et al*.[38] realized the topotactic phase transformation of $SrFeO_x$ thin films from $SrFeO_{2.5}$ to $SrFeO_3$ by post-annealing in the O_2 atmosphere. Unfortunately, all these methods are not suitable for practical memory applications since the chemical reaction is irreversible and requires a relatively high reaction temperature as well as a long reaction time.

Therefore, to overcome these problems, several researchers reported electrochemical methods to control the protonation/oxidation in TMOs (**Figure 1-3**). In 2019, by using the ionic liquid electrolyte, Saleem *et al*.[39] succeeded in the electrochemical topotactic phase transition of $SrFeO_x$ epitaxial films. Also in 2017, via the electrochemical protonation of $SrCoO_x$ utilizing the residual water in the ionic liquid, the $H_xSrCoO_{2.5}$ phase accompanied with the changes in optical, electrical, and magnetic properties was firstly demonstrated.[40] When a voltage over 1.23 V was applied, water electrolysis theoretically occurs, which provides proton and oxide ions for the modulation of TMOs structure. Very recently, it was reported that the electrochemical control of oxygen and proton concentration in $SrCoO_x$ induced a thermal conductivity difference among tristate phases: $H_xSrCoO_{2.5}$, $SrCoO_{2.5}$, and $SrCoO_3$.[41] This offers another possible application like a thermal transistor. However, these examples involve the usage of liquid electrolyte with

the risk of liquid leakage, which limits the practical applications.

1.3 Solid-state electrochemistry in TMOs

For overcoming the leakage issue, the use of the all-solid-state structure is believed to be the most ideal way. There are many solid electrolyte candidates. One example is amorphous $NaTaO_3$ [42,43]. The nanopillar structure amorphous $NaTaO_3$ film can be fabricated by pulsed laser deposition (PLD) method, and the film density can be modulated by the growth condition, which is beneficial for lowering film density for water vapor absorption. In 2016, Katase *et al.*[42] used amorphous $NaTaO_3$ film with nanopillar structure as the solid electrolyte to successfully convert $SrCoO_{2.5}$ film to $SrCoO_3$ film at room temperature. However, due to the strong alkalinity of NaOH resulting from the reaction between $NaTaO_3$ and water, they could not protonate $SrCoO_{2.5}$ into $H_xSrCoO_{2.5}$. In this regard, the solid electrolyte containing neutral water in a similar porous structure can be of use. A mesoporous amorphous $12CaO{\cdot}7Al_2O_3$ (CAN) film, filled with ultrapure water in its meso-pores (~40 vol.%), shows an electrical conductivity value of 2×10^{-9} S cm^{-1} at room temperature.[44] The advantage of CAN film as the solid electrolyte is that the water concentration could be modulated easily through controlling the oxygen pressure during fabrication processes as shown in **Figure 1-4(a)**. Katase *et al*. demonstrated that VO_2[33] and WO_3[27] can be protonated at room temperature through an electrochemical method with CAN as the solid electrolyte (**Figure 1-4(b)**). From these considerations, it can be expected that both protonation and oxidation of $SrCoO_{2.5}$ are

possible by using CAN as the solid electrolyte.

In addition to the insertion and removal of H^+ ions, another method for controlling the functional properties of TMOs involves the oxygen vacancy control (electrochemical redox control of oxygen migration). As mentioned earlier, Ichikawa *et al*.[37] tried to reduce the $SrCoO_{2.5}$ film by using CaH_2 but failed. Hence, an alternate method is necessary to realize tristate devices using phase transition between $SrCoO_{2.5-x}$, $SrCoO_{2.5}$, and $SrCoO_3$. In order to continually modulate the oxygen concentration, the solid-state electrochemical redox using an oxide ion-conductive electrolyte is needed. Yttria-stabilized zirconia (YSZ) has a great potential in this regard because YSZ is known as an excellent oxide ion (O^{2-}) conductor[45-47] exhibiting dc electrical conductivity of 10^{-6} S cm^{-1} at 300 °C as shown in **Figure 1-5**[48]. It can be expected that O^{2-} ions in a TMO crystal would be extracted/inserted by applying a voltage through YSZ at 300 °C in air. Moreover, YSZ is also an excellent substrate for TMO film growth. Lu *et al*.[49] reported that $SrCoO_{2.5}$ was heteroepitaxially grown on Gd-doped CeO_2 (GDC)-buffered YSZ substrate and successfully controlled the crystalline phase between $SrCoO_{2.5}$ and $SrCoO_3$. Therefore, TMO films on YSZ substrates provide a great platform for studying solid-state electrochemistry of TMOs.

1.4 Objective of this research

The main target of this research is the development of all-solid-state memory devices by

cross-coupling the physical properties in TMO systems. $SrCoO_x$ and $SrFeO_x$ were selected as the candidates since their physical properties can be clearly modulated by the structural phase transition. $SrCoO_{2.5}$ is known as an oxygen sponge[50], where the ordering of one-dimensional oxygen vacancy channels in the structure can work as the path to accommodate additional oxygen, making it easy to modulate the oxygen stoichiometry through the topotactic redox reaction of $SrCoO_x$. Moreover, $SrCoO_x$ exhibits tristate phases transition. These phases depend on the valence state of Co ions: brownmillerite (BM) $SrCoO_{2.5}$ (Co^{3+}) is orthorhombic structure with lattice parameters of a = 5.5739 Å, b = 5.4697 Å, and c = 15.7450 Å, which can be denoted as pseudo-tetragonal (a = 3.905 and $c/4$ = 3.936 Å)[51]; perovskite (PV) $SrCoO_3$ (Co^{4+}) is a cubic structure with a = 3.830 Å[52]; protonated BM $H_xSrCoO_{2.5}$ (Co^{2+})[40,53] and another reduced phase $SrCoO_2$ (Co^{2+})[54]. The crystal structures are summarized in **Figure 1-6**. BM $SrCoO_{2.5}$ is a brown antiferromagnetic insulator, and PV $SrCoO_3$ is a black ferromagnetic metal. In addition, protonated $H_xSrCoO_{2.5}$ is almost transparent in the visible spectrum, exerting electrically insulating and weak ferromagnetic behaviors. Furthermore, the thermal conductivity of $SrCoO_x$ can also be tuned by the electrochemical protonation and oxidation.[41] From these considerations, $SrCoO_x$ is promising as the active material in the electrochemical memory device as the optical, electrical, magnetic, and thermal properties of $SrCoO_x$ are modulated electrochemically.

Similarly, strontium ferrite ($SrFeO_x$) also exhibits an obvious phase transition from

orthorhombic BM antiferromagnetic insulator ($SrFeO_{2.5}$, Fe^{3+}) to cubic PV helimagnetic metal ($SrFeO_3$, Fe^{4+}) by changing the oxide ion (O^{2-}) concentration. The lattice parameters of $SrFeO_{2.5}$ are $a/\sqrt{2}$ = 4.01 Å, $b/4$ = 3.90 Å, and $c/\sqrt{2}$ = 3.91 Å, whereas the a of $SrFeO_3$ (Cubic) is 3.850 Å.[55] Due to the multiple valence states of Fe, the valence state dependent physical properties can be studied in $SrFeO_x$. In addition, since $SrFeO_x$ has a similar crystal structure with $SrCoO_x$, it also can be used to examine the feasibility of the electrochemical redox treatment of TMO using YSZ as the solid electrolyte.

The given dissertation is organized as the following. The background and motivation are discussed in Chapter 1. The experimental procedures including the film device fabrication, crystal structural characterizations, and functional property measurements are presented in Chapter 2. Chapter 3 focused on the analysis of the electronic structure of $SrCoO_{2.5}$ films by using the thermopower as the metric. An extremely small difference in the electronic structure and the oxidation states among the films are discussed using thermopower values exhibiting positive/negative sign reversal. In Chapters 4−6, proton/oxide ion insertion and removal in $SrCoO_x$ and $SrFeO_x$ systems by the solid-state electrochemical method as well as the resulting phase transition induced change on physical properties are investigated. Chapter 4 explored the solid-state electrochemical protonation of $SrCoO_{2.5}$ into $H_xSrCoO_{2.5}$ using CAN electrolyte instead of ionic liquid. The crystalline phase was controlled from $SrCoO_{2.5}$ to $HSrCoO_{2.5}$, $H_{1.5}SrCoO_{2.5}$, and $H_2SrCoO_{2.5}$, which were accompanied with clear optical, electrical, and magnetic

property transitions. Chapters 5 and 6 concentrated on the electrochemical redox reaction using YSZ substrate as the solid-electrolyte. The crystalline phases were reversibly converted from an as-grown state to oxidized state. Simultaneously, the thermopower and optoelectronic properties of these thin films were clarified. Finally, all results and the contributions of the given doctoral research are summarized in Chapter 7.

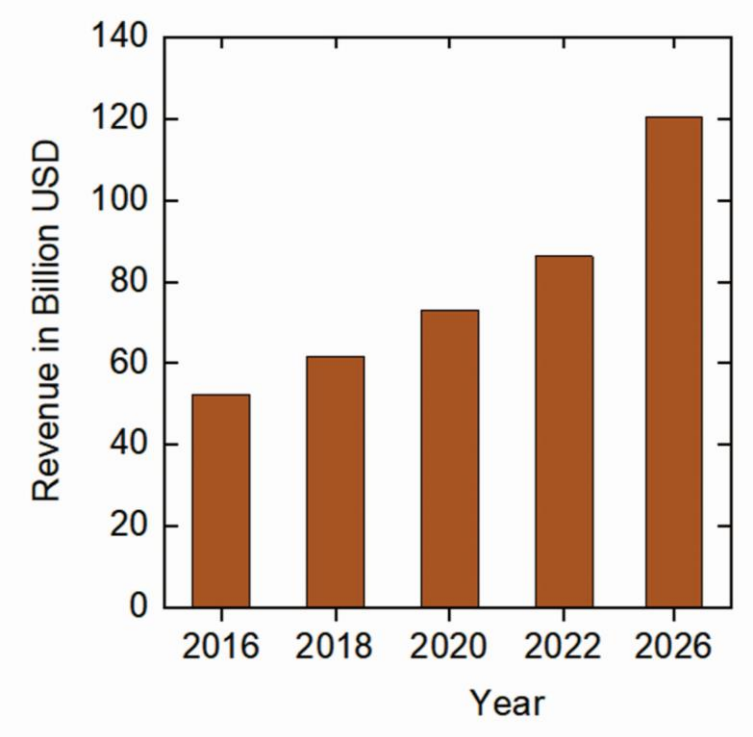

Figure 1-1. Growth of the market size of non-volatile memory devices.[8]

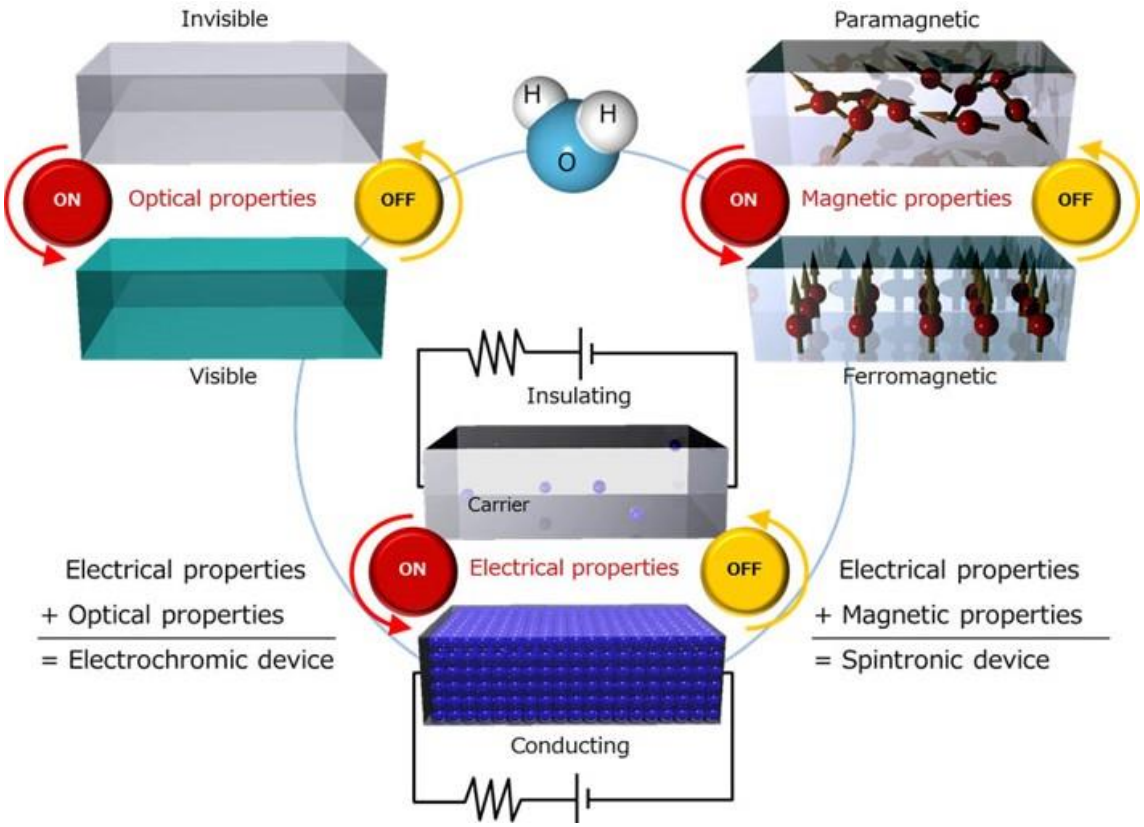

Figure 1-2. Concept of transition metal oxides-based memory devices.

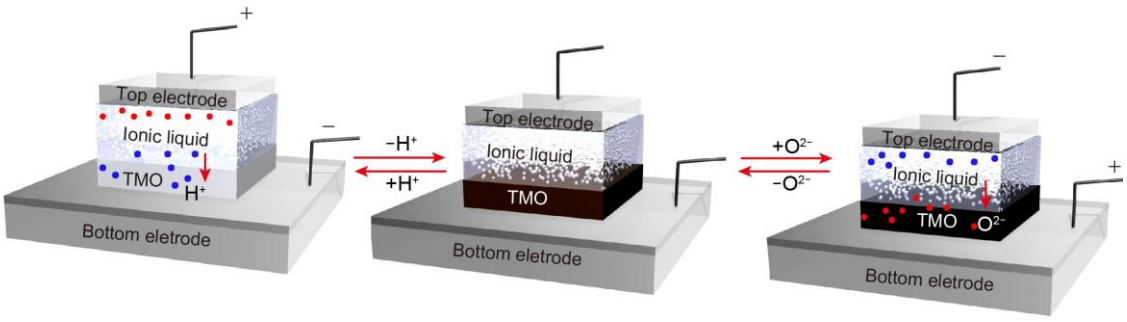

Figure 1-3. Schematic protonation/oxidation diagram of TMO electrochemical cell.

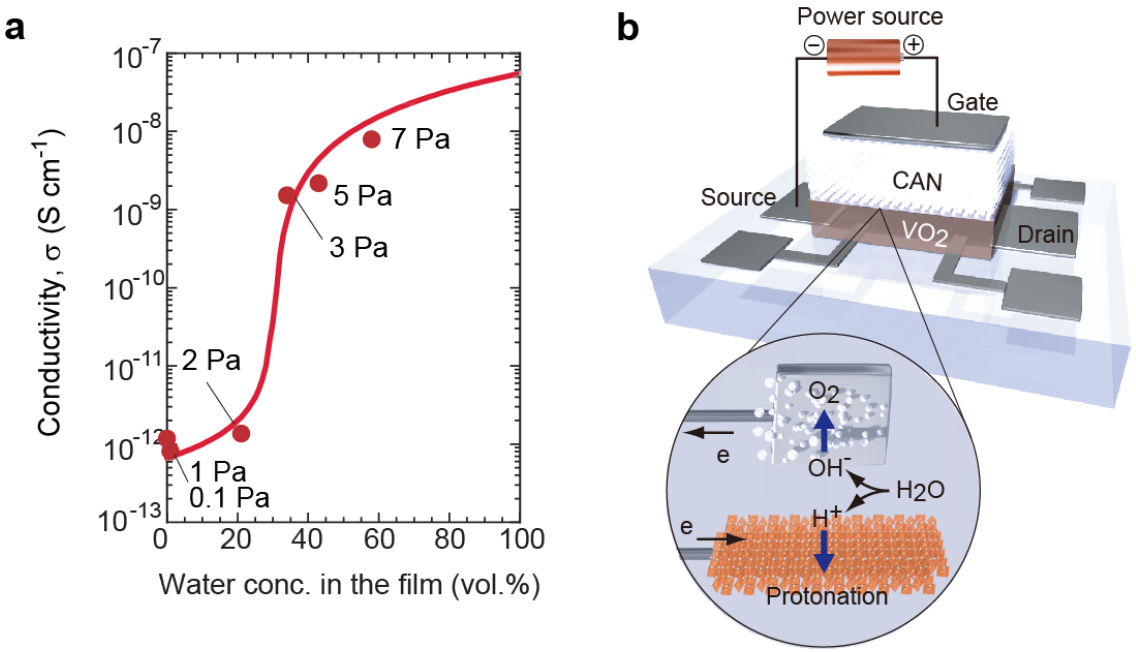

Figure 1-4. (a), Electrical conductivity of the CAN films as a function of water concentration. The CAN films were deposited at different oxygen pressure.[44] (b), Schematic illustration of the solid-state VO_2-based electrochemical device with CAN film as the solid electrolyte.[33]

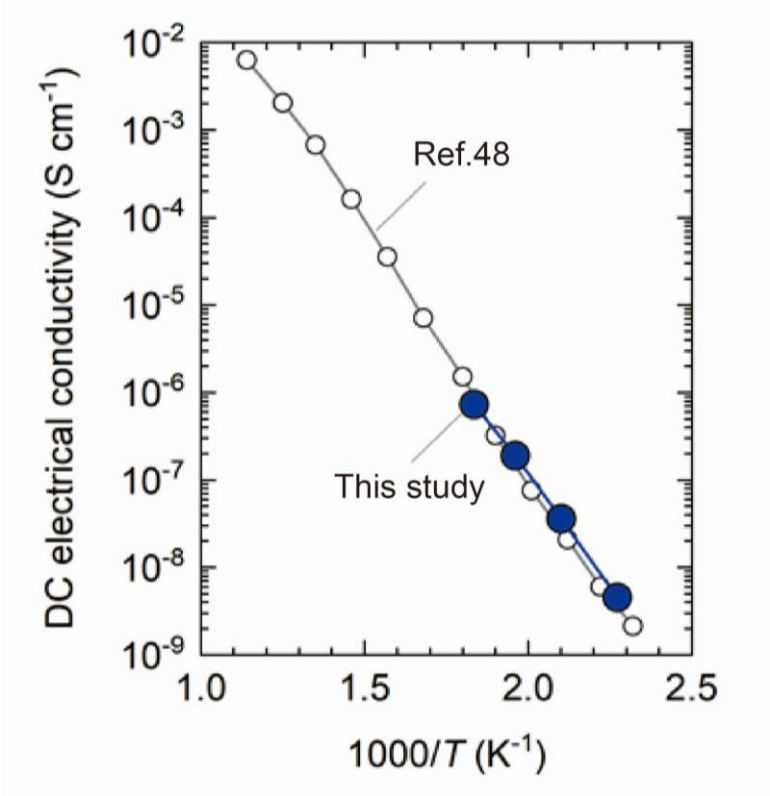

Figure 1-5. Temperature dependence of the oxide ion conductivity of YSZ.[48]

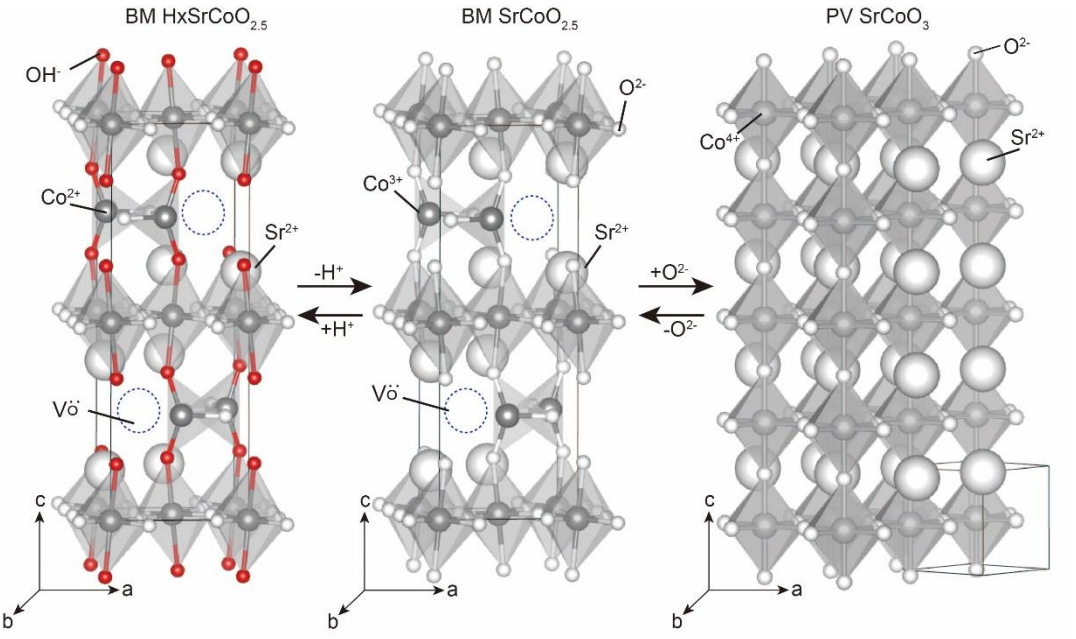

Figure 1-6. Schematic crystal structure of (left) protonated $H_xSrCoO_{2.5}$, (center) $SrCoO_{2.5}$, and (right) oxidized $SrCoO_3$.

References

1 Tiwari, S. *et al.* in *Proceedings of International Electron Devices Meeting.* 521-524 (IEEE).

2 Reed, M. A. *et al*. Molecular random access memory cell. *Appl. Phys. Lett.* **78**, 3735-3737 (2001).

3 Meena, J. S. *et al*. Overview of emerging nonvolatile memory technologies. *Nanoscale Res. Lett.* **9**, 1-33 (2014).

4 Chen, A. A review of emerging non-volatile memory (NVM) technologies and applications. *Solid-State Electron.* **125**, 25-38 (2016).

5 Lacaze, P.-C. *et al*. *Non-volatile memories*. (John Wiley & Sons, 2014).

6 Pavan, P. *et al*. Flash memory cells-an overview. *Proceedings of the IEEE* **85**, 1248-1271 (1997).

7 Zahoor, F. *et al*. Resistive random access memory (RRAM): an overview of materials, switching mechanism, performance, multilevel cell (MLC) storage, modeling, and applications. *Nanoscale Res. Lett.* **15**, 1-26 (2020).

8 Profshare n.d. Non-Volatile Memory Market, accessed 18 January 2022, https://www.profsharemarketresearch.com/non-volatile-memory-market-report/.

9 Masuoka, F. & Iizuka, H. Semiconductor memory device and method for manufacturing the same. US4531203A, Japan (1985).

10 Kumar, M. P. *et al*. in *2019 IEEE International Conference on Intelligent Systems and Green Technology (ICISGT).* 49-493 (IEEE).

11 Chen, F. *et al.* Temperature Impacts on Endurance and Read Disturbs in Charge-Trap 3D NAND Flash Memories. *Micromachines* **12**, 1152 (2021).

12 White, M. H. Charge retention of scaled SONOS nonvolatile memory devices at elevated temperatures. *Solid-State Electron.* **44**, 949-958 (2000).

13 Chang, M. *et al*. Band bending effect induced by gate voltage on the charge loss behavior of charge trap flash memory devices. *Appl. Phys. Lett.* **96**, 052106 (2010).

14 Aritome, S. *et al*. Reliability issues of flash memory cells. *Proceedings of the IEEE* **81**, 776-788 (1993).

15 Li, Y. *et al.* An overview of resistive random access memory devices. *Chinese Sci. Bull.* **56**, 3072-3078 (2011).

16 Akinaga, H. *et al*. Resistive random access memory (ReRAM) based on metal oxides. *Proceedings of the IEEE* **98**, 2237-2251 (2010).

17 Sawa, A. Resistive switching in transition metal oxides. *Mater. today* **11**, 28-36 (2008).

18 Bersuker, G. *et al.* Metal oxide resistive memory switching mechanism based on conductive filament properties. *J. Appl. Phys.* **110**, 124518 (2011).

19 Gupta, V. *et al*. Resistive random access memory: A review of device challenges. *IETE Tech. Rev.* **37**, 377-390 (2020).

20 Ntinas, V. *et al.* Power-Efficient Noise-Induced Reduction of ReRAM Cell's Temporal Variability Effects. *IEEE Trans. Circuits Syst. II Express Briefs* **68**, 1378-1382 (2020).

21 Chen, P.-W. *et al.* Fast response of complementary electrochromic device based on WO_3/NiO electrodes. *Sci. Rep.* **10**, 1-12 (2020).

22 Barawi, M. *et al.* A dual band electrochromic device switchable across four distinct optical modes. *J. Mater. Chem. A* **6**, 10201-10205 (2018).

23 Onozato, T. *et al*. Fast operation of a WO_3-based solid-state electrochromic transistor. *AIP Adv.* **9**, 025122 (2019).

24 Puebla, J. *et al*. Spintronic devices for energy-efficient data storage and energy harvesting. *Commun. Mater.* **1**, 1-9 (2020).

25 Barla, P. *et al*. Spintronic devices: a promising alternative to CMOS devices. *J. Comput. Electron.* **20**, 805-837 (2021).

26 Singh, R. *et al*. in *Multifunctional Nanostructured Metal Oxides for Energy*

Harvesting and Storage Devices 113-128 (CRC Press, 2020).

27 Katase, T. *et al*. A transparent electrochromic metal-insulator switching device with three-terminal transistor geometry. *Sci. Rep.* **6**, 1-9 (2016).

28 Mannhart, J. *et al*. The value of seeing nothing. *Nature* **430**, 620-621 (2004).

29 Takagi, H. *et al*. An emergent change of phase for electronics. *Science* **327**, 1601-1602 (2010).

30 Dagotto, E. Complexity in strongly correlated electronic systems. *Science* **309**, 257-262 (2005).

31 Rao, C. N. R. Transition metal oxides. *Annu. Rev. Phys. Chem.* **40**, 291-326 (1989).

32 Kim, G. *et al.* Coexistence of High Electron Conduction and Low Heat Conduction in Tungsten Oxide Epitaxial Films with 1D Atomic Defect Tunnels. *ACS Appl. Electron. Mater.* **2**, 2507-2513 (2020).

33 Katase, T. *et al*. Room-Temperature-Protonation-Driven On-Demand Metal–Insulator Conversion of a Transition Metal Oxide. *Adv. Electron. Mater.* **1**, 1500063 (2015).

34 Wang, H. *et al.* Oxygen vacancies on the surface of H_xWO_{3-y} for enhanced charge storage. *J. Mater. Chem. A* **6**, 6780-6784 (2018).

35 Yao, L. *et al*. Direct observation of oxygen vacancy-driven structural and resistive phase transitions in $La_{2/3}Sr_{1/3}MnO_3$. *Nature commun.* **8**, 1-9 (2017).

36 Li, D. *et al.* Superconductivity in an infinite-layer nickelate. *Nature* **572**, 624-627 (2019).

37 Ichikawa, N. *et al.* Reduction and oxidation of $SrCoO_{2.5}$ thin films at low temperatures. *Dalton Trans.* **41**, 10507-10510 (2012).

38 Khare, A. *et al.* Topotactic metal–insulator transition in epitaxial $SrFeO_x$ thin films. *Adv. Mater.* **29**, 1606566 (2017).

39 Saleem, M. S. *et al.* Electric field control of phase transition and tunable resistive switching in $SrFeO_{2.5}$. *ACS Applied Mater. Interfaces* **11**, 6581-6588 (2019).

40 Lu, N. *et al.* Electric-field control of tri-state phase transformation with a selective

dual-ion switch. *Nature* **546**, 124-128 (2017).

41 Lu, Q. *et al.* Bi-directional tuning of thermal transport in $SrCoO_x$ with electrochemically induced phase transitions. *Nature Mater.* **19**, 655-662 (2020).

42 Katase, T. *et al*. Reversibly Switchable Electromagnetic Device with Leakage-Free Electrolyte. *Adv. Electron. Mater.* **2**, 1600044 (2016).

43 Katase, T. *et al*. Highly conducting leakage-free electrolyte for $SrCoO_x$-based non-volatile memory device. *J. Appl. Phys.* **122**, 135303 (2017).

44 Ohta, H. *et al.* Field-induced water electrolysis switches an oxide semiconductor from an insulator to a metal. *Nature commun.* **1**, 1-6 (2010).

45 Ahamer, C. *et al*. Revisiting the temperature dependent ionic conductivity of yttria stabilized zirconia (YSZ). *J. Electrochem. Soc.* **164**, F790 (2017).

46 Zhao, W. *et al*. Influence of thickness on the electrical conductivity of YSZ electrolytes. *J. Ceram. Soc. Japan* **118**, 550-554 (2010).

47 Shim, J. H. *et al*. Atomic layer deposition of yttria-stabilized zirconia for solid oxide fuel cells. *Chem. Mater.* **19**, 3850-3854 (2007).

48 Garcia-Barriocanal, J. *et al.* Colossal ionic conductivity at interfaces of epitaxial ZrO2: Y_2O_3/$SrTiO_3$ heterostructures. *Science* **321**, 676-680 (2008).

49 Lu, Q. *et al*. Voltage-controlled topotactic phase transition in thin-film $SrCoO_x$ monitored by in situ x-ray diffraction. *Nano Lett.* **16**, 1186-1193 (2016).

50 Jeen, H. *et al.* Reversible redox reactions in an epitaxially stabilized $SrCoO_x$ oxygen sponge. *Nature Mater.* **12**, 1057-1063 (2013).

51 Jeen, H. *et al.* Topotactic phase transformation of the brownmillerite $SrCoO_{2.5}$ to the perovskite $SrCoO_{3-\delta}$. *Adv. Mater.* **25**, 3651-3656 (2013).

52 Le Toquin, R. *et al*. Time-resolved in situ studies of oxygen intercalation into $SrCoO_{2.5}$, performed by neutron diffraction and X-ray absorption spectroscopy. *J. Am. Chem. Soc.* **128**, 13161-13174 (2006).

53 Li, H. B. *et al.* Electric Field–Controlled Multistep Proton Evolution in $H_xSrCoO_{2.5}$ with Formation of H–H Dimer. *Advanced Science* **6**, 1901432 (2019).

54 Li, H.-B. *et al.* Dehydration of Electrochemically Protonated Oxide: $SrCoO_2$ with Square Spin Tubes. *J. Am. Chem. Soc.* **143**, 17517-17525 (2021).

55 Yamada, H. *et al*. Epitaxial growth and valence control of strained perovskite $SrFeO_3$ films. *Appl. Phys. Lett.* **80**, 622-624 (2002).

Chapter 2. Experimental Methods

2.1 Pulsed Laser Deposition (PLD)

Pulsed laser deposition (PLD) was used to fabricate TMO thin films. PLD is a type of physical vapor deposition (PVD) technology. It exhibits great controllability with high deposition rate and became a key technique for fabricating high-quality epitaxial thin films.[1,2] Its schematic illustration is shown in **Figure 2-1** (KrF excimer laser, $\lambda = 248$ nm). There are many complex phenomena involved in the film growth processes, but the growth mechanism can be briefly described as follows: (1) high-power laser pulse ablates the target surface to create a plasma plume in a vacuum chamber; (2) the particles in the plasmas are condensed onto a heated substrate and produce the film. The film deposition process is strongly related to the interaction between the plasma and the surface morphology of the substrate. If vaporized ions with high kinetic energy reach the substrate, they may bombard out a portion of the surface atoms and damage the substrate. In this case, a region of high collision rate forms in the vicinity of substrate due to the interaction between the initial flux of plasma particles and the sputtered atoms from the substrate surface, which causes particle condensation. The film grows immediately upon the formation of this collision region. In contrast, if the rate of plasma flow is low, the collision region cannot be formed, and the film growth directly relies on the flow of the ablated particles. For these reasons, the film quality and surface morphology are affected by substrate temperature, laser energy, deposition rate, and vacuum level during

deposition, which makes PLD suitable for preparing various forms of high-quality multifunctional films, such as optoelectronics, ferroelectrics, piezoelectrics, and high-temperature superconductors.

2.2 Reflection high-energy electron diffraction

In this study, reflection high-energy electron diffraction (RHEED)[3,4] in the PLD system was adopted to monitor the *in-situ* film growth process as shown in **Figure 2-2**. Generally, RHEED is installed in a high-vacuum chamber, where high-energy electrons (10−50 keV) are irradiated onto the film surface with an incidence angle of 3−5 °. These electron beams penetrate the atomic planes near the film surface, resulting in the RHEED pattern, which is the cross-sectional projection of the reciprocal lattice. To comprehend the RHEED pattern, it is essential to understand the Ewald construction (**Figure 2-2(a)**). When electron beam is incident on the crystal, it will be scattered by the lattice atoms. The diffraction spots appear only when the reciprocal lattice points fall on the Ewald sphere. One example from this research is shown in **Figure 2-2(b)**. According to RHEED patterns associated with different surface morphology (**Figure 2-2(c)**), the film surfaces in this study were flat.

2.3 Structure characterizations

X-ray diffraction (XRD) was used for crystallographic analyses, including the crystalline phase, orientation, and lattice parameters as well as strain. X-ray diffraction condition

follows the Bragg's law, which can be expressed as:

$$n \cdot \lambda = 2 \cdot d_{hkl} \cdot \sin \theta$$

Here, λ is the wavelength of the X-ray radiation; n is the diffraction order; d_{hkl} is the distance between the respective crystal planes; θ is the diffraction angle.

In this study, high-resolution X-ray diffraction (HRXRD, ATX-G, Rigaku Co.)[5] was used as shown in **Figure 2-3(a-b)**. Monochromatic X-ray beam with a wavelength of 1.54059 Å (Cu $K\alpha_1$) was used. ω is the angle between the incident X-ray beam and the sample surface while 2θ is the angle between the incident beam and the diffracted beam. In addition, the other two Euler angles φ and χ can be adjusted for controlling the beam direction with respect to the in-plane axes. The orientations of the film and substrate can be clarified by the out-of-plane and in-plane XRD (**Figure 2-3(c)**). For the out-plane XRD, $2\theta/\omega$ scan was performed. In the ω scan, the rocking curve can be obtained, where the crystal tilting can be estimated from the full width half maximum (FWHM, **Figure 2-3(d)**). In contrast, by performing the $2\theta\chi/\varphi$ scan with fixed $2\theta/\omega$, one can get the in-plane diffraction information of the lattice. During the X-ray reflectivity (XRR) measurement, due to the reflectivity difference in the film and substrate, the incident X-ray reflected at the film/substrate interface and film surface interfere with each other, resulting in an oscillation (**Figure 2-3(e)**). By fitting the fringes, the thickness, density, and roughness can be estimated.

To investigate the film structure in detail, high-angle annular dark field scanning transmission electron microscopy (HAADF-STEM) was performed at the University of Tokyo (**Figure 2-4**). When the incident electron beam intervenes with the sample, it gets elastically and inelastically scattered, which changes the direction and energy of the electrons. The HAADF-STEM image is obtained by detecting the inelastically scattered electrons or thermal scattered electrons at high angles with an annular dark-field (ADF) detector. For ADF mode (range of θ_2), the elements with larger *Z*-value are observed in brighter contrast, but elements with smaller *Z*-value are difficult to be observed.[6,7] In order to visualize light atoms, annular bright-field (ABF, range of θ_3) STEM[8] and low-angle annular dark-field (LAADF) STEM[9] are utilized. In the range of θ_1, signal comes from incoherently scattered electrons at very high incident angles. This micrograph is known as HAADF *Z*-contrast micrograph, which is highly dependent on the atomic number (*Z*-value).[10] In addition, STEM can also analyze the electronic structure of the film with electron energy loss spectrum (EELS). It is also possible to perform micro-area energy dispersive spectroscopy (EDS) to analyze the chemical composition.

Atomic force microscopy (AFM, Nanocute, Hitachi High-Tech Sci. Co.)[11,12] was used to check the surface morphology of the films (**Figure 2-5**). The AFM is mainly composed of cantilever tip, scanning tube, laser, photoelectric detector, feedback system, and image system. If the tip is close to the sample, a reference value (setpoint) is set. The signal from the interaction between tip and film surface is detected as the tip moves along the surface.

Comparing this signal and the setpoint through the feedback system, the error signal can be obtained, which is directly fed through the feedback system that controls the scanning tube to change the voltage, keeping the measured value consistent with the setpoint. This process is recorded by the imaging system to reflect the surface morphology. In order to observe insulator to metal transition through electrochemical oxidation, conductive area of the film surface in a dimension of 5 μm × 5 μm (512 lines, 1 Hz) was visualized using conducting AFM (MFP-3D Origin^{TM}, Oxford Instruments) by applying −2 V against the sample surface using Pt coated cantilever in the air at room temperature.[13]

2.4 Optical property measurements

The optical transmission and reflection spectra of the films were measured by using the ultraviolet-visible-near infrared (UV-VIS-NIR) spectrometer (SolidSpec-3700, Shimadzu, **Figure 2-6**). Generally, the spectrophotometer is mainly composed of a light source system, monochromator system, sample station, and detector. The light source is separated into a monochromatic light by the monochromator. Then, the monochromatic light illuminates the sample, causing a part of the light to be absorbed by the sample. Simultaneously, reflected and transmitted light can be gathered, which can be analyzed by the detecting and processing systems to extract the optical properties of samples. In addition, FT-IR (model IRPrestige-21, Shimadzu) was performed from 1300 nm to 5000 nm to further analyze the optical transmission.

2.5 X-ray spectroscopy

X-ray spectroscopy can analyze the valence state of ions by exciting the core electrons, among which the X-ray photoelectron spectroscopy (XPS) and X-ray absorption spectroscopy (XAS) are widely used.[14,15] XPS is sensitive to the surface chemical state. When a specimen is irradiated by X-rays, photoelectrons are emitted. During this process, the kinetic energy (E_K) of the emitted photoelectrons is measured, and the binding energy (E_B) is obtained using the Einstein equation:

$$E_B = h\nu - (E_K + \varphi)$$

where E_B is the binding energy of the electron relative to the chemical potential, $h\nu$ is the energy of the X-ray, and φ is the instrument's work function. E_B is the characteristic of specific atomic configurations. The same atom in different chemical bonding environment results in different binding energy, which causes chemical shifts. Through the analysis of this chemical shift, the valence state of the same atoms in different states can be distinguished.

On the other hand, XAS is a unique tool for observing the local structure around a selected element at atomic scales. When the incident X-ray energy is equal to the ionization energy of the core electrons, they will be emitted as photoelectrons, resulting in a sudden change of X-ray absorption. This is called an absorption edge in the X-ray absorption spectrum. The absorption edges K-edges, L-edges, and M-edges are corresponded to the principal quantum number n = 1, 2, and 3, respectively. Since the absorption edge is determined by

the quantum number and the electron configuration of the valence band, XAS can be used for qualitative analysis of elements and their chemical states.

In this study, XPS was used to confirm the valence state of Co in as-prepared $SrCoO_{2.5}$ films. Al Kα flood gun was used to realize a charging-free measurement at room temperature. All spectra were calibrated with C 1s peak at 284.8 eV. XAS was also performed around the Co $L_{2,3}$ edges in Pohang accelerator laboratory (2A). Surface-sensitive electron yield mode was used (the penetration depth of X-ray ~10 nm).

2.6 Thermopower

Thermopower (S) is known as one of the methods to address the electronic density of states (DOS) around the E_F (**Figure 2-7**). In the case of single-band semiconductors, the S value can be expressed by the Mott equation,[16]

$$S = \frac{\pi^2}{3}\frac{{k_B}^2 T}{e}\left\{\frac{d[\ln(\sigma(E))]}{dE}\right\}_{E=E_F} = \frac{\pi^2}{3}\frac{{k_B}^2 T}{e}\left\{\frac{1}{n}\cdot\frac{dn(E)}{dE}+\frac{1}{\mu}\cdot\frac{d\mu(E)}{dE}\right\}_{E=E_F}$$

where k_B, e, n, and μ are the Boltzmann constant, electron charge, carrier concentration, and carrier mobility, respectively. The right side is usually simplified as the slope of the DOS around the E_F, $\left[\frac{\partial DOS(E)}{\partial E}\right]_{E=E_F}$. In this research, S was used to detect the change of the electronic structure of TMOs. S of the films was characterized through a standard steady-state method at room temperature. The specimen was supported between two Peltier devices with a gap of ~5 mm, which can generate temperature difference through

applying the forward/reverse current to each side. The temperature difference (ΔT) was recorded along with the thermos-electromotive force (ΔV) simultaneously. The thermopower was deduced from the slope of ΔT – ΔV linear fitting.

2.7 Electrical resistivity

The electrical resistivity of the films was measured by dc four-probe method in the van der Pauw electrode configuration.[17] This method requires the specimen to be uniform and flat. Current is applied on two terminals, and the voltage drop is simultaneously measured through the other two terminals. Conventionally, it is necessary to repeatedly interchange current and voltage eight times as shown in **Figure 2-8(a-b)**. The sheet resistance (R) can be calculated by the following equations:

$$R_1: \quad R_{12,43}=\frac{V_{2(43)}-V_{1(43)}}{I_{12}-I_{21}}, \qquad R_2: \quad R_{23,14}=\frac{V_{2(14)}-V_{1(14)}}{I_{23}-I_{32}}$$

$$R_3: \quad R_{34,21}=\frac{V_{2(21)}-V_{1(21)}}{I_{34}-I_{43}}, \qquad R_4: \quad R_{41,32}=\frac{V_{2(32)}-V_{1(32)}}{I_{41}-I_{14}}$$

The series measurements are used to calculate the resistivity (ρ) based on the following equation:

$$\rho_1 = \frac{\pi}{\ln 2}\frac{R_1+R_2}{2} f\left[\frac{R_1}{R_2}\right] t$$

Four possible configurations are: ρ_1-R_1, R_2; ρ_2-R_2, R_3; ρ_3-R_3, R_4; ρ_4-R_4, R_1. Here t is the thickness of film, and f is the geometrical factor, which is 1 for perfect in-plane symmetry.

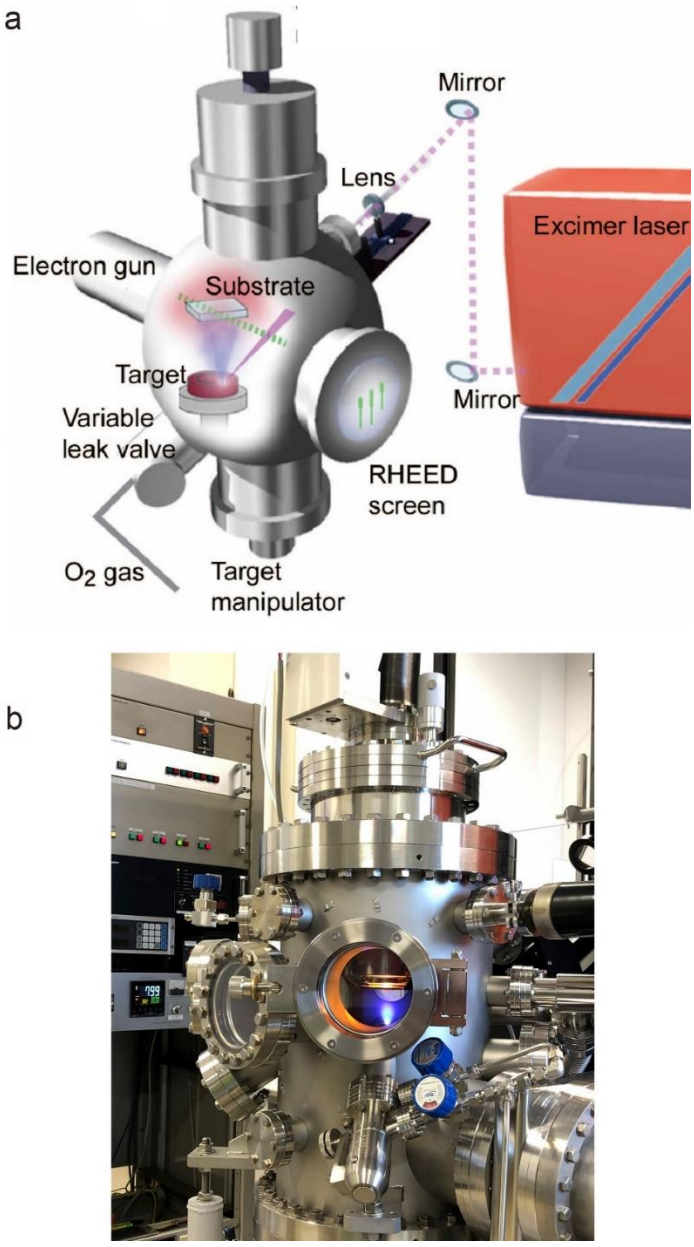

Figure 2-1. (a) Schematic illustration and (b) photograph of the PLD system.

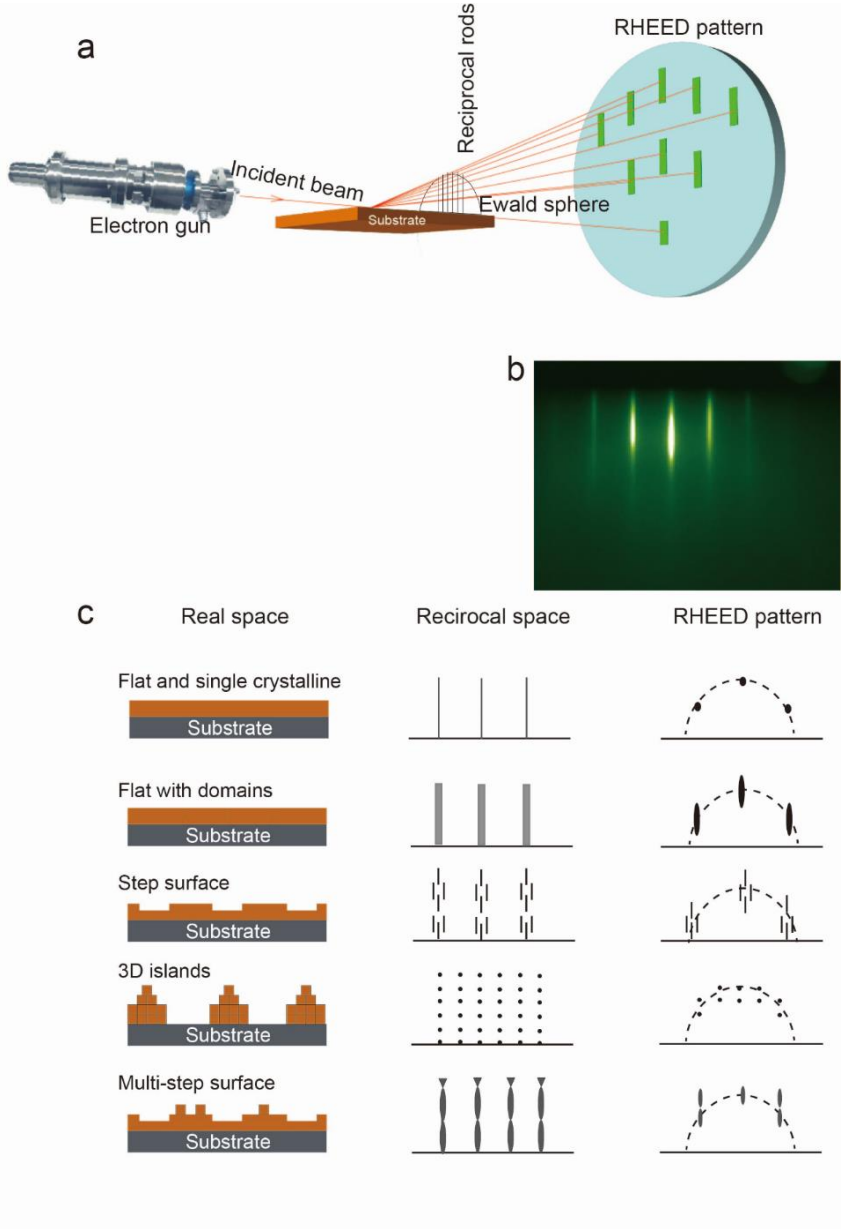

Figure 2-2. RHEED system. (a), The simplified diagram for the formation of RHEED pattern. (b), An example of RHEED picture from case of $SrCoO_{2.5}$. (c), The relationship between film surface, recirocal space, and related RHEED patterns.[4]

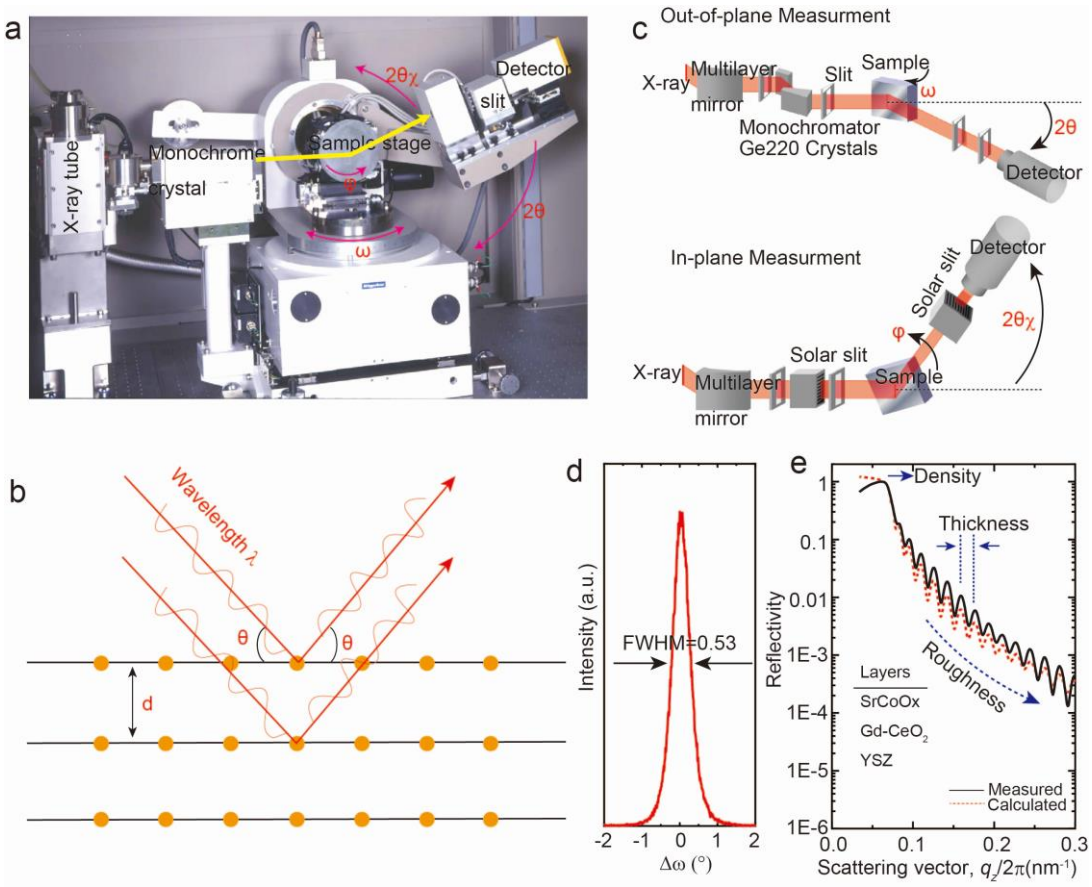

Figure 2-3. High-resolution XRD system. (a), Photograph of HRXRD setup. (b), Bragg' law. (c), Out-of-plane and in-plane measurment. (d), Rocking curve. (e), XRR curve of mulitlayers.

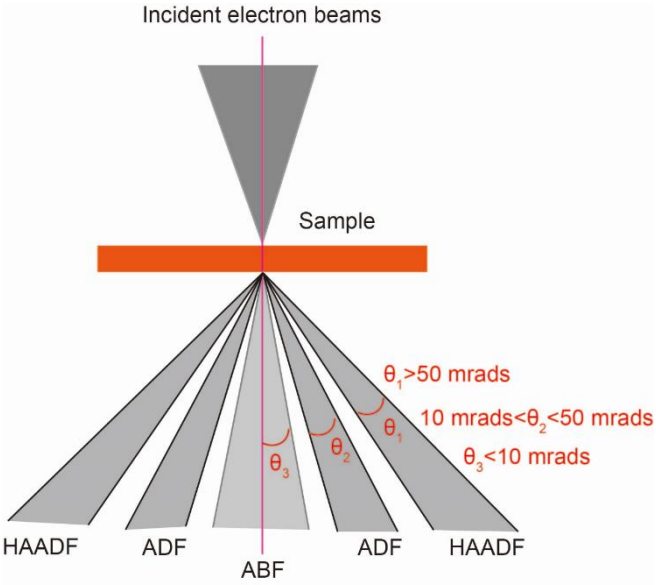

Figure 2-4. Schematic illustration of HAADF-STEM.

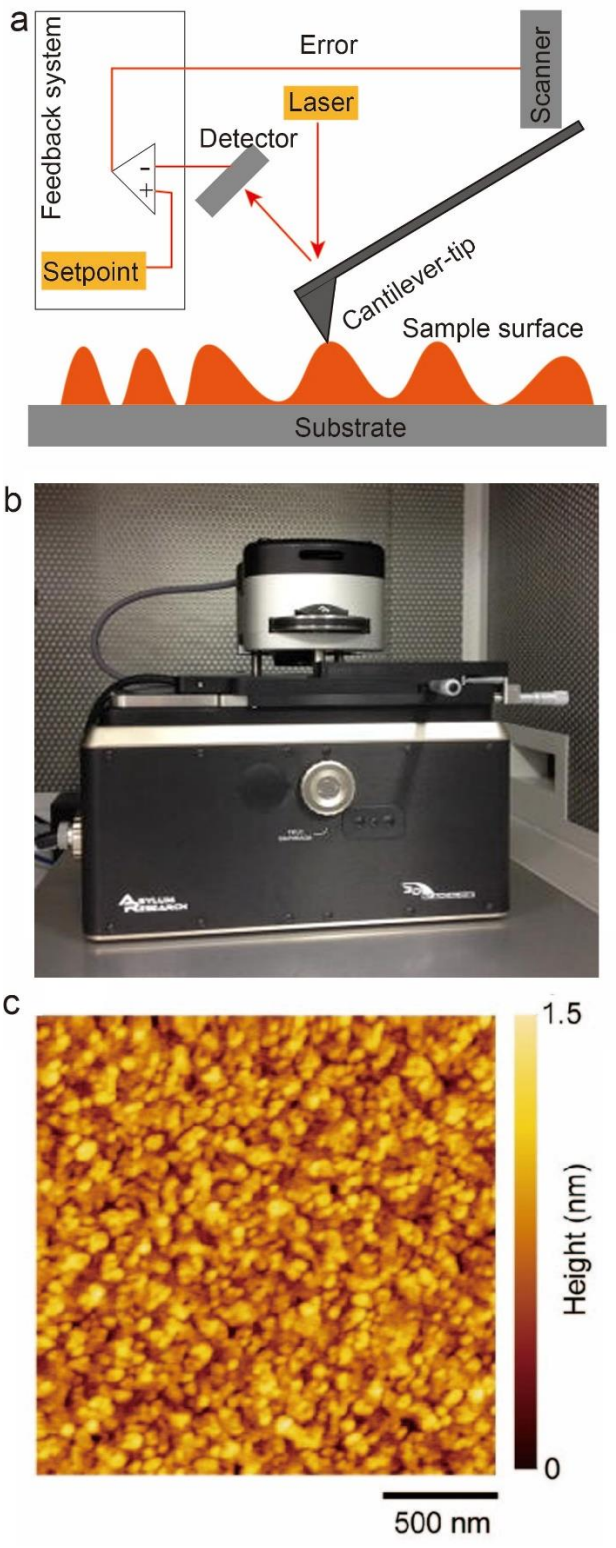

Figure 2-5. (a), Schematic diagram of AFM system. (b), photography of AFM instrument. (c), an example of AFM image.

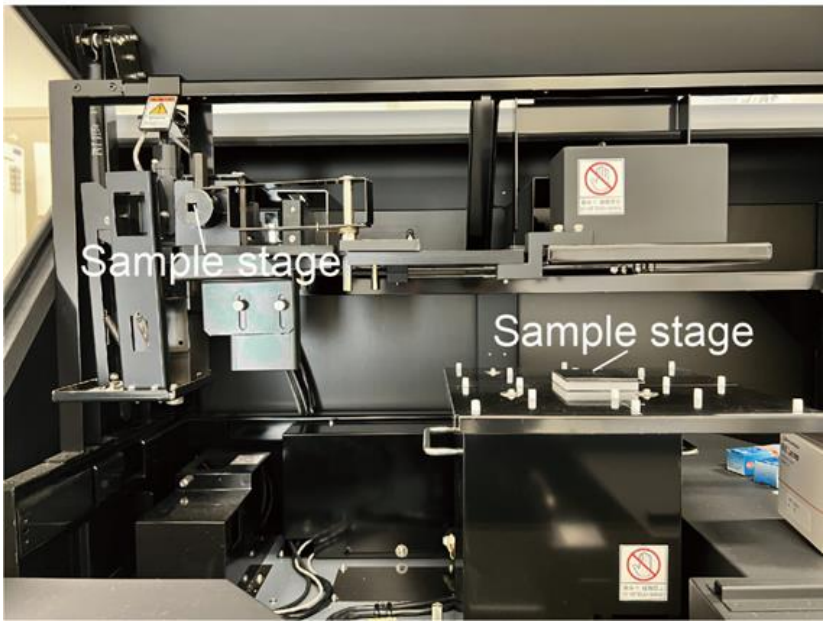

Figure 2-6. Photograph of the UV-Vis-NIR spectrometer.

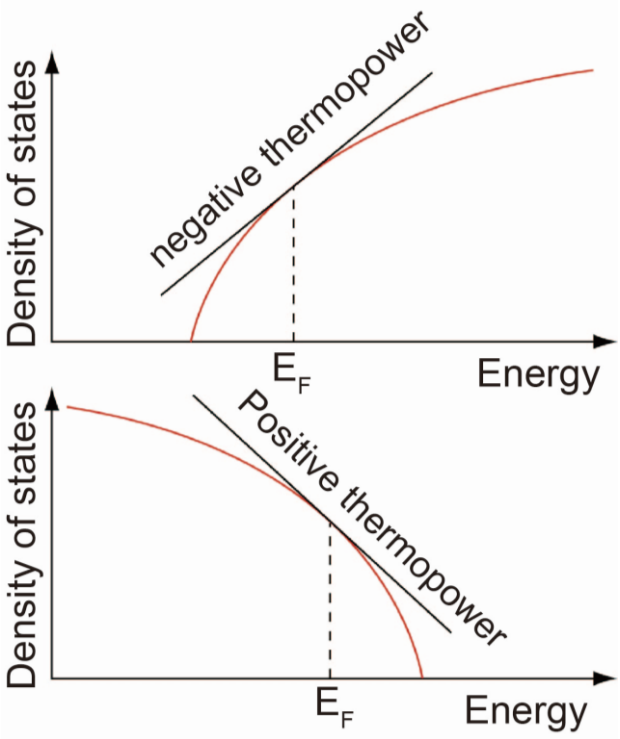

Figure 2-7. Schematic illustration of density of states explaining the relationship between thermopower and Fermi energy.

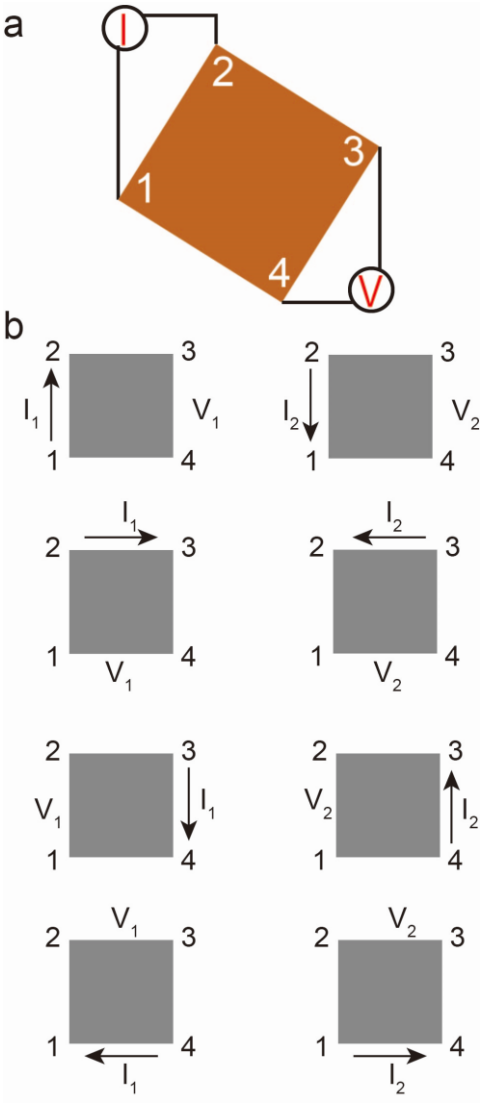

Figure 2-8. The resistivity measurement by van der Pauw electrode configuration. (a), Simple setup of van der Pauw method. (b), Repeated interchange of current and voltage probes.

References

1 Eason, R. *Pulsed laser deposition of thin films: applications-led growth of functional materials*. (John Wiley & Sons, 2007).

2 Krebs, H.-U. *et al.* in *Advances in Solid State Physics* 505-518 (Springer, 2003).

3 Ichimiya, A. *et al*. *Reflection high-energy electron diffraction*. (Cambridge University Press, 2004).

4 Hasegawa, S. Reflection high-energy electron diffraction. *Characterization of Materials* **97**, 1925-1938 (2012).

5 Krost, A. *et al*. in *Optical characterization of epitaxial semiconductor layers* 287-391 (Springer, 1996).

6 Nellist, P. *et al*. The principles and interpretation of annular dark-field Z-contrast imaging. *Adv. Imaging Electron Phys.* **113**, 147-203 (2000).

7 Hillyard, S. *et al*. Annular dark-field imaging: resolution and thickness effects. *Ultramicroscopy* **49**, 14-25 (1993).

8 Findlay, S. *et al.* Dynamics of annular bright field imaging in scanning transmission electron microscopy. *Ultramicroscopy* **110**, 903-923 (2010).

9 Phillips, P. J. *et al.* Atomic-resolution defect contrast in low angle annular dark-field STEM. *Ultramicroscopy* **116**, 47-55 (2012).

10 Rosenauer, A. *et al*. in *Microscopy of semiconducting materials 2007* 170-172 (Springer, 2008).

11 Rugar, D. *et al*. Atomic force microscopy. *Phys. Today* **43**, 23-30 (1990).

12 Eaton, P. *et al*. *Atomic force microscopy*. (Oxford university press, 2010).

13 Yang, Q. *et al*. Macroscopic visualization of fast electrochemical reaction of $SrCoO_x$ oxygen sponge. *Adv. Mater. Interfaces* **6**, 1901260 (2019).

14 Kawai, J. *et al*. Comparison between X-ray photoelectron and X-ray absorption spectra of an environmental aerosol sample measured by synchrotron radiation. *Spectrochim Acta Part B At Spectrosc* **54**, 241-245 (1999).

15 Mårtensson, N. *et al.* in 012131 (IOP Publishing).

16 Cutler, M. *et al*. Observation of Anderson localization in an electron gas. *Phys. Rev.* **181**, 1336 (1969).

17 David, T. *et al*. Novel analog switching circuit for van der Pauw measurements. *arXiv preprint cond-mat/0502182* (2005).

Chapter 3. Unusually Large Thermopower Change from +330 μV K^{-1} to −185 μV K^{-1} of Brownmillerite $SrCoO_{2.5}$

3.1 Objective of this Chapter

An ideal active material for memory application exhibits a drastic difference in observable properties such as electrical conductivity, magnetic response, and optical absorption, upon a small external influence. One interesting factor that affects the electrical properties of $SrCoO_{2.5}$ films is the lattice strain, where the Fermi energy (E_F) in $SrCoO_{2.5}$ films can be controlled through the lattice distortion. Therefore, it provides an opportunity to associate electrical properties with mechanical deformations, which can be utilized in developing $SrCoO_{2.5}$ based memory devices.

Till now, several studies have been done on the lattice strain-induced property variations in $SrCoO_{2.5}$. In 2018, Zhao *et al.*[1] reported that the electrical properties of epitaxial $SrCoO_{2.5}$ thin films can be tuned by introducing epitaxial strain. Very recently, Song *et al.*[2] reported that brownmillerite $SrCoO_{2.5}$ films with different crystallographic orientations exhibited strongly anisotropic electrical conductivity. These reports suggest that the location of the E_F in the electronic structure of the $SrCoO_{2.5}$ films can be modulated if they are heteroepitaxially grown on ABO_3 substrates with different lattice mismatches[3]. To utilize the versatile properties and understand the fundamental electronic structure of $SrCoO_{2.5}$, it is essential to evaluate the location of the E_F and its dependence

on strain state, even if the shift is extremely small. In order to clarify the electronic structure of $SrCoO_{2.5}$, high power light sources such as electron beam or X-ray are usually used, and the obtained data are compared with the calculation based on the density functional theory (DFT). Since the data collection is usually performed in the vacuum chamber, there is a possibility that the $SrCoO_{2.5}$ samples release lattice oxygen or adsorb oxygen in the vacuum chamber, and the reduction of the transition metal ion occurs, which affects the electronic structure and the oxidation state of the transition metal ion. Therefore, analysis without vacuum requirement is appropriate to analyze the electronic structure of $SrCoO_{2.5}$. According to the relationship between E_F and S, the thermopower measurement is an indirect probe to observe the changes in electronic structure because vacuum condition is not mandatory.[4]

In this chapter, through a selection of ABO_3-type single crystalline substrates (i.e. $SrTiO_3$, $LaAlO_3$, $(LaAlO_3)_{0.3}(SrAl_{0.5}Ta_{0.5}O_3)_{0.7}$, *etc.*), the lattice strains in $SrCoO_{2.5}$ epitaxial thin films were modulated, and using thermopower measurements, the resulting physical properties were associated with a small shifting in E_F, which can affect electrical properties significantly. This chapter establishes the proof of concept that $SrCoO_{2.5}$ is an excellent candidate as the active material for advanced memory applications.

3.2 Experimental

$SrCoO_{2.5}$ films were heteroepitaxially grown on (001) ABO_3 single crystal substrates by

PLD. During the film deposition, the substrate temperature was kept at 750 °C, and the oxygen pressure was kept at 10 Pa. KrF excimer laser pulses (~2 J cm^{-2} pulse^{-1}, 10 Hz) were irradiated on ceramic targets. All film thicknesses were ~50 nm. The atomic arrangement around the film/substrate interface was observed using STEM operated at 200 keV. HAADF images were taken with detection angle of 68 – 280 mrad. XPS spectra were obtained to address the valence state of Co ions. XAS around the Co $L_{2,3}$ edges of the films were also obtained to thoroughly assess the electronic structure. In order to measure the *S* accurately, a large temperature difference (ΔT = 10 – 18 K) was introduced to the films (surface area: 10 mm × 10 mm).

3.3 Results and discussion

Heteroepitaxial growth of $SrCoO_{2.5}$ was confirmed using RHEED and XRD measurements, and the crystallographic texture was mostly (001)[100] $SrCoO_{2.5}$ || (001)[100] ABO_3. **Figure 3-1** shows the X-ray reciprocal space mappings (RSMs) around 103 diffraction spots of the substrates as well as the resultant $SrCoO_{2.5}$ films, which were used to analyze the lattice parameters in the in-plane direction (*a*) and the out-of-plane direction (*c*). **Figures 3-2(a) and 2(b)** show the extracted lattice parameters *a* and *c*, respectively. Only the films on $SrTiO_3$, LSAT, and $NdGaO_3$ show coherent epitaxial growth, of which the *a* lattice parameter agrees with that of the substrate. Since $SrTiO_3$ lattice is perfectly matched with $SrCoO_{2.5}$, only the films on LSAT and $NdGaO_3$ substrates exhibit compressive in-plane strain. The lattice parameters of the $SrCoO_{2.5}$

films on $DyScO_3$, $LaAlO_3$, and $YAlO_3$ were different from the bulk single crystal values. The interface structures of $SrCoO_{2.5}$ on different substrates observed from cross-sectional HAADF-STEM are shown in **Figure 3-3(a)–(d)**. The atomic arrangement of the $SrCoO_{2.5}$ film grown on (001) $SrTiO_3$ is coherent with $SrTiO_3$ without any dislocations (**Figure 3-3(a)**). On the other hand, $SrCoO_{2.5}$ on $YAlO_3$ is accompanied by misfit dislocations (arrows) at the interface every ~7 nm, which corresponds to the lattice mismatch (~5 %) (**Figure 3-3(b)**). This indicates that the lattice of the $SrCoO_{2.5}$ on $YAlO_3$ is fully relaxed. Furthermore, *a*-axis orientated domains (**Figure 3-3(d)**) with *c*-axis orientation (**Figure 3-3(c)**) were observed in the $SrCoO_{2.5}$ film on $DyScO_3$ substrate. Despite the coexistence of two crystallographic orientations, the film/substrate interface was coherent.

Figures 3-2(c)–2(h) show topographic AFM images of the resultant $SrCoO_{2.5}$ films (2 μm × 2μm). While an atomically flat terraced and stepped surface is seen from the $SrCoO_{2.5}$ film on $SrTiO_3$ **(Figure 3-2(d))**, the surface of other films shows intergranular features. The grain size of the films on $DyScO_3$ **(Figure 3-2(c))** is ~0.15 μm, LSAT **(Figure 3-2(e))** is ~0.3 μm, $NdGaO_3$ **(Figure 3-2(f))** is 0.1−0.3 μm, $LaAlO_3$ **(Figure 3-2(g))** is 0.2−0.3 μm, and $YAlO_3$ **(Figure 3-2(h))** is ~0.1 μm. The grain formation on LSAT, $NdGaO_3$, and $LaAlO_3$ is likely due to spiral growth of the $SrCoO_{2.5}$ domain, whereas that on $DyScO_3$ and $YAlO_3$ is due to the formation of misfit dislocations. The

difference in the surface morphology is likely attributed to the difference in the initial film growth mechanism of $SrCoO_{2.5}$ due to the lattice mismatch.

Figure 3-4(a) shows the change in the *S* of the $SrCoO_{2.5}$ films (blue symbols: as-grown, red symbols: after annealing at 300 °C in the air) measured at room temperature. The *S* of the as-grown $SrCoO_{2.5}$ film on LSAT substrate was +230 μV K^{-1}, close to the previously reported value (+254 μV K^{-1}).[4,5] However, $SrCoO_{2.5}$ films on other substrates showed different *S* values, as they tend to decrease with decreasing substate lattice parameter. It is interesting to note that anomalously large change in thermopower from +330 μV K^{-1} (−69 μV K^{-1} after annealing at 300 °C in the air) on $SrTiO_3$ to −185 μV K^{-1} (−348 μV K^{-1} after annealing at 300 °C in the air) on $YAlO_3$ was observed. These results indicate a shift in the E_F in the valence band occurred as schematically shown in **Figure 3-4(b)** and **Figure 3-4(c)**. The reduction of thermopower after air annealing indicates a unidirectional change in the curvature by the reduction of the number of electrons in Co for the films.

The origin of anomalously large changes in *S* can be assessed in the following manner: the lattice parameters of the $SrCoO_{2.5}$ film on $SrTiO_3$ substrate matched with those of the bulk, and the peak position of Co $L_{2,3}$ edge in the EELS spectra (data did not show) was not different among the samples. Therefore, the chemical composition of the resultant

films was close to being stoichiometric. The XRD patterns of the $SrCoO_{2.5}$ films before and after 300 °C annealing are almost the same, confirming the lattice of film did not change after the annealing. In addition, the electrical resistivity showed no clear tendency related to the lattice mismatch (**Figure 3-5**), which estimated the effect of lattice strain is small. Since the grain size weakly decreases with decreasing lattice mismatch (**Figures 3-2(c) − 2(h), Figure 3-6,** and **Table 3-1**), the specific surface area of the $SrCoO_{2.5}$ film grown on lattice-mismatched substrate is considered to be larger than that of the same film on lattice-matched substrate. These observations lead to the following hypotheses. (1) The $SrCoO_{2.5}$ films grown on lattice-mismatched substrate adsorb oxygen gas due to their large specific surface area. (2) The adsorbed oxygen takes electrons away from the $SrCoO_{2.5}$ film, which oxidizes Co ions and lowers E_F. (3) The oxygen adsorption would strongly occur at 300 °C in air.

The hypothesis can be verified with the oxidation state of Co ion from XPS and electron yield (EY) mode XAS (**Figure 3-7**). Tiny peak energy shift of both Co L_3 and L_2 edges were observed. With decreasing the substrate lattice parameter, the peak energy increases (**Figure 3-7(c))**, indicating the stabilization of higher Co valence state.[5,6] Since the XPS and EY mode XAS measurements are sensitive to sample surface, these results indicate oxygen adsorption at the film surface tends to occur when the lattice parameter of the substrate is small.

Hypothesis (3) can be verified by annealing $SrCoO_{2.5}$ films on (001) LSAT substrates at various temperatures (T_A) in the air for 10 min and measuring the resultant XRD patterns, resistivity, and *S* at room temperature. The peak position and the shape of the out-of-plane XRD pattern of the $SrCoO_{2.5}$ film did not change after the annealing while the change in resistivity was small (10 − 29 Ω cm). **Figure 3-4(d)** plots the change in the *S* of the annealed $SrCoO_{2.5}$ films at room temperature. Positive *S*-values were observed when the T_A was below 130 °C (region A) and above 320 °C (region C) whereas negative *S* values were observed when T_A was in the range from 130 – 320 °C (region B). These results indicate that the E_F shifts in the Co^o DOS upon the thermal annealing as schematically shown in **Figure 3-4(e)**. In region A, the E_F is located higher energy side of the Co^o DOS, showing positive *S* (~+140 μV K^{-1}). When T_A is in region B, the E_F shifts to the lower energy side with negative *S*. When T_A is in region C, the E_F returns to the higher energy side. There are two critical temperatures: 130 °C and 320 °C. The former is due to oxygen adsorption after vaporization of water molecules from the surface while the latter is most likely oxygen desorption from the surface of the $SrCoO_{2.5}$ film.[7-9]

More sophisticated assessment of the electronic structure can be achieved by analyzing the optical conductivity. As schematically shown in **Figure 3-8(a)**, several optical absorption peaks are present in $SrCoO_{2.5}$.[1,10,11] The bandgap (~0.35 eV) is the d–d transition from occupied Co^o to unoccupied Co^o. Another d–d transition from occupied Co^o to unoccupied Co^t can be α or α'[11] transition. The charge transfer transition from

occupied O 2p to unoccupied Co^t is called β transition. The optical conductivity results are shown in **Figure 3-8(b) – 8(g)**. Three absorption peaks of α' (~1.1 eV[11]), α (~1.4 eV) and β (~2.5 eV) are seen. The E_F of $SrCoO_{2.5}$ is located around the occupied Co^o, which mainly constitutes the valence band. It can be noted that the peak area of α' increases with decreasing the lattice parameter of the substrate. This indicates that the occupied Co^o state around the E_F increases with decreasing the lattice parameter of the substrate.

Figure 3-9 schematically illustrates the E_F in the electronic structure of the $SrCoO_{2.5}$ films on lattice-matched $SrTiO_3$ and lattice-mismatched $YAlO_3$. A tiny position of Co^o is unoccupied at the top of the valence band. Since the DOS of Co^o is small, the E_F can be modulated by the oxygen adsorption and the resulting free electron loss. When the E_F is located on the higher energy side of the Co^o state (**Figure 3-9(a)**), positive *S* is observed. On the other hand, when the E_F is located on the lower energy side of the Co^o state (**Figure 3-9(b)**), negative *S* is observed. Since the lattice mismatch largely affects the formation of misfit dislocations and the surface morphology of the resultant $SrCoO_{2.5}$ films, the oxygen adsorption tends to occur when the lattice mismatch is large. Hence, the *S*-value exhibits some dependence on the lattice mismatch. The adsorbed oxygen takes free electrons away from the film, and the E_F shifts to the lower energy side. Therefore, the *S* tends to decrease with decreasing the substrate lattice parameter. Although the X-ray spectroscopy analyses revealed the difference of the oxidation state of the Co ions among

the samples is very small, this tiny difference was detected by the thermopower, clearly showing that thermopower is an excellent measure for analyzing the location of E_F in the electronic structure of $SrCoO_{2.5}$ in a practical manner.

In memory devices, tiny changes in the physical properties need to be detected and recorded with simple measuring techniques. In this regard, thermopower can be utilized to detect the tiny electronic structure variations due to its high sensitivity and easy accessibility. The tiny changes in electronic configuration could be reflected not only by the magnitude of thermopower but also by the sign of value. Therefore, the utilization of thermopower measurement will be promising in characterizing materials for memory applications.

3.4 Conclusion

This chapter showed that the location of the E_F and the shape of the Co^o state in the electronic structure of $SrCoO_{2.5}$ films on various lattice-mismatched substrates can be visualized by measuring the thermopower. The microstructure analyses and the thermal annealing results revealed that the lattice mismatch caused the reduction of the grain size, which resulted in the slight increase of the oxidation state of the Co ions from an increase in the amount of adsorbed oxygen. Although the X-ray spectroscopy analyses revealed the difference in the oxidation state of the Co ions among the samples is small, unusually large change of the thermopower from +330 μV K^{-1} (lattice-matched $SrTiO_3$ substrate)

to −185 μV K^{-1} (lattice-mismatched $YAlO_3$ substrate) was observed due to E_F shifting to the lower energy side. The present results clearly demonstrate the excellent sensitivity of thermopower for analyzing the location of E_F in the electronic structure of $SrCoO_{2.5}$ in practical environments. In addition, the huge changes in thermopower values by fractional changes of Co valence state, while keeping its crystal structure, is promising for characterizing materials for memory applications.

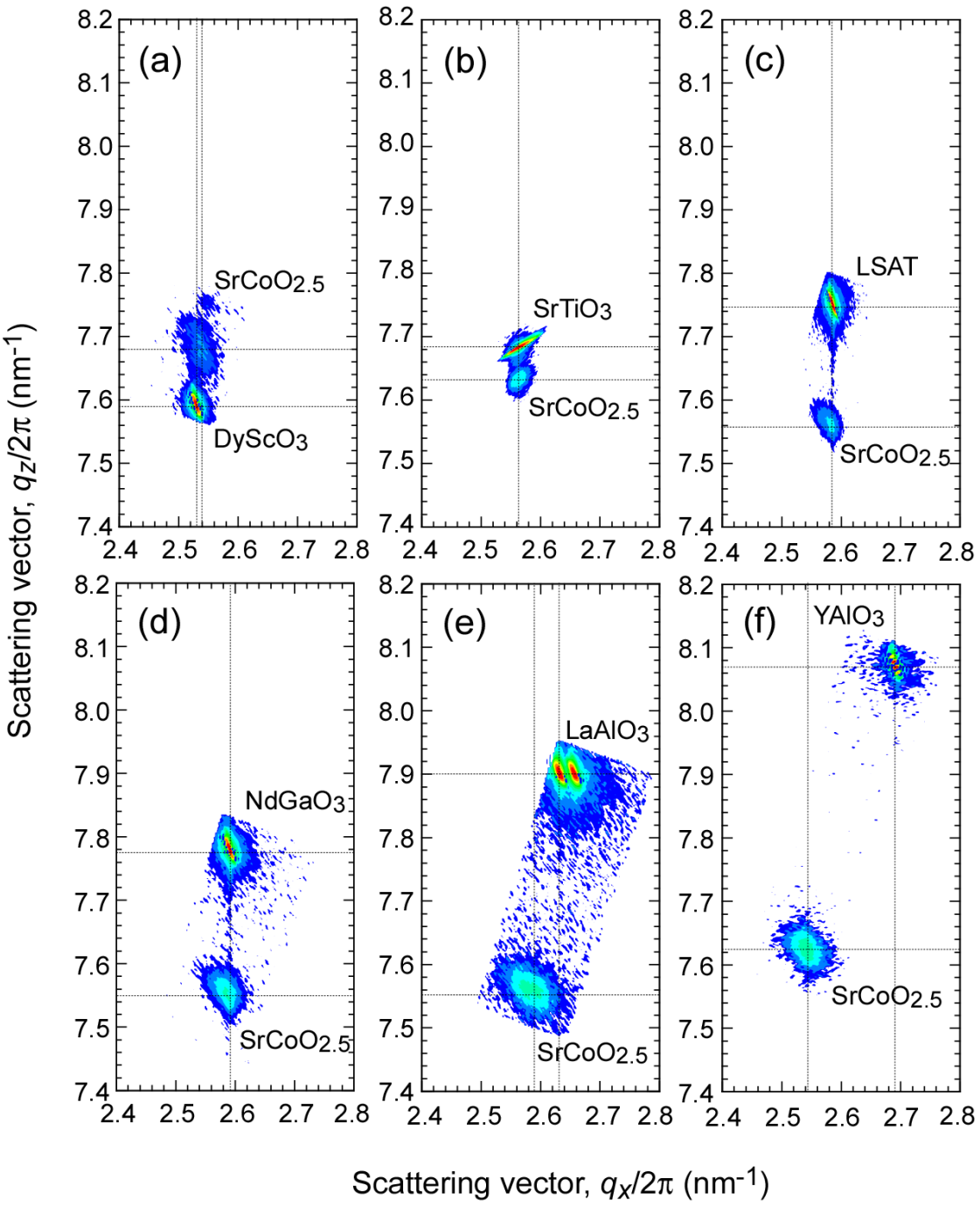

Figure 3-1. X-ray reciprocal space mappings around 103 diffraction spots of the substrates. The solid lines indicate the peak positions. Coherent epitaxial growth occurred only on $SrTiO_3$, LSAT, and $NdGaO_3$ substrates.

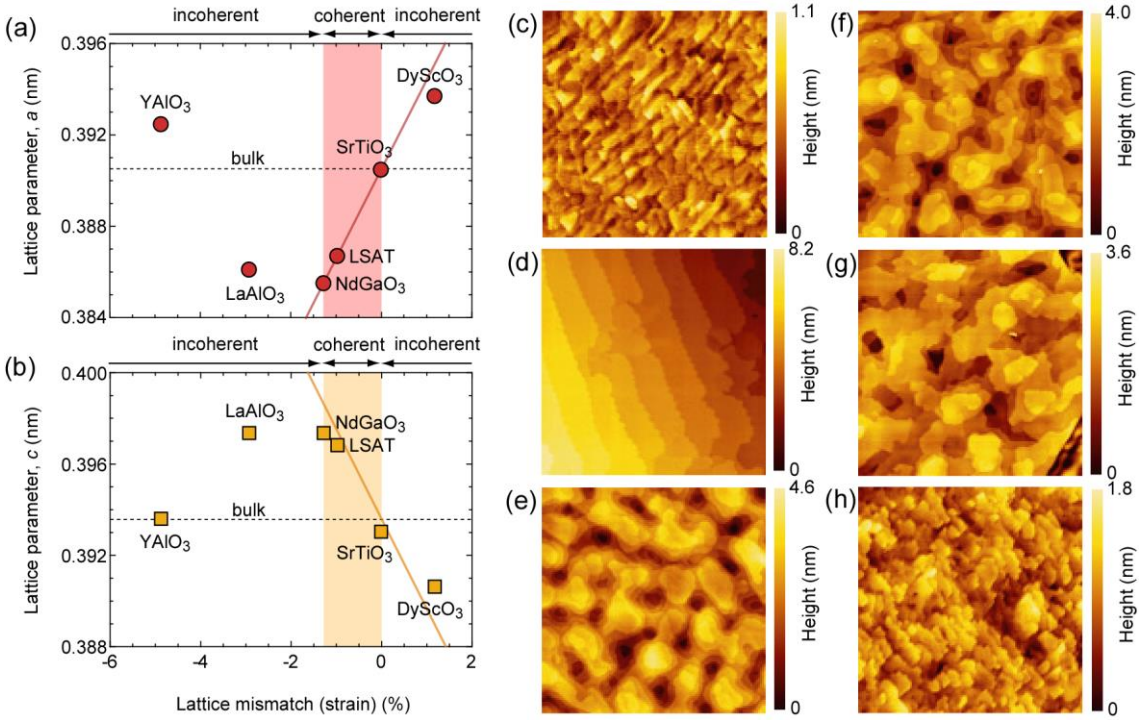

Figure 3-2. Lattice parameters of (a) *a* and (b) *c* for the $SrCoO_{2.5}$ films grown on lattice-mismatched substrates. Dotted lines show the bulk values. Solid lines indicate the ideal coherent growth of the film. Only the films on $SrTiO_3$, LSAT, and $NdGaO_3$ show coherent epitaxial growth. (c) – (h) Topographic AFM images (2 μm × 2μm) of the $SrCoO_{2.5}$ films grown on (c) $DyScO_3$, (d) $SrTiO_3$, (e) LSAT, (f) $NdGaO_3$, (g) $LaAlO_3$, and (h) $YAlO_3$ substrates. Atomically flat terraced and stepped surface is seen in the $SrCoO_{2.5}$ film on $SrTiO_3$. The grain size of the films on $DyScO_3$ is ~0.15 μm, on LSAT is ~0.3 μm, on $NdGaO_3$ is 0.1 − 0.3 μm, on $LaAlO_3$ is 0.2 − 0.3 μm, and on $YAlO_3$ is ~0.1 μm.

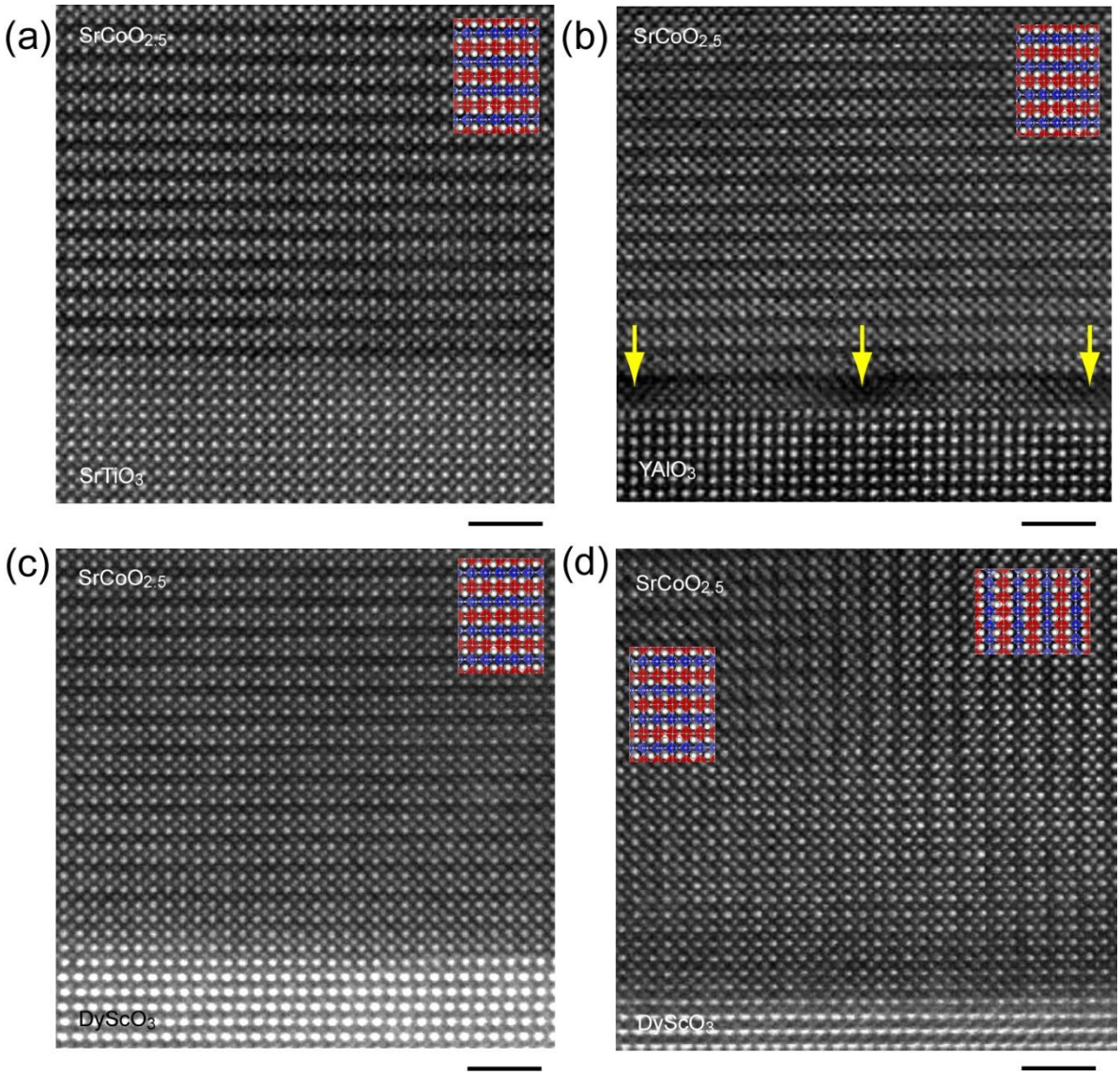

Figure 3-3. Cross-sectional HAADF-STEM images of the $SrCoO_{2.5}$ film/substrate interfaces on (a) $SrTiO_3$, (b) $YAlO_3$, and (c and d) $DyScO_3$ substrates. The scale bar is 2 nm. The schematic crystal structure is also shown to visualize the crystallographic orientation of the films. The arrows in (b) indicate the misfit dislocations.

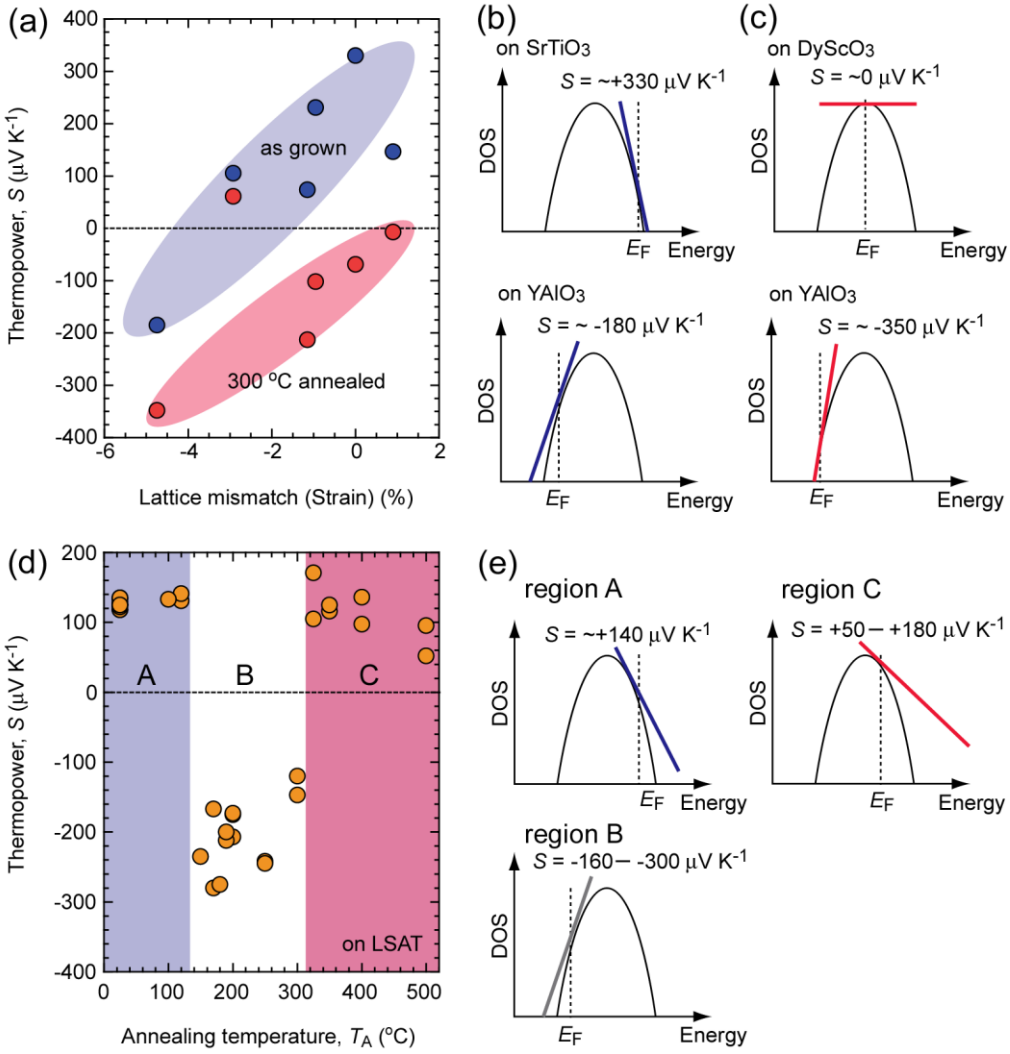

Figure 3-4. (a) Change in the *S* of the SrCoO$_{2.5}$ films (blue symbols: as grown, red symbols: annealed at 300 °C in the air) measured at room temperature. (b) and (c) Schematic energy band diagram of the SrCoO$_{2.5}$ film around the Fermi energy (E_F) [(b) as grown and (c) after 300 °C annealing in the air]. (d) Change in the *S* of the SrCoO$_{2.5}$ film grown on LSAT substrate after annealing at T_A in air. (e) Schematic energy band diagram of the SrCoO$_{2.5}$ film after annealing at the T_A region **A**, **B**, and **C**. The E_F moved upon the thermal annealing.

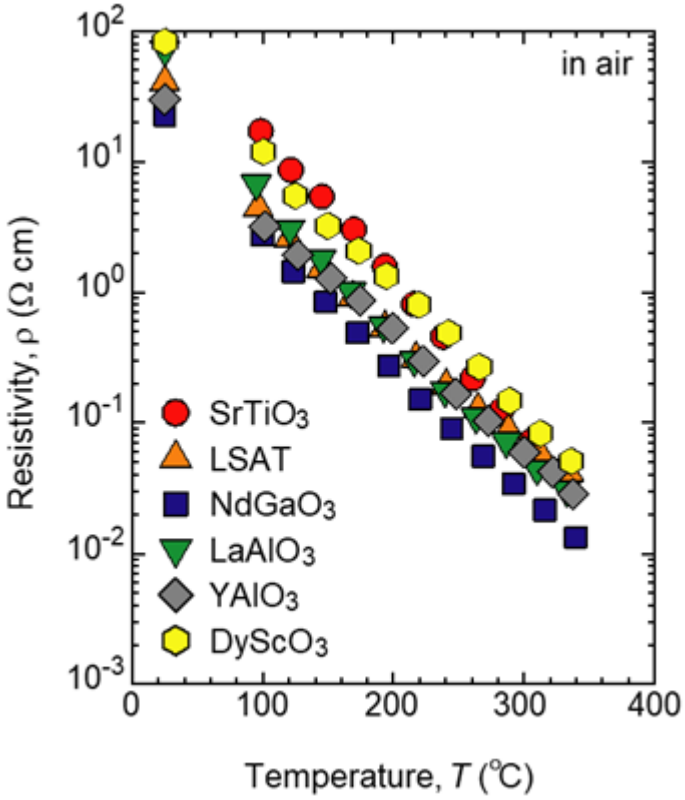

Figure 3-5. Temperature dependence of the resistivity of the $SrCoO_{2.5}$ films grown on various substrates. The resistivity was measured in air. The electrical resistivity showed no clear tendency with the lattice mismatch.

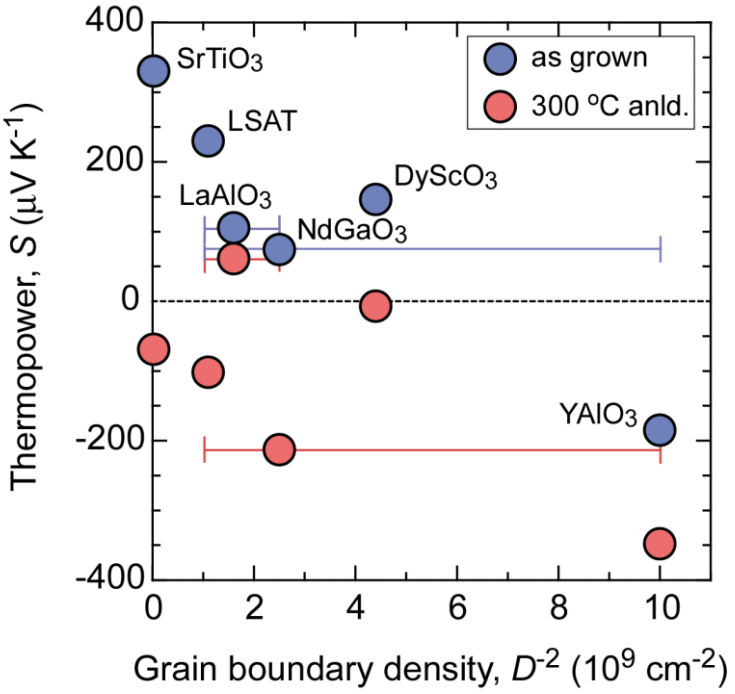

Figure 3-6. Plots of the *S* of the $SrCoO_{2.5}$ films grown on several lattice-mismatched substrates as a function of the grain boundary density, D^{-2}. The grain size (*D*) was extracted from the topographic AFM images. In order to digitize the difference of the specific surface area between the films, the grain boundary density was calculated.

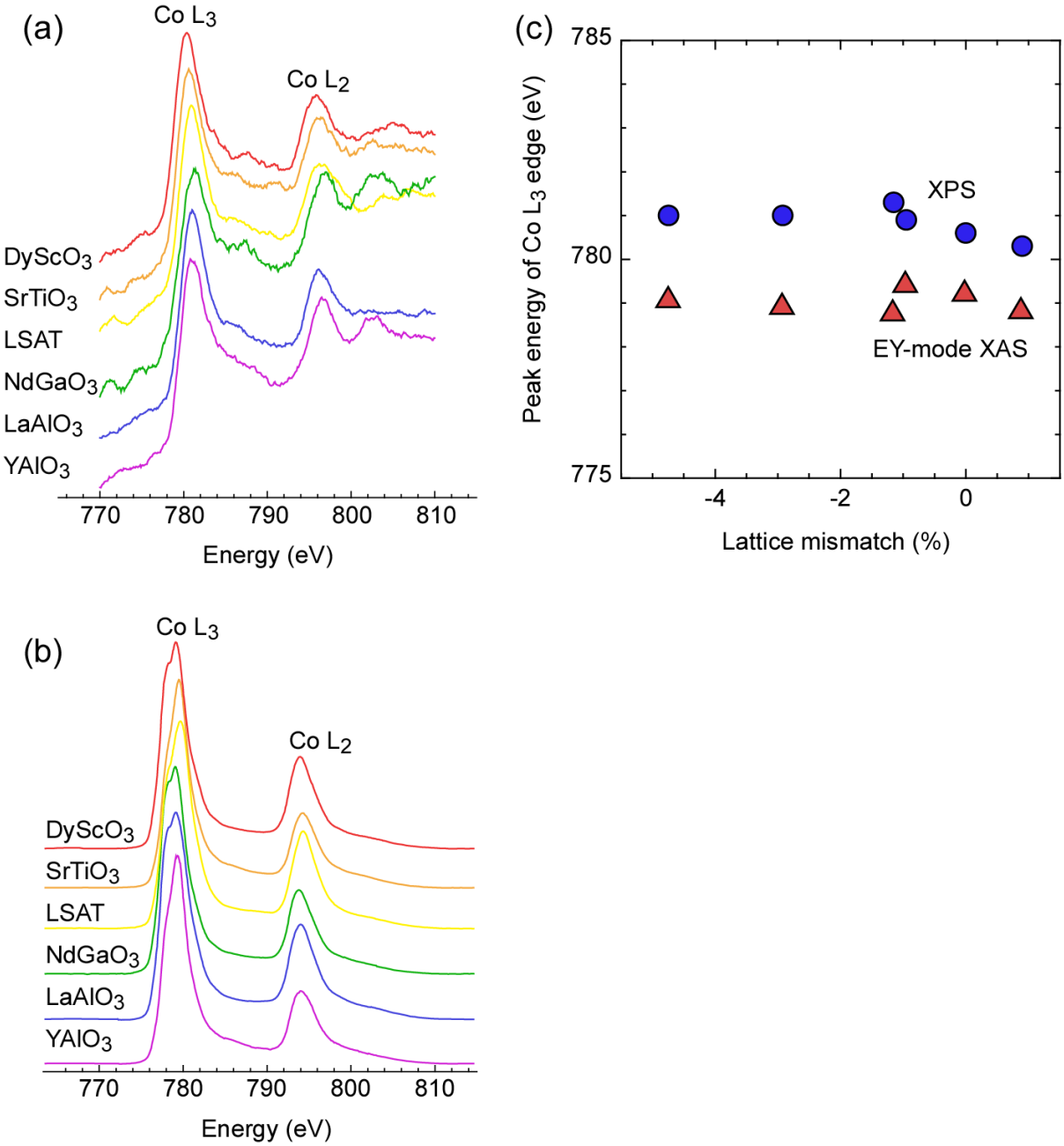

Figure 3-7. Peak energy shift of Co L_3 edge. (a) XPS and (b) EY-mode XAS. (c) The plot of the peak energy of Co L_3 edge as a function of the lattice mismatch. Tiny peak energy shift of both Co L_3 and L_2 edges are observed. Since the XPS and EY mode XAS measurements are sensitive to sample surface, these results indicate oxygen adsorption at the film surface tend to occur when the lattice parameter of the substrate is small.

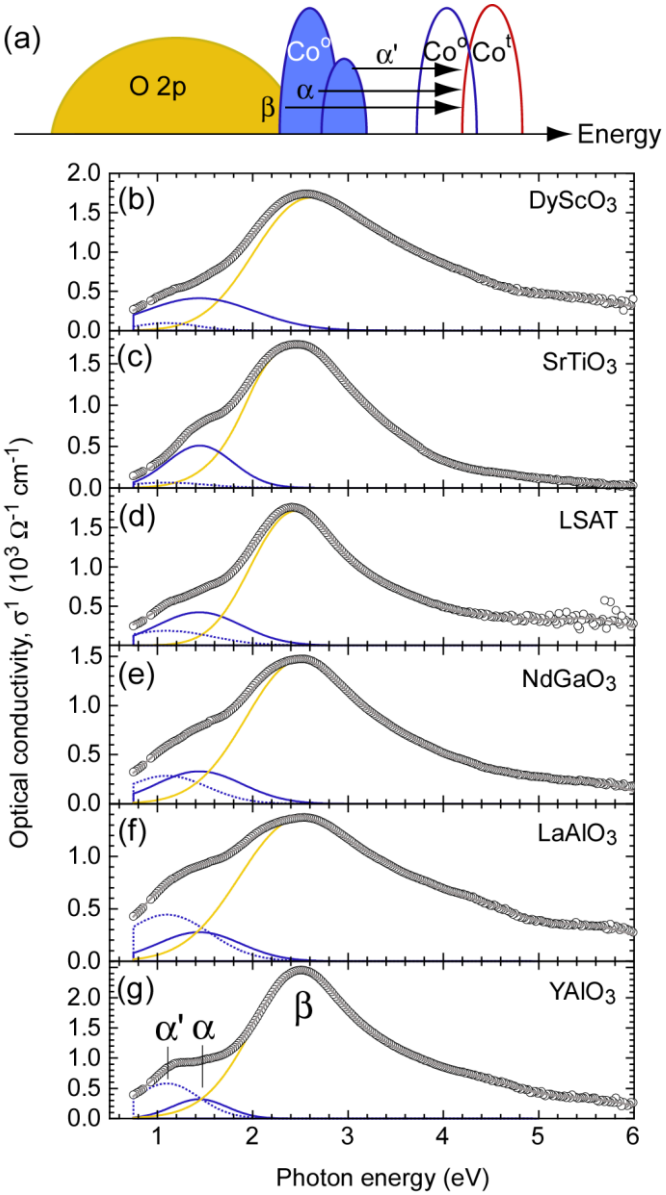

Figure 3-8. (a) Schematic energy band structure of $SrCoO_{2.5}$. The bandgap is ~0.35 eV, which is composed of d−d transition from Co^o to Co^o. In addition to the bandgap, optical absorptions occur at α, α' (d−d transition from Co^o to Co^t), and β (charge transfer transition from O 2p to Co^t). (b−g) Optical conductivity of the $SrCoO_{2.5}$ films (as-grown). The optical absorptions peaking around 1.1 eV (α'), 1.4 eV (α), and around 2.5 eV (β) are seen. Note that the peak area of α' increases with decreasing the lattice parameter of the substrate.

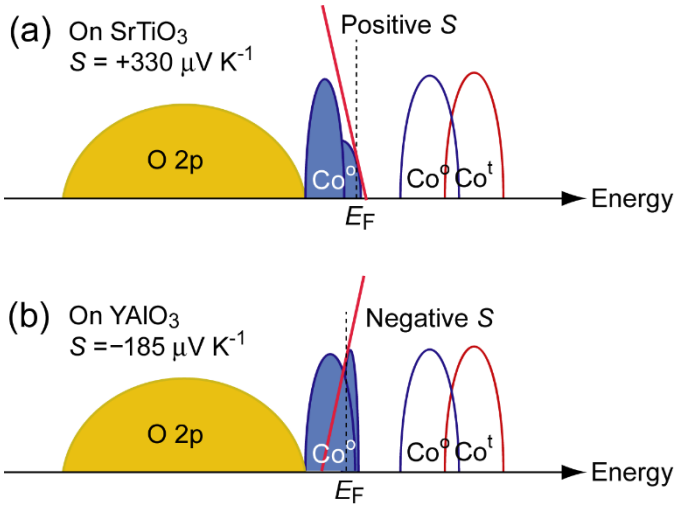

Figure 3-9. Schematic energy band structure of (a) $SrCoO_{2.5}$ on $SrTiO_3$ and (b) on $YAlO_3$ substrates (as-grown). The $SrCoO_{2.5}$ film on $SrTiO_3$ shows positive thermopower (*S*) whereas that on $YAlO_3$ shows negative *S*. The E_F of the $SrCoO_{2.5}$ film on (a) $SrTiO_3$ locates on the higher energy side of α' whereas that on (b) $YAlO_3$ locates on the lower energy side of α'.

Table 3-1. The *S*, Grain size, and Grain boundary density of films on various substrates

Substrate crystal	Grain size, *D* (μm)	Grain boundary density, D^{-2} (cm^{-2})	*S* as-grown (μV K^{-1})	*S* annealed (μV K^{-1})
$DyScO_3$	~0.15	4.4×10^9	+146	−7
$SrTiO_3$	>> 2	<< 2.5×10^7	+330	−69
LSAT	~0.3	1.1×10^9	+230	−102
$NdGaO_3$	0.1 − 0.3	1×10^9–1×10^{10}	+74	−213
$LaAlO_3$	0.2 − 0.3	1×10^9–2.5×10^9	+105	+61
$YAlO_3$	~0.1	1×10^{10}	−185	−348

References

1 Zhao, J. L. *et al.* Manipulating the structural and electronic properties of epitaxial $SrCoO_{2.5}$ thin films by tuning the epitaxial strain. *ACS Appl. Mater. Interfaces* **10**, 10211-10219 (2018).

2 Song, J. H. *et al.* Strong anisotropy and its electric tuning for brownmillerite $SrCoO_{2.5}$ films with different crystal orientations. *Phys. Rev. Mater.* **3**, 045801 (2019).

3 Biswas, A. *et al*. Atomically flat single terminated oxide substrate surfaces. *Prog. Surf. Sci.* **92**, 117-141 (2017).

4 Cutler, M. *et al*. Observation of Anderson localization in an electron gas. *Phys. Rev.* **181**, 1336 (1969).

5 Jeen, H. *et al.* Reversible redox reactions in an epitaxially stabilized $SrCoO_x$ oxygen sponge. *Nat. Mater.* **12**, 1057 (2013).

6 Jeen, H. *et al.* Topotactic Phase Transformation of the Brownmillerite $SrCoO_{2.5}$ to the Perovskite $SrCoO_{3-\delta}$. *Adv. Mater.* **25**, 3651-3656 (2013).

7 Higuchi, K. *et al*. Molecular and Dissociative Adsorption of Oxygen on Solid Oxide Fuel Cell Cathode Materials of $La_{1-x}Sr_xCoO_3$, $La_{1-x}Sr_xCo_{1-y}Fe_yO_3$, and $La_{1-x}Sr_xMnO_3$ Studied by Temperature-Programmed Desorption. *J. Phys. Chem. C* **121**, 14581-14588 (2017).

8 Wang, J. *et al*. Ta-Doped $SrCoO_{3-\delta}$ as a promising bifunctional oxygen electrode for reversible solid oxide fuel cells: a focused study on stability. *J. Mater. Chem. A* **5**, 8989-9002 (2017).

9 Wang, J. *et al*. A new defect chemistry model for Nb-doped $SrCoO_{2.5+\delta}$: The role of oxygen interstitials and delocalized-to-localized electron holes. *J. Solid State Chem.* **246**, 97-106 (2017).

10 Choi, W. S. *et al.* Reversal of the lattice structure in $SrCoO_x$ epitaxial thin films studied by real-time optical spectroscopy and first-principles calculations. *Phys. Rev. Lett.* **111**, 097401 (2013).

11 Lee, J. H. *et al.* Strongly coupled magnetic and electronic transitions in multivalent strontium cobaltites. *Sci. Rep.* **7**, 16066 (2017).

Chapter 4. Solid-State Electrochemical Protonation of $SrCoO_{2.5}$ into $H_xSrCoO_{2.5}$ (x = 1, 1.5 and 2)

4.1 Objective of this Chapter

In Chapter 3, strain-sensitive electronic properties in $SrCoO_x$ system and the respective E_F changes were visualized by thermopower measurement. However, strain engineering is usually not reversible and therefore, cannot be utilized in memory applications. In this regard, ionic defect engineering such as non-stoichiometry and proton doping in this material can be considered since it also can significantly influence the electronic structure and physical properties. For example, metal-to-insulator, antiferromagnetic-to-ferromagnetic, and transparent-to-opaque transitions induced by electrochemical protonation/oxidation of $SrCoO_x$ all have strong potential in memory applications. Therefore, scientists turned to the investigation of the physical property change of $SrCoO_x$ during the topotactic phase transition induced by electrochemical protonation. However, previous approaches were limited by the use of liquid electrolyte[1,2] or strong alkalinity in the electrolyte[3], which prevented protonation.

To overcome these problems, this chapter focuses on the solid-state electrochemical protonation of $SrCoO_{2.5}$ into $H_2SrCoO_{2.5}$ using a mesoporous amorphous $12CaO{\cdot}7Al_2O_3$ (CAN)[4,5] film as the solid electrolyte. Since CAN film could provide H^+ for the electrochemical protonation, the crystalline phase was successfully modulated from

$SrCoO_{2.5}$ to $HSrCoO_{2.5}$ (phase A), $H_{1.5}SrCoO_{2.5}$ (phase B), and $H_2SrCoO_{2.5}$ (phase C) through the formation of an intermediate phase of $H_{1.25}SrCoO_{2.5}$. The physical properties of these phases are extensively discussed.

4.2 Experimental

Two-terminal electrochemical cells were fabricated by a pulsed laser deposition (PLD) technique with stencil masks (**Figure 4-1**). First, ~30-nm-thick 10 mol% Nb-doped $SrTiO_3$ films were heteroepitaxially grown on (001)-oriented $SrTiO_3$ substrate (10 mm × 10 mm × 0.5 mm) at the substrate temperature of 900 °C in an oxygen atmosphere (1 × 10^{-3} Pa). Second, ~50-nm-thick $SrCoO_{2.5}$ active layers were heteroepitaxially grown on the Nb-doped $SrTiO_3$ films with stencil mask (2.25 mm × 2.25 mm) at the substrate temperature of 850 °C in an oxygen atmosphere (10 Pa). Then, ~300-nm-thick mesoporous CAN was deposited on the $SrCoO_{2.5}$ film at room temperature as the solid electrolyte. Finally, ~30-nm-thick ITO film was deposited as the top electrode at room temperature.

Electrochemical protonation of $SrCoO_{2.5}$ films was performed at room temperature in air as schematically shown in (**Figure 4-1**). When a constant voltage of +10 V was applied using a source meter (Model 2450, Keithley), the $SrCoO_{2.5}$ film was converted into $H_xSrCoO_{2.5}$ film within several hours. After applying the bias voltage using gold-coated probes, all the *in-situ* XRD patterns were measured at room temperature in air. Each scan

took about 5 minutes and was plotted in a two-dimensional contour diagram. The magnetic moments of samples were measured at 10−300 K with 100 Oe field using a SQUID magnetometer (MPMS3, Quantum Design). To check the change in magnetic properties, magnetic hysteresis loops (*M* vs. *H* curves) were measured up to 7 T at 10 K. Then, secondary-ion mass spectrometry (SIMS) was performed to obtain the hydrogen concentration in the protonated sample (Front Side SIMS, PHI, 6800). Cs^+ primary ion beam (2 keV) was scanned, and data were collected in an area from 40 × 40 μm. The hydrogen concentration was quantitatively analyzed by profiling proton-embedded silica with known H^+ doses.

4.3 Results and discussion

The changes in the *in-situ* out-of-plane XRD pattern of the device during protonation are shown in **Figure 4-2(a)**. The flowing current density (*J*) to the solid-state electrochemical cell during the voltage application is also shown (**Figure 4-2(b)**). Before the protonation (0 min), the 008 diffraction peak of BM-$SrCoO_{2.5}$ (008_{BM}) is seen together with 002 $SrTiO_3$ substrate (002s). Approximately 40 min after starting the protonation, 008 diffraction peak of $HSrCoO_{2.5}$ (008_A) appears, and the intensity of 008_{BM} becomes weak. Simultaneously, the *J* dropped from ~5 mA cm^{-2} to ~4 mA cm^{-2}. Approximately 100 mins after the protonation, the 008 diffraction peak of $H_{1.5}SrCoO_{2.5}$ (008_B) appears together with the diffraction peak of an intermediate phase, which will be described later. Approximately 260 mins after the protonation, the 008 diffraction peak of $H_2SrCoO_{2.5}$

(008_C) appears. Simultaneously, the diffraction peaks of 008_A and the intermediate phase disappear. The *J* gradually decreased from ~3.6 mA cm^{-2} to ~0.3 mA cm^{-2}. These results indicate that solid-state protonation is possible by using CAN as the solid electrolyte.

In order to clarify the diffraction peak of the intermediate phase, the out-of-plane XRD patterns of another solid-state electrochemical cell after protonation were measured (**Figure 4-2(c)**). At 0 min, the 00*l* diffraction peaks of BM-$SrCoO_{2.5}$ are seen together with those of 00*l* $SrTiO_3$ substrate, indicating strong *c*-axis orientation of the BM-$SrCoO_{2.5}$ film. After the protonation, the diffraction peak position changes discretely from $q_z/2\pi = (0.6346 \times l)$ nm^{-1} (BM-$SrCoO_{2.5}$) to $(0.6091 \times l)$ nm^{-1} ($HSrCoO_{2.5}$, A), $(0.5968 \times l)$ nm^{-1} ($H_{1.5}SrCoO_{2.5}$, B), and $(0.5845 \times l)$ nm^{-1} ($H_2SrCoO_{2.5}$, C) through the formation of the intermediate $H_{1.25}SrCoO_{2.5}$ phase ($q_z/2\pi$ = 1.822, 3.046, 4.253, 5.484, and 6.699 nm^{-1}). **Figure 4-2(d)** summarizes the schematic modification in the crystal structure upon the protonation. The lattice parameter *c* of BM-$SrCoO_{2.5}$ is 1.5751 nm, which agrees well with the reported value (1.5745 nm)[6]. The lattice parameter *c* of phase B is 1.6756 nm, which also agrees well with that of $H_{1.5}SrCoO_{2.5}$ (1.675 nm)[7]. The intermediate $H_{1.25}SrCoO_{2.5}$ phase is a half-filled state in the oxygen vacancy site of $HSrCoO_{2.5}$ (phase A) with an H_2 dimer. Thus, the lattice parameter *c* is two times that of phases A and B.

The hydrogen concentration in the samples measured by SIMS is shown in **Figure 4-3**. The hydrogen concentration of the $H_{1.5}SrCoO_{2.5}$ (phase B) sample is $\sim 2 \times 10^{22}$ cm^{-3}. For

comparison, oxidized $SrCoO_3$ samples were also prepared by applying negative voltage (−10 V) to the solid-state electrochemical cell for 1 h in air. Compared to the as-grown $SrCoO_{2.5}$ sample and oxidized $SrCoO_3$ samples, the $H_{1.5}SrCoO_{2.5}$ (phase B) sample is an order of magnitude higher in the hydrogen concentration. The quantitative hydrogen concentration was estimated to be 1.5 H per chemical formula of $SrCoO_{2.5}$, which is close to the stoichiometry value of $H_{1.5}SrCoO_{2.5}$[7].

Then, the optical transmission spectra of the as-grown BM-$SrCoO_{2.5}$ sample, the protonated $H_{1.5}SrCoO_{2.5}$ (phase B, 240 min) sample, and the oxidized $SrCoO_3$ sample are discussed (**Figure 4-4**). Compared to the BM-$SrCoO_{2.5}$ sample, the $H_{1.5}SrCoO_{2.5}$ (phase B) sample is more transparent in the visible region, whereas the oxidized $SrCoO_3$ sample shows lower transmissivity. The as-grown BM-$SrCoO_{2.5}$ samples are brown, the oxidized $SrCoO_3$ sample is black, and the protonated $H_{1.5}SrCoO_{2.5}$ (phase B) sample is colorless transparent as shown in the inset of **Figure 4-4**. Note that the low transmission in the IR region is due to the absorption of Nb-doped $SrTiO_3$ film. The overall tendency of the color change in the electrochemical cells is similar to the previously reported tendencies in literature[1,8].

The magnetic properties of the solid-state electrochemical cell are shown in **Figure 4-5**. The magnetism of $SrCoO_x$ is closely linked to the concentration of oxygen in the lattice, likely due to the formation of oxygen holes[9,10]. A clear magnetic transition was observed

from the relationship between *M* versus *T* (**Figure 4-5(a)**). The as-grown BM-$SrCoO_{2.5}$ sample did not show any magnetic transition due to its antiferromagnetic ground state. On the other hand, a clear transition is observed in the oxidized $SrCoO_3$ sample. The transition temperature (T_c) is estimated to be ~240 K, which is comparable to the reported T_c of the nearly stoichiometric perovskite $SrCoO_3$[1,11,12]. Further, the protonated $H_{1.5}SrCoO_{2.5}$ (phase B) sample showed a weak ferromagnetic behavior with T_c ~130 K, which is consistent with the reported value[1]. The field-dependent magnetization measurements at 10 K provide the deeper analysis (**Figure 4-5(b)**). The oxidized $SrCoO_3$ sample showed a clear ferromagnetic signal, and the hysteresis loop is clearly seen. The coercive field is estimated to be 500 Oe, which is ~1/4 of that observed from the ionic-liquid case (~2000 Oe[1]). Since the $SrCoO_3$ film is unstable and will lose oxygen in vacuum during the measurement, much lower coercive field than the ideal single crystal value was observed. In contrast, the protonated $H_{1.5}SrCoO_{2.5}$ (phase B) sample has a comparable magnetic moment to ionic-liquid gated $HSrCoO_{2.5}$[1]. These results clearly show that the optical and magnetic properties can be controlled electrochemically at room temperature in the air by using the solid-state electrochemical cells composed of $SrCoO_{2.5}$ and CAN solid electrolyte.

4.4 Conclusion

This chapter demonstrated the solid-state room-temperature electrochemical protonation of $SrCoO_{2.5}$ films in air. All-solid-state electrochemical cells of $SrCoO_{2.5}$ using CAN film

as the solid electrolyte was prepared. During the protonation, the crystalline phase discretely changed from $SrCoO_{2.5}$ to $HSrCoO_{2.5}$, $H_{1.5}SrCoO_{2.5}$, and $H_2SrCoO_{2.5}$ through the formation of an intermediate phase of $H_{1.25}SrCoO_{2.5}$. The $H_{1.5}SrCoO_{2.5}$ sample was colorless-transparent and showed weak ferromagnetism with T_c ~130 K. The present results suggest that the CAN film can be used as the solid electrolyte for the protonation treatment of TMOs, which overcomes the issue faced by previous approaches on the electrochemical treatments of TMOs using liquid electrolyte.

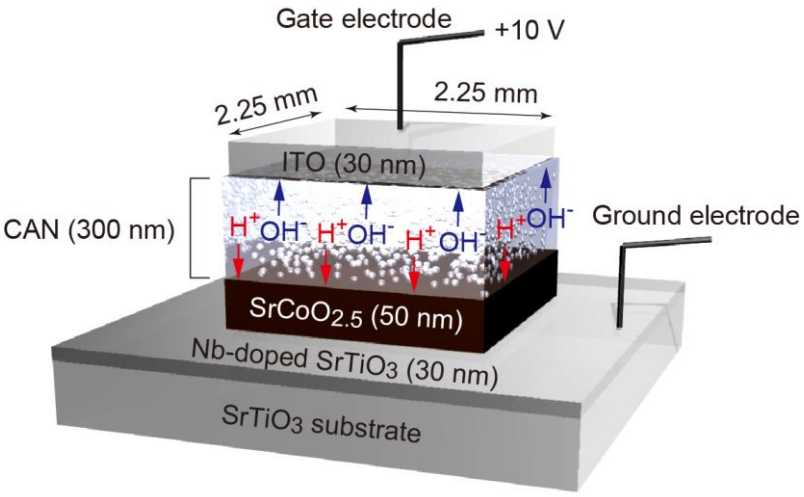

Figure 4-1. Schematic illustration of solid-state electrochemical protonation of $SrCoO_{2.5}$ film. The active area of the electrochemical cell is 2.25 mm × 2.25 mm. +10 V was applied for the protonation. Since CAN film contains ultrapure water, protonation of $SrCoO_{2.5}$ and oxidation of ITO films occurs during +10 V application.

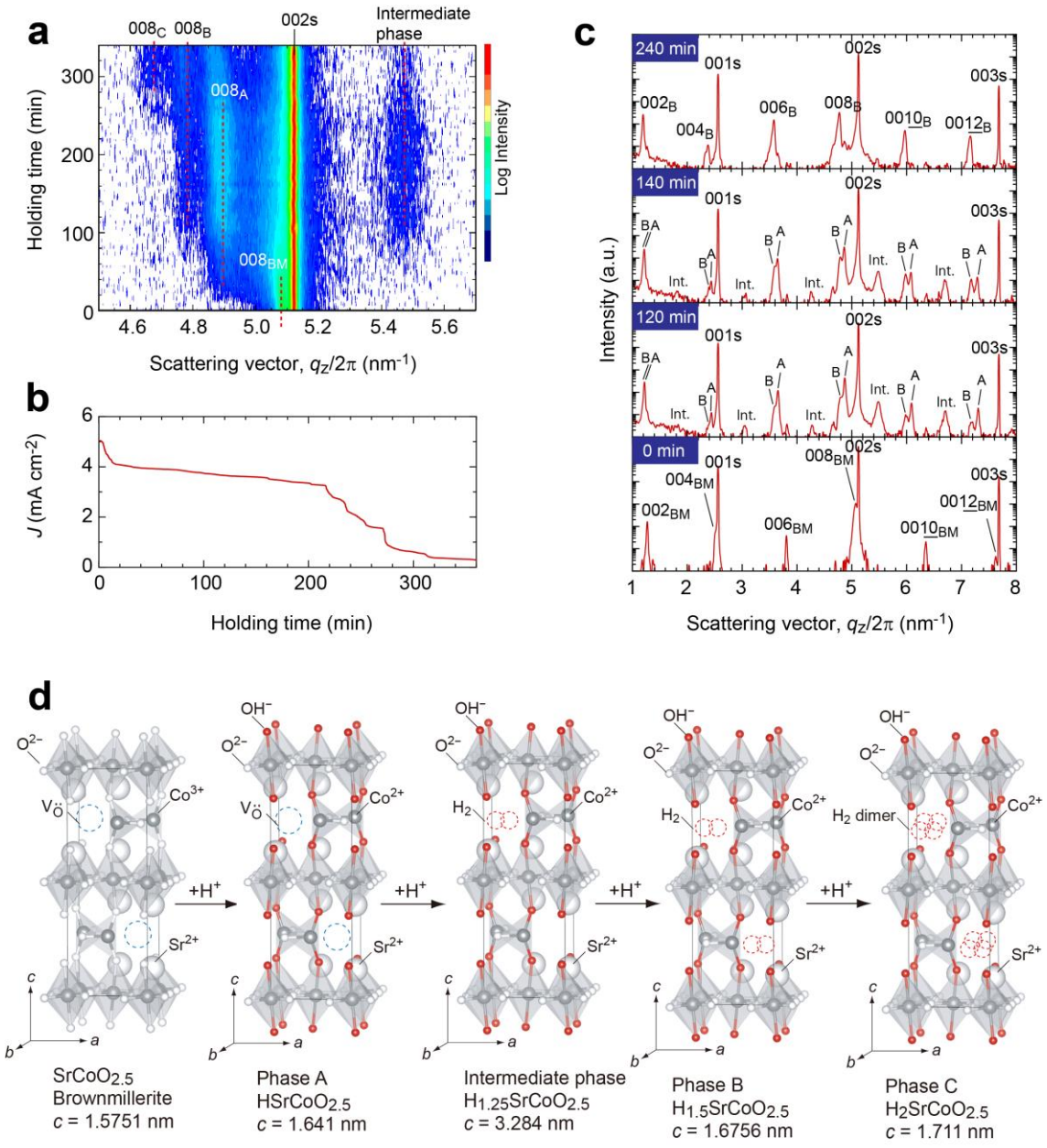

Figure 4-2. Crystal phase modulation during the protonation. (a) Change in the out-of-plane XRD pattern of the solid-state electrochemical cell during the electrochemical protonation treatment. The XRD patterns were taken every 5 min in situ. (b) Change in the current density (J) with holding time. (c) Out-of-plane XRD patterns of the solid-state electrochemical cell (another sample) after the electrochemical protonation treatment. A, B, and Int. denote $HSrCoO_{2.5}$ (phase A), $H_{1.5}SrCoO_{2.5}$ (phase B), and $H_{1.25}SrCoO_{2.5}$ (intermediate phase), respectively. (d) Schematic crystal structure change upon protonation.

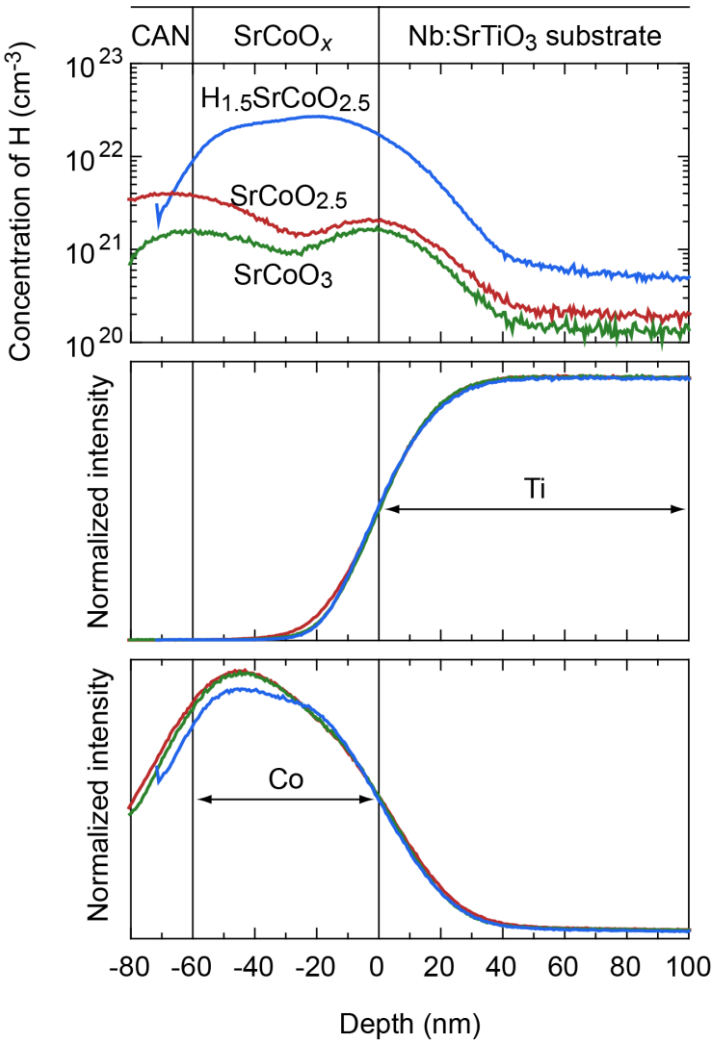

Figure 4-3. Depth profiles of H, Ti, and Co ions of the multilayer samples measured by SIMS (40 μm × 40 μm). The hydrogen concentration of the protonated $H_{1.5}SrCoO_{2.5}$ sample is ~2×10^{22} cm^{-3}, confirming that $H_{1.5}SrCoO_{2.5}$ was formed. Since the film surface of ITO/CAN is rough, the SIMS results do not show a flat profile.

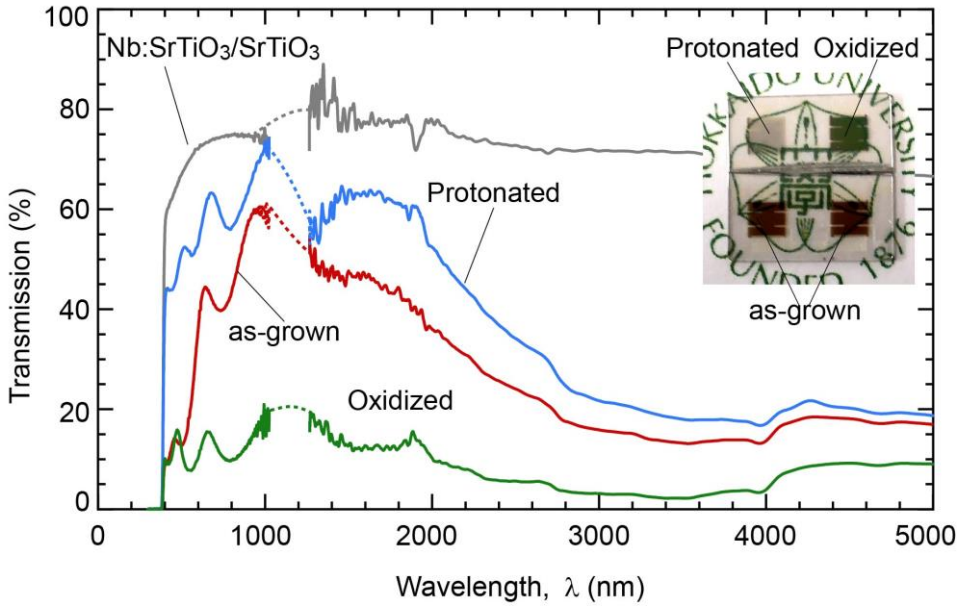

Figure 4-4. Optical transmission spectra of the solid-state electrochemical cells. As-grown: BM-$SrCoO_{2.5}$ sample, Protonated: $H_{1.5}SrCoO_{2.5}$ sample, Oxidized: $SrCoO_3$ sample. The gray line is the reference of Nb-$SrTiO_3$ coated $SrTiO_3$ substrate. The dotted lines were used to connect two different spectrometer results. (Inset) Photograph of the devices. The as-grown BM-$SrCoO_{2.5}$ samples are brown, the protonated $H_{1.5}SrCoO_{2.5}$ sample (240 mins) is colorless transparent, and the oxidized $SrCoO_3$ sample is black, respectively.

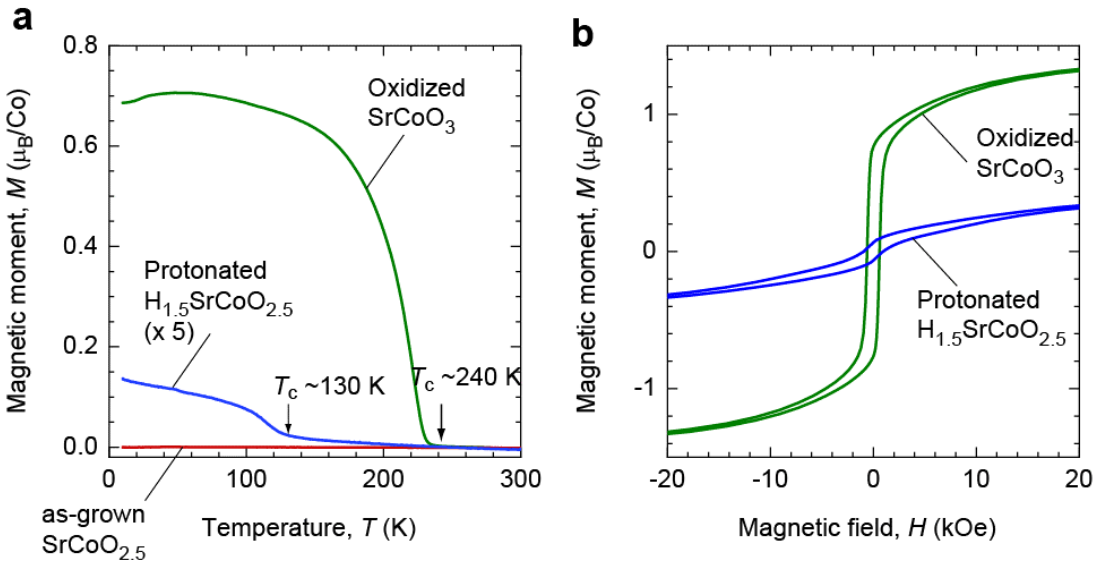

Figure 4-5. (a) Temperature dependence of the magnetization of $SrCoO_x$ layer measured with the magnetic field of 100 Oe. The oxidized $SrCoO_3$ sample shows clear magnetic transition with T_c ~240 K. The protonated $H_{1.5}SrCoO_{2.5}$ sample shows T_c ~130 K. Both T_c values are comparable to the reported values[1]. (b) *M*–*H* curves of the oxidized $SrCoO_3$ sample and the protonated $H_{1.5}SrCoO_{2.5}$ sample measured at 10 K.

References

1 Lu, N. *et al.* Electric-field control of tri-state phase transformation with a selective dual-ion switch. *Nature* **546**, 124-128 (2017).

2 Gao, L. *et al.* Tracing the ionic evolution during ILG induced phase transformation in strontium cobaltite thin films. *J. Phys. Condens. Matter.* **33**, 104004 (2021).

3 Katase, T. *et al*. Reversibly switchable electromagnetic device with leakage-free electrolyte. *Adv. Electron. Mater.* **2**, 1600044 (2016).

4 Ohta, H. *et al.* Field-induced water electrolysis switches an oxide semiconductor from an insulator to a metal. *Nat. Commun.* **1**, 118 (2010).

5 Ohta, H. *et al.* Unusually Large Enhancement of Thermopower in an Electric Field Induced Two-Dimensional Electron Gas. *Adv. Mater.* **24**, 740-744 (2012).

6 de la Calle, C. *et al*. Correlation between reconstructive phase transitions and transport properties from $SrCoO_{2.5}$ brownmillerite: A neutron diffraction study. *Solid State Sci.* **10**, 1924-1935 (2008).

7 Li, H. B. *et al.* Electric Field-Controlled Multistep Proton Evolution in $H_xSrCoO_{2.5}$ with Formation of H-H Dimer. *Adv. Sci.* **6**, 1901432 (2019).

8 Choi, W. S. *et al.* Reversal of the Lattice Structure in $SrCoO_x$ Epitaxial Thin Films Studied by Real-Time Optical Spectroscopy and First-Principles Calculations. *Phys. Rev. Lett.* **111** (2013).

9 Potze, R. *et al*. Possibility for an intermediate-spin ground state in the charge-transfer material $SrCoO_3$. *Phys. Rev. B* **51**, 11501 (1995).

10 Medling, S. *et al.* Evolution of magnetic oxygen states in Sr-doped $LaCoO_3$. *Phys. Rev. Lett.* **109**, 157204 (2012).

11 Jeen, H. *et al.* Reversible redox reactions in an epitaxially stabilized $SrCoO_x$ oxygen sponge. *Nat. Mater.* **12**, 1057-1063 (2013).

12 Jeen, H. *et al.* Topotactic phase transformation of the Brownmillerite $SrCoO_{2.5}$ to the Perovskite $SrCoO_{3-\delta}$. *Adv. Mater.* **25**, 3651 (2013).

Chapter 5. Macroscopic Visualization of Fast Electrochemical Reaction of $SrCoO_x$ Oxygen Sponge

5.1 Objective of this Chapter

Chapter 4 explored the electrochemical phase transition and the respective physical property change of $SrCoO_{2.5}$, which involved protonation. This chapter moves beyond the H^+ doping and explores the ability to control oxygen non-stoichiometry for reversible modulation of the phase and physical properties. Therefore, the rest of the given dissertation focuses on the electrochemical reduction/oxidation of TMOs using YSZ substrate as the solid-electrolyte to tune the oxygen concentration. As schematically shown in **Figure 5-1(a)**, by changing the oxygen contents in $SrCoO_{2.5}$ to form $SrCoO_{3-\delta}$.[1,2], the valence states of cobalt ion change from 3+ into 4+, which has excellent potential for memory applications.

In order to further improve and optimize the device performance, the electrochemical oxidation needs to be visualized macroscopically. Usually, transmission electron microscopy (TEM) observation is used to visualize the electrochemical redox reaction in a material.[3,4] However, TEM cannot be used for $SrCoO_{3-\delta}$ because $SrCoO_{3-\delta}$ easily releases oxygen and becomes $SrCoO_{2.5}$ when an intense electron beam is irradiated. In this regard, conductive atomic force microscopy (AFM) provides an alternate powerful tool for analyzing the conductive region in a material.[5] This chapter addresses the

macroscopic visualization of the electrochemical reaction of $SrCoO_{2.5}$ films on YSZ substrate using conductive AFM. In order to further confirm the electrochemical oxidation mode, the *S* of $SrCoO_x$ film with various oxidation states was also analyzed because *S* is sensitive to the volume of conducting part in a mixed phase of insulating and conducting materials.[6-11]

5.2 Experimental

$SrCoO_{2.5}$ films were heteroepitaxially grown on (001) YSZ single crystal substrate by PLD. During the film deposition, the substrate temperature was kept at 750 °C, and the oxygen pressure was kept at 10 Pa. KrF excimer laser pulses (~2 J cm^{-2} $pulse^{-1}$, 10 Hz) were irradiated onto the ceramic target. First, 6-nm-thick 8 mol% Gd-doped CeO_2 (GDC) buffer layer was grown followed by the growth of ~40-nm-thick $SrCoO_{2.5}$.[12-14]

For the electrochemical oxidation, 55-nm-thick porous Pt film (relative density ~53%) with comb-shaped pattern was deposited on the backside of the YSZ substrate by d.c. sputtering (IB-3, Eiko Co.) at room temperature. Al foil was used as the counter electrode as shown in **Figure 5-1(b)**. In order to oxidize the $SrCoO_{2.5}$ into $SrCoO_{3-\delta}$, the sample was heated at 300 °C in air, and the oxidizing current was applied under −5 V or −10 V. The current density was up to −20 μA cm^{-2}. The electrochemical reaction is denoted by the following formula.

$$SrCoO_{2.5} + 0.5O^{2-} \rightarrow SrCoO_3 + e^-$$

Thus, the electron density of 1.61×10^{22} cm^{-3} is needed to fully oxidize $SrCoO_{2.5}$ into $SrCoO_3$. The required quantity of electricity per unit area was $1.61 \times 10^{22} \times$ (film thickness of $SrCoO_{2.5}$) $\times 1.602 \times 10^{-19} = 9.5$ mC cm^{-2}. The samples were labelled according to the transferred charge as 0.44 mC cm^{-2} (4.6 %) for sample A, 0.88 mC cm^{-2} (9.3 %) for sample B, 2.1 mC cm^{-2} (22 %) for sample C, 4.0 mC cm^{-2} (42 %) for sample D, and 12 mC cm^{-2} (126 %) for sample E, respectively.

5.3 Results and discussion

The XRD of the resultant $SrCoO_x$ films are shown in **Figure 5-2**. Only intense diffraction peaks of 00*l* BM-$SrCoO_{2.5}$ or 00*l* PV-$SrCoO_{3-\delta}$ together with 00*l* GDC / 00*l* YSZ are seen from the out-of-plane XRD patterns (**Figure 5-2(a)**) in all cases, indicating strong *c*-axis orientation of the $SrCoO_x$ films. The as-grown sample was single phase $SrCoO_{2.5}$, and sample E was single phase $SrCoO_{3-\delta}$. Samples A, B, C, and D were mixtures composed of BM-$SrCoO_{2.5}$ and PV-$SrCoO_{3-\delta}$. **Figure 5-2(b)** is the magnified XRD patterns around 008_{BM} or 002_{PV} Bragg peak. From as-grown to sample E, the peak intensity of 008_{BM} decreased, whereas that of 002_{PV} increased. The *d*-spacing of 008_{BM} was 0.1973 nm, and that of 002_{PV} was 0.1910 nm, which is ~3.2 % shorter than 008_{BM} (**Figure 5-3(a) and 3(b)**). From the *d*-spacing of 002_{PV}, the lattice constant of the oxidized film is calculated to be 0.382 nm, which is closed to the lattice constant of $SrCoO_3$ single crystal (0.3829 nm).[15] It should be noted that the average crystal tilting (= full width at half maximum of

the X-ray rocking curve, **Figure 5-3(c) and 3(d)**) of both $SrCoO_{2.5}$ and $SrCoO_{3-\delta}$ films is ~0.7 °, which shows that the oxidization does not change the crystal tilting.

According to the X-ray reflectivity measurements, the thickness of the $SrCoO_{2.5}$ film was 43.9 nm whereas that of the $SrCoO_{3-\delta}$ was 42.5 nm. The film thickness decreased ~3.2 % due to the *d*-spacing decrease, indicating that the $SrCoO_{2.5}$ was fully oxidized into $SrCoO_{3-\delta}$. The thickness of the GDC film was 6 nm, which did not change after the oxidation. In the topographic AFM images, several-hundred-nanometer-sized grain structures were seen from both $SrCoO_{2.5}$ and $SrCoO_{3-\delta}$ films, showing that their surface morphologies are essentially the same. Bright streaks in the RHEED pattern indicate that the $SrCoO_{2.5}$ was heteroepitaxially grown on the substrate with smooth surface. These results indicate that electrochemical topotactic oxidation occurred without any crystallographic damages.

Figures 5-2(c) – **2(h)** are the reciprocal space mappings (RSM) of (c) as-grown, (d) sample A, (e) sample B, (f) sample C, (g) sample D, and (h) sample F. The RSMs show that the $SrCoO_x$ films were heteroepitaxially grown on the GDC/YSZ with the epitaxial relationship of (001)[100] $SrCoO_{2.5}$ || (001)[110] GDC/YSZ. In **Figure 5-2(c)** and **Figure 5-2(d)**, only intense diffraction spot of $11\underline{1}2_{BM}$ is observed. On the other hand, only intense diffraction spot of 103_{PV} is observed in **Figure 5-2(h)**. In **Figures 5-2(f) – 2(g)**,

both diffraction spots are seen, clearly indicating that these films are the mixture composed of BM-$SrCoO_{2.5}$ and PV-$SrCoO_{3-\delta}$.

Since the as-grown sample was single phase $SrCoO_{2.5}$ while sample E was single phase $SrCoO_{3-\delta}$, the BM-$SrCoO_{2.5}$ into PV-$SrCoO_{3-\delta}$ conversion rate was calculated from the ratio of the diffraction peak area of 008 BM-$SrCoO_{2.5}$ and 002 PV-$SrCoO_{3-\delta}$ as a function of the transferred charge over required charge for complete transition (**Figure 5-4(a)**). With increasing charge transport, the peak area of 002_{PV} increases rapidly and saturates, whereas that of 008_{BM} decreases rapidly and approaches to zero. The conversion rate was calculated as (peak area of 002_{PV})/(peak area of 002_{PV} for sample E) as shown in **Figure 5-4(b)**. The conversion rate of as-grown was 0 %, sample A was 24.4 %, sample B was 34.5 %, sample C was 60.0 %, sample D was 84.7 %, and sample E was 100 %.

From the XRD and RSM results, several structural information including the lattice constants in both in-plane and out-of-plane directions and grain size were extracted. **Figure 5-5** summarizes the changes in (a) scattering vector in the in-plane direction ($q_x/2\pi$), (b) scattering vector in the out-of-plane direction ($q_z/2\pi$) ($11\underline{12}_{BM}$ or 103_{PV}), (c) *d*-spacing value, and (d) inverse of the integral width (008_{BM} or 002_{PV}). The inverse of the integration width is equal to the coherence length in the out-of-plane direction of the film (Scherrer's equation). The $q_x/2\pi$ (**Figure 5-5(a)**) and $q_z/2\pi$ (**Figure 5-5(b)**) values of as-grown and samples B − E were similar to the bulk values. However, the $q_x/2\pi$ of $11\underline{12}_{BM}$ for sample A (24.4 %) is small compared to the other samples. Although the out-

of-plane lattice parameter was similar to the bulk value, the in-plane lattice parameter of sample A is 0.4052 nm, which is ~3.8 % larger than that of bulk BM-$SrCoO_{2.5}$ (0.3905 nm). The out-of-plane lattice parameter of both BM-$SrCoO_{2.5}$ and PV-$SrCoO_{3-\delta}$ gradually decreased with increasing the conversion rate (**Figure 5-5(c)**).

Figure 5-5(d) shows the coherence length of 008_{BM} or 002_{PV} Bragg diffraction peak. If the electrochemical oxidation extends in the planar direction, a systematic change in the coherence length is expected. The values at 0 % (~19 nm) and 100 % (~17 nm) are smaller than the film thickness (~37 nm) calculated from the X-ray reflectivity measurements. This is probably due to the fact that the Bragg diffraction peak is affected by lattice distortion. The coherence length of 008_{BM} did not change until the conversion rate reached 40 %. The coherence length of 008_{BM} then gradually decreased with increasing conversion rate. On the other hand, the coherence length of 002_{PV} was ~4 nm at 24.4 %. Conversion but increased to above 10 nm with increasing conversion rate. It then finally reached 17 nm. Even if qualitative increase in the coherence length of 002_{PV} and decrease in that of 008_{BM} are reflecting progressive oxidation in $SrCoO_x$, since there is no systematic change, it does not reflect the grain size change upon planar oxidation. It should be noted that the lateral grain sizes of both BM-$SrCoO_{2.5}$ (14.5 ±0.4 nm) and PV-$SrCoO_3$ (10.4 ±1.3 nm) are obviously smaller than the film thickness (~37 nm). Although these results roughly suggest the columnar oxidation of $SrCoO_{2.5}$, they are not sufficient enough to fully confirm the nature of electrochemical oxidation in $SrCoO_x$.

In order to differently address the electrochemical oxidation of $SrCoO_x$, the electrical resistivity (ρ) was analyzed as shown in **Figure 5-6(a)** and **Figure 5-7**, and the S (**Figure 5-6(b))** of the $SrCoO_x$ was investigated as a function of the conversion rate. The as-grown sample showed insulating $\rho - T$ behavior, which is similar to that of $SrCoO_{2.5}$ reported by Lu *et al*.[16] With increasing the oxidation state, the $\rho - T$ approached to that of $SrCoO_{3-\delta}$. From these results, it can be confirmed that x in the $SrCoO_x$ films could be modulated from 2.5 to 3 by electrochemical oxidation. The as-grown sample (0 %) showed the ρ of 4.0 Ω cm and the S of +70 μV K^{-1}, whereas 100 % converted sample showed ρ = 0.7 mΩ cm and S = −0.5 μV K^{-1} at room temperature. Both ρ and S drastically decreased with increasing conversion rate. Note that the sheet resistance of GDC/YSZ substrate is extremely high (~10^{16} Ω, 0.5 mm) as compared to that of SrCoO2.5 (<10^7 Ω), and therefore, the $SrCoO_{2.5}$ film (~40 nm) solely contributes the observed S.

The ρ and S as a function of the conversion rate was predicted by assuming the conductive path is a parallel circuit composed of the insulating $SrCoO_{2.5}$ region and the conducting $SrCoO_{3-\delta}$ region as schematically shown in **Figure 5-6(c)**.

$$(\rho_{para})^{-1} = \frac{(\rho_{SrCoO2.5})^{-1} \cdot (100 - y) + (\rho_{SrCoO3})^{-1} \cdot y}{100}$$

and

$$S_{para} = \frac{S_{SrCoO2.5} \cdot (\rho_{SrCoO2.5})^{-1} \cdot \frac{100 - y}{100} + S_{SrCoO3} \cdot (\rho_{SrCoO3})^{-1} \cdot \frac{y}{100}}{(\rho_{SrCoO2.5})^{-1} \cdot \frac{100 - y}{100} + (\rho_{SrCoO3})^{-1} \cdot \frac{y}{100}} \quad 7,17$$

where *y* is the conversion rate. The results are plotted as dotted lines in **Figure 5-6(a)** and **Figure 5-6(b)**. Although the dotted lines reproduce both ρ and *S* well when the conversion rate is above 60 %, they do not reproduce the observed ρ and *S* when the conversion rate is less than 60 %. Hence, the system seems to be described by the isolated conducting $SrCoO_{3-\delta}$ column surrounded by the insulating $SrCoO_{2.5}$ matrix. Thus, the contribution from the series circuit of insulating $SrCoO_{2.5}$ region and conducting $SrCoO_{3-\delta}$ region along the current direction is not negligible.

Therefore, the ρ and *S* as a function of the conversion rate was calculated by assuming oxidation in the columnar direction as shown in **Figure 5-6(d)**. According to the percolation model [18], the observed ρ and *S* were reproduced very well as follows:

$$\rho_{percolation} = \rho_{SrCoO2.5} \cdot \left(1 - \frac{\phi}{\phi_c}\right) \qquad (\phi_c < 0.25)$$

$$\rho_{percolation} = \frac{1}{\rho_{SrCoO3-\delta}} \cdot (\phi - \phi_c) \qquad (\phi_c > 0.25)$$

$$S_{percolation} = S_{SrCoO2.5} \cdot \left(1 - \frac{\phi}{\phi_c}\right) \qquad (\phi_c < 0.25)$$

$$S_{percolation} = S_{SrCoO3-\delta} \cdot \left(\frac{\phi}{\phi_c}\right) \qquad (\phi_c > 0.25)$$

where ϕ is the conversion rate, and ϕ_c is the percolation threshold. These results suggest that columnar oxidation firstly occurs along with the oxidation direction and then spreads in perpendicular to the oxidation direction.

Figure 5-8 shows the macroscopic mapping of the insulating $SrCoO_{2.5}$ region and the conducting $SrCoO_{3-\delta}$ region in the partially oxidized $SrCoO_x$ films, obtained by the conductive AFM. Although their topographic AFM images (2 μm × 2 μm) did not show any noticeable differences, the electric current mappings clearly show differences (**Figure 5-8(e)** – **(h))**. Connection of the conducting region in (g) and (h) is clearly visible whereas that in (e) and (f) is not seen. Note that the lateral dimension of each highly conducting area stretches up to ~200 nm. As such, it is likely that the sample is fully oxidized along the depth direction, if the speed of oxidation is uniform. According to the percolation theory, the parallel electrical circuit model can be used for (g) and (h) of **Figure 5-8** with uniform and high current distribution on the plane. However, both the parallel and series circuit models contribute for images with dot-like current distribution from (e) and (f), which are below the percolation threshold. These observations are fully consistent with the resistivity and thermopower values.

These results are sufficient enough to claim successful visualization of the electrochemical oxidation of $SrCoO_{2.5}$ film into $SrCoO_{3-\delta}$ film. First, the columnar oxidation occurred along with the oxidation direction (perpendicular to the film surface) and then spread perpendicular to the oxidation direction (lateral direction).

5.4 Conclusion

In this chapter, the electrochemical oxidation reaction of $SrCoO_x$ was investigated. Thermopower analysis and conductive AFM analyses were performed to macroscopically visualize the electrochemical oxidation. The XRD results suggested that columnar oxidation occurred. The resistivity and thermopower data can be explained by the percolation of conducting $SrCoO_3$ columns. When the column density of $SrCoO_3$ exceeds 25 %, the resistivity and thermopower drastically decreased. The flowing current and the conducting area in the conductive AFM image increased with increasing oxidation state. All observations point out that columnar oxidation firstly occurred along with the oxidation direction and then spread perpendicular to the oxidation direction. This macroscopic image of the electrochemical oxidation would be of great use for developing a functional device utilizing the electrochemical redox reaction of $SrCoO_x$.

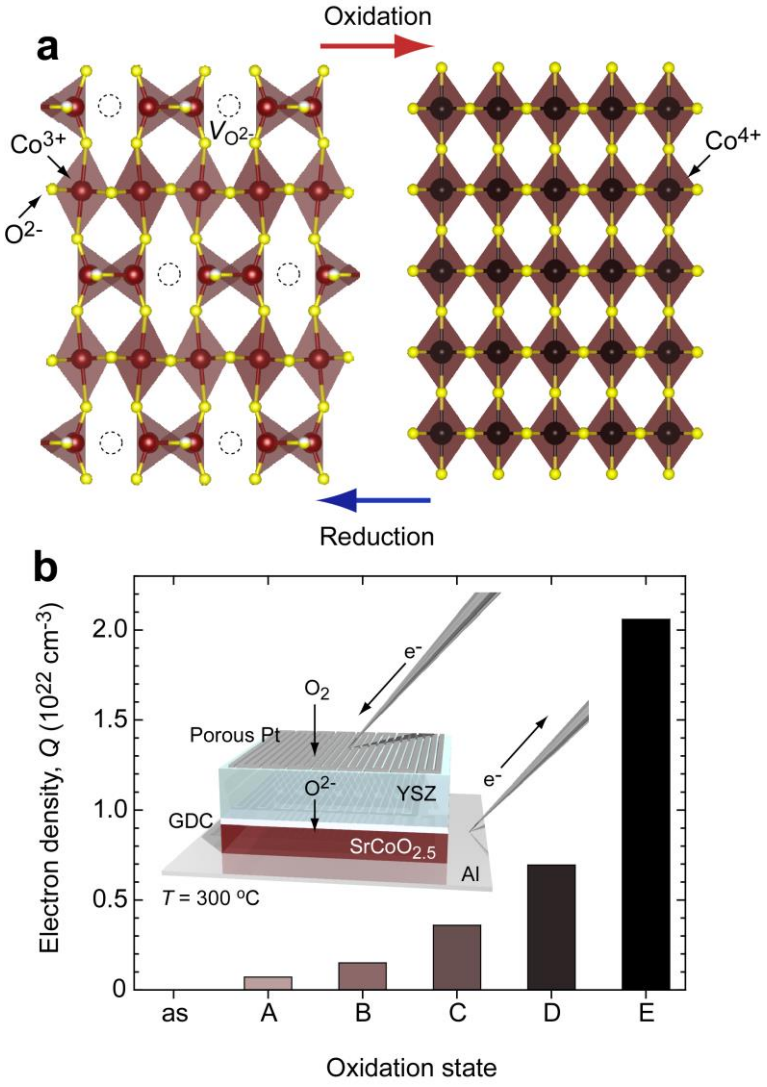

Figure 5-1. Electrochemical reaction of $SrCoO_x$ oxygen sponge. (a) Schematic crystal structure of brownmillerate $SrCoO_{2.5}$ and perovskite $SrCoO_{3-\delta}$. Although there are oxygen vacancies (V_{O2-}) in $SrCoO_{2.5}$ crystal, the vacancies are occupied with oxygen after the electrochemical oxidation ($SrCoO_{3-\delta}$). Valence states of cobalt ion change from 3+ into 4+ by the oxidation. This electrochemical reaction is reversible. (b) $SrCoO_x$ samples with different oxidation states. Oxidation current with different electron densities was applied to the multilayer structure composed of Pt/YSZ/GDC/$SrCoO_{2.5}$/Al at 300 °C in the air as shown in the inset.

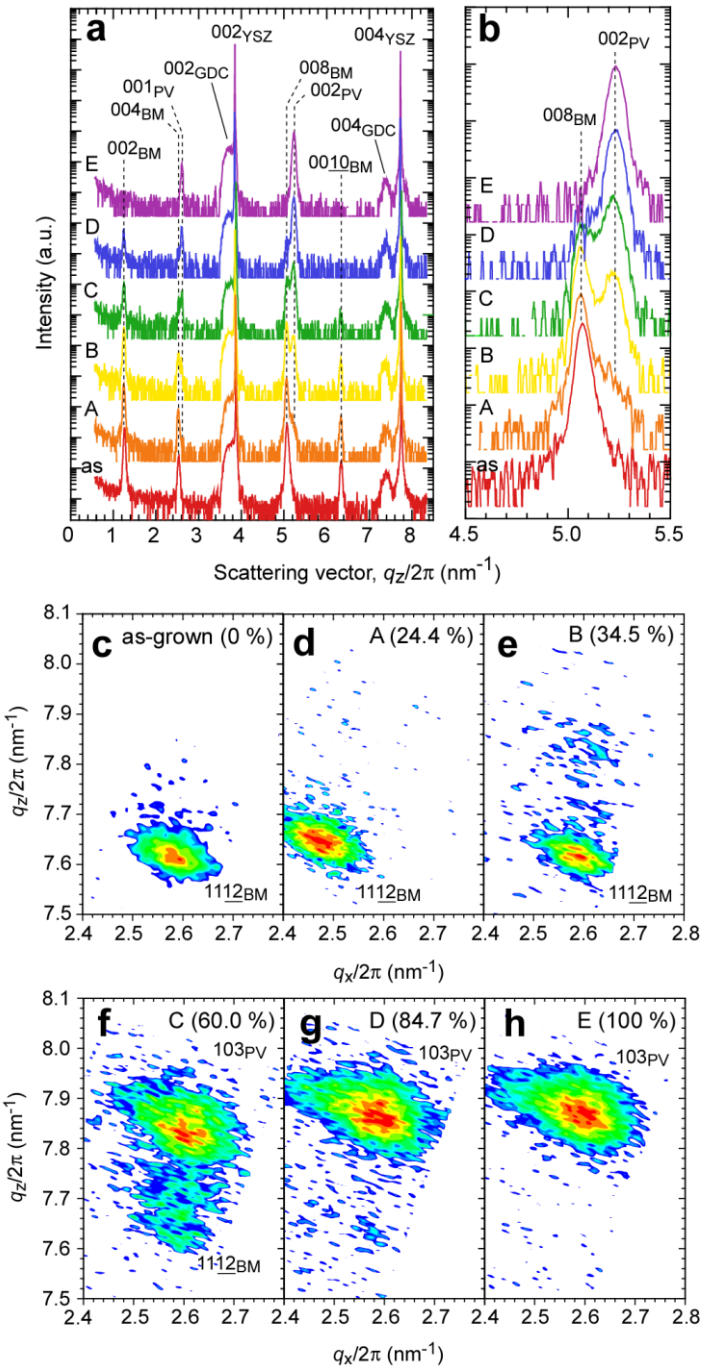

Figure 5-2. X-ray diffraction analyses of $SrCoO_x$ films with various oxidation states. (a) Out-of-plane XRD patterns. Intense diffraction peaks of $00l_{BM}$ or $00l_{PV}$ are seen together with $00l_{GDC}$/$00l_{YSZ}$, indicating strong *c*-axis orientation of the films. (b) Magnified XRD pattern. With increasing the oxidation state, the peak position changed from 008_{BM} to 002_{PV}. (c)−(h) RSMs around $11\underline{1}2_{BM}$ or 103_{PV}. Although the diffraction spot was $11\underline{1}2_{BM}$ when the oxidation state is lower than 34.5 %, it changed into 103_{PV} when the oxidation state was greater than 60 %.

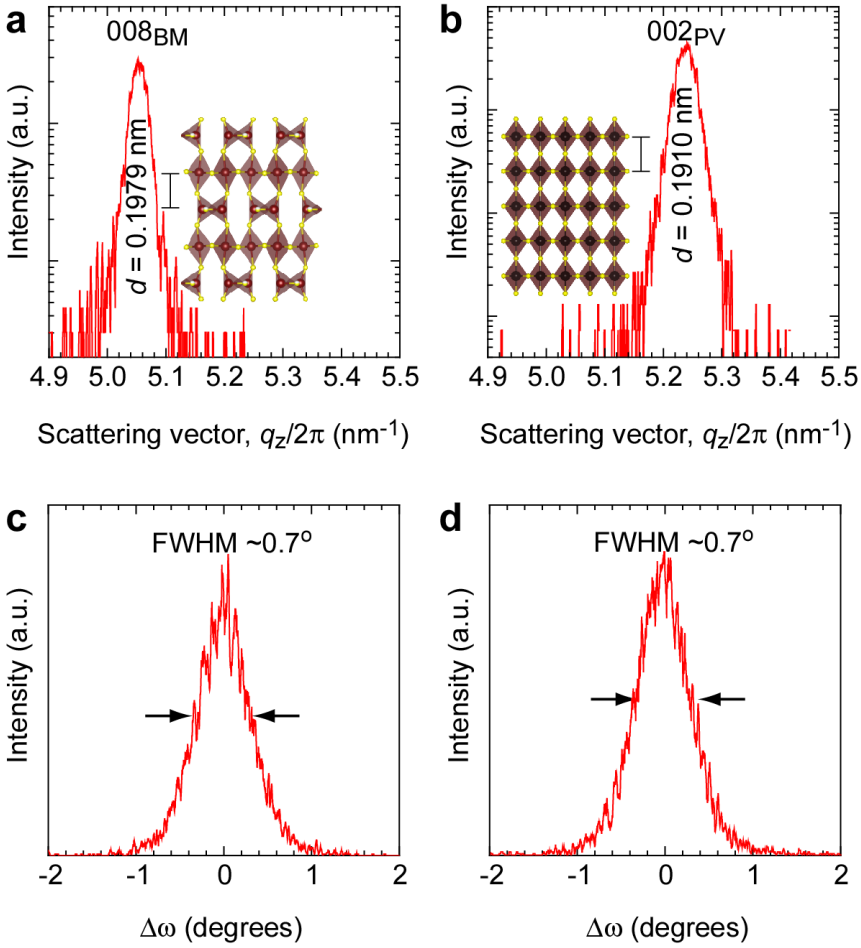

Figure 5-3. Out-of-plane lattice parameter and tilting of $SrCoO_x$ films at room temperature. Out-of-plane Bragg diffraction patterns of (a) as-grown (x = 2.5, 008_{BM}) and (b) electrochemically oxidized ($x = 3-\delta$, 002_{PV}) $SrCoO_x$ films. The d-spacing of 008_{BM} is 0.1979 nm, whereas that of 002_{PV} is 0.1910 nm, ~3.2 % shorter than 008_{BM}. Out-of-plane X-ray rocking curves of (c) 008_{BM} for the as-grown and (d) 002_{PV} for the electrochemically oxidized $SrCoO_x$ films. Average tilting (≡ full width at half maximum, FWHM) of both $SrCoO_x$ films is ~0.7 °.

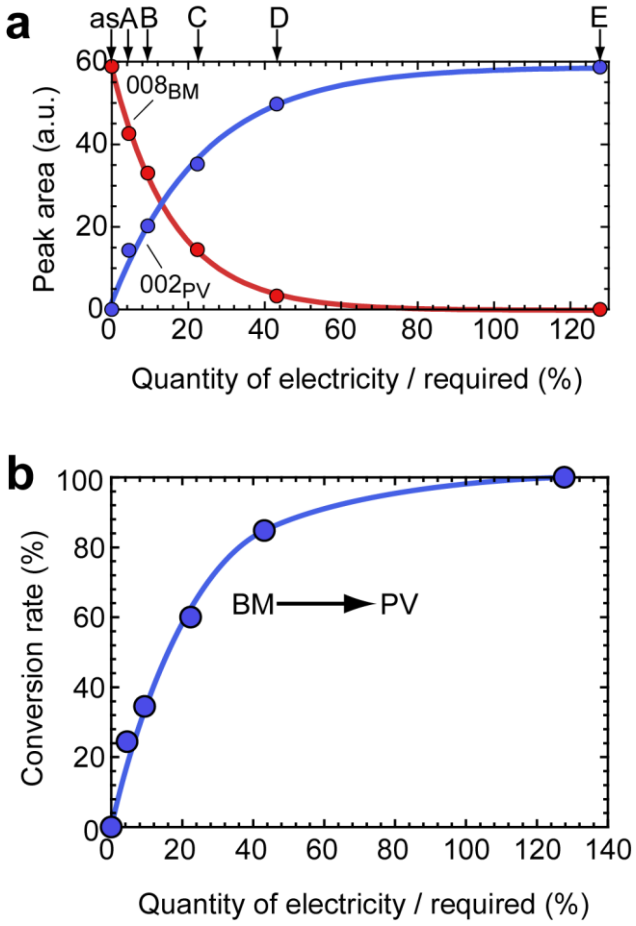

Figure 5-4. Calculation of the conversion rate from BM-$SrCoO_{2.5}$ into PV-$SrCoO_3$. (a) Changes in the diffraction peak area of (red) 008_{BM}-$SrCoO_{2.5}$ and (blue) 002_{PV}-$SrCoO_{3-\delta}$ as a function of the quantity of electricity over required electricity. The required electric charge is 9.6 mC. With increasing the electricity, the peak area of 002PV increases rapidly and saturates whereas that of 008BM decreases rapidly and approaches to zero. (b) Conversion rate from BM-$SrCoO_{2.5}$ into PV-$SrCoO_{3-\delta}$. S**ample E** was assumed to be fully oxidized. The conversion rate was calculated as (peak area of 002_{PV})/(peak area of 002_{PV} for **sample E**).

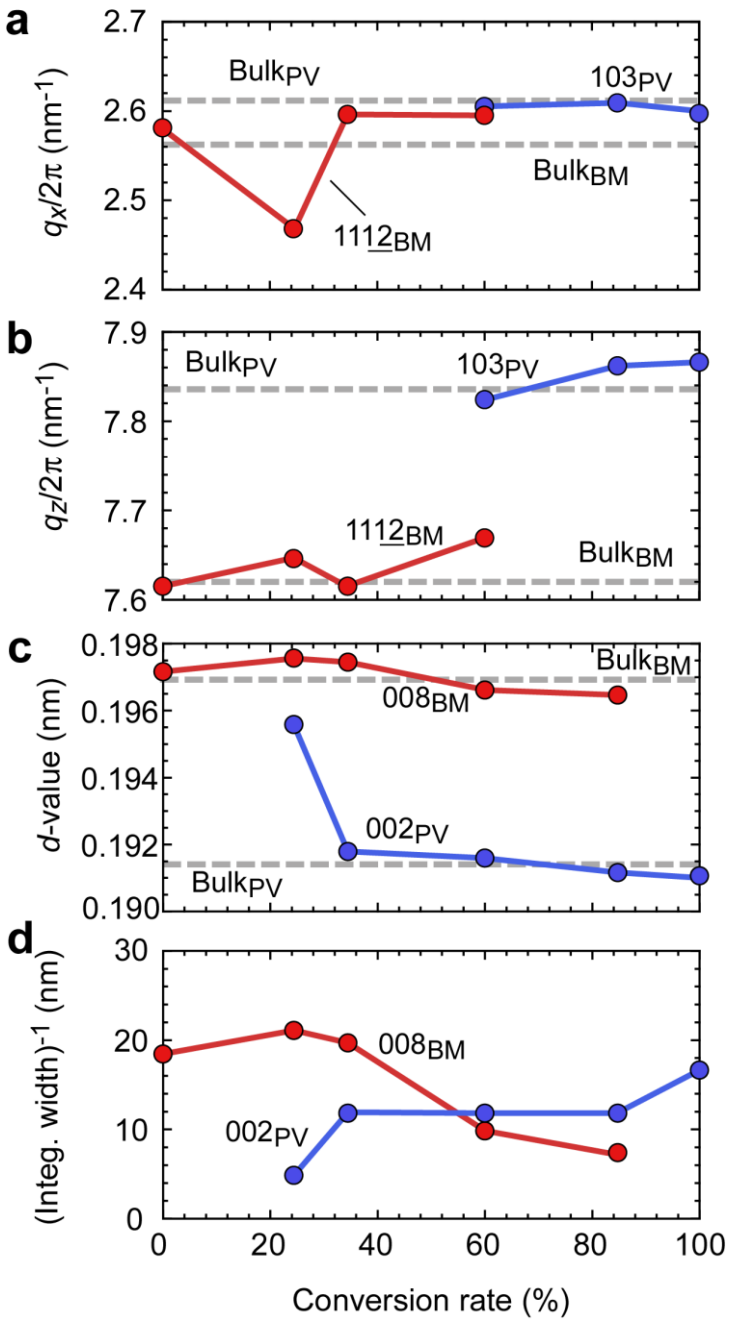

Figure 5-5. Changes in the crystallographic size of the $SrCoO_x$ film as a function of the conversion rate. (a) Scattering vector in the in-plane direction ($q_x/2\pi$) and (b) scattering vector in the out-of-plane direction ($q_z/2\pi$) of 11$\underline{2}$$_{BM}$ and 103$_{PV}$. (c) *d*-value and (d) inverse of the integral width of 008$_{BM}$ and 002$_{PV}$. Crystal phase changed from BM to PV around 40 − 60 %. The conversion rate dependences of the inverse of the integral width suggest that the columnar oxidation of $SrCoO_x$ occurred.

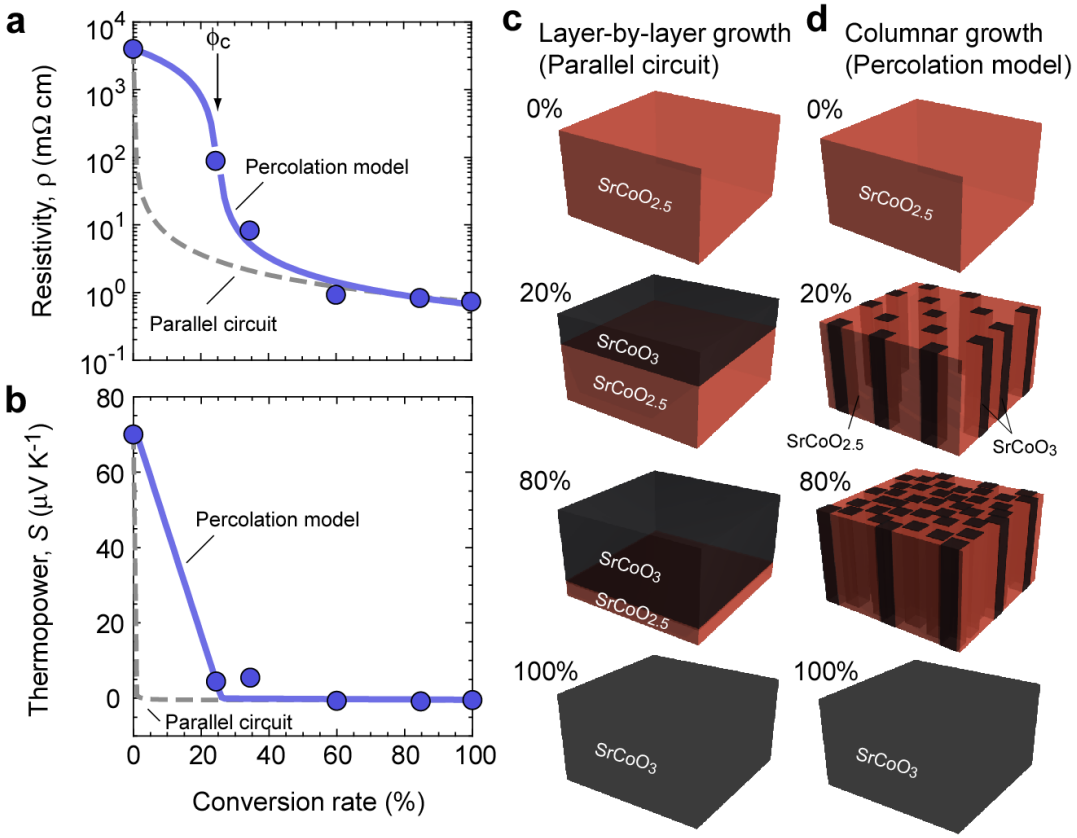

Figure 5-6. Electron transport properties of the $SrCoO_x$ as a function of the conversion rate at room temperature. (a) Resistivity and (b) thermopower. The as-grown sample (0 %) showed the resistivity of 4.0 Ω cm and the thermopower of +70 μV K^{-1}, whereas 100 % converted sample showed 0.7 mΩ cm and −0.5 μV K^{-1}. The dotted lines were calculated by assuming (c) the parallel electrical circuit of insulating $SrCoO_{2.5}$ region and conducting $SrCoO_{3-\delta}$ region. The solid lines were calculated by assuming (d) the percolation model (columnar growth) of conducting $SrCoO_{3-\delta}$ region. The percolation model reproduces the observed values well, indicating that columnar growth of $SrCoO_{3-\delta}$ occurred.

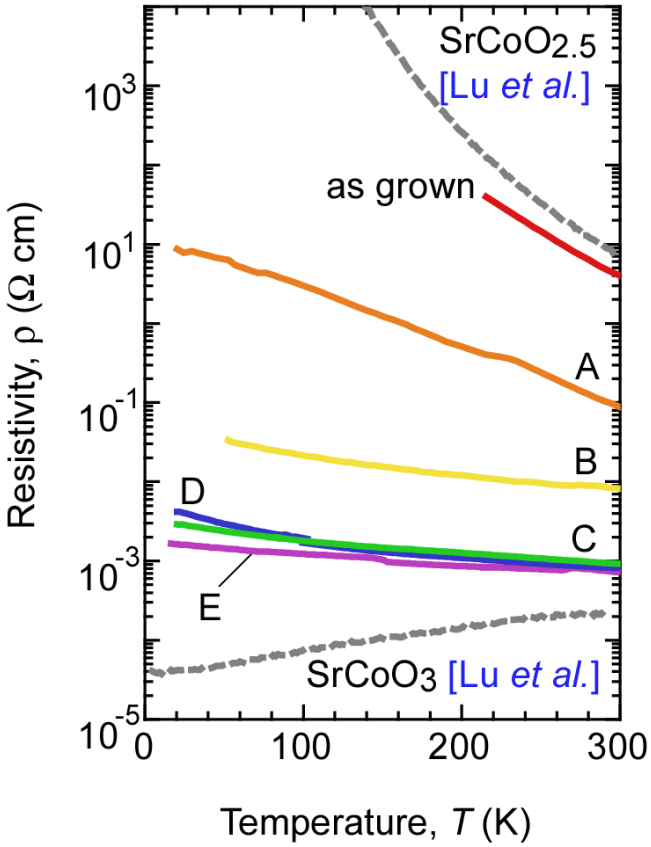

Figure 5-7. Temperature dependence of the resistivity of the $SrCoO_x$ films. The as-grown sample shows insulating $\rho-T$ behavior, which is similar to that of $SrCoO_{2.5}$ reported by Lu *et al*.[16] With increasing the oxidation state, the $\rho-T$ approaches that of $SrCoO_3$ reported by Lu *et al*.

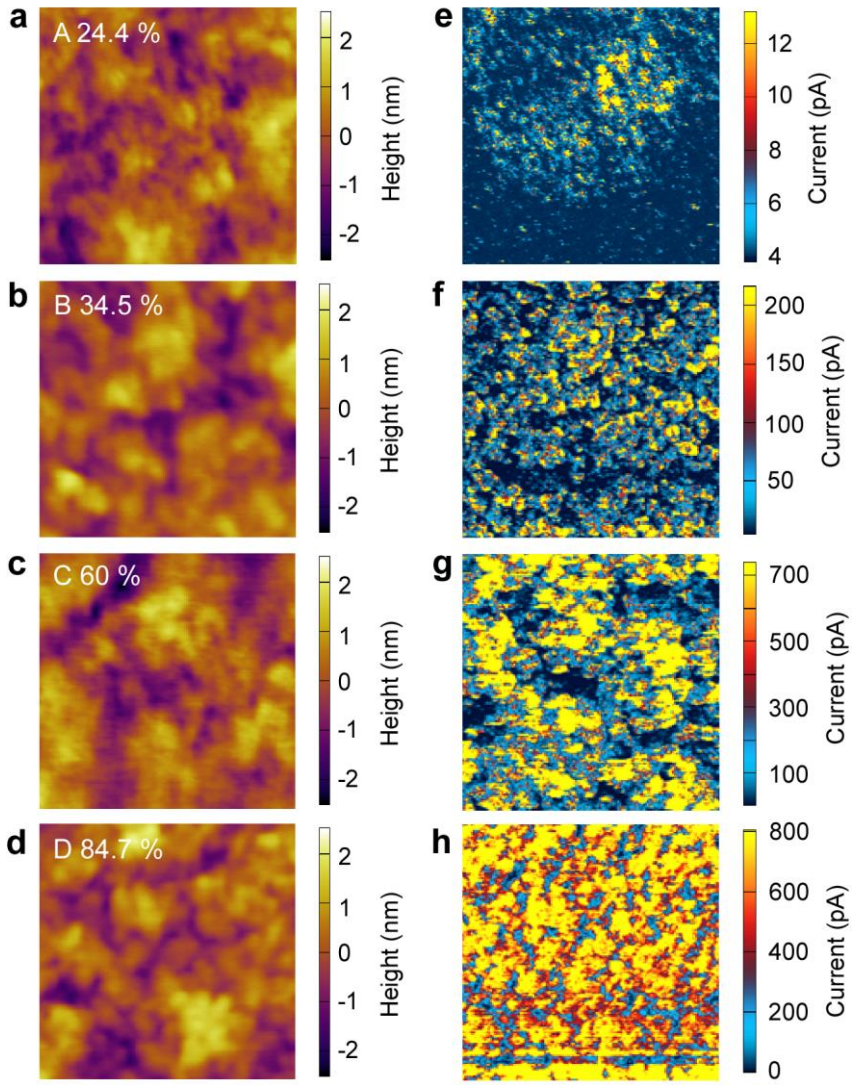

Figure 5-8. Macroscopic mapping of insulating $SrCoO_{2.5}$ region and conducting $SrCoO_{3-\delta}$ region. Topographic AFM images (2 μm × 2 μm) of (a) sample A (24.4 %), (b) sample B (34.5 %), (c) sample C (60 %) and (d) sample D (84.7 %). (e − h) Electric current mapping of the samples corresponding to the topographic AFM images of (a) – (d). The currents were taken under applying −2 V with respect to the sample surface. Connection of the conducting region in the images (g) and (h) is clearly visible whereas that in (e) and (f) is not seen. According to the percolation theory, parallel electrical circuit composed of insulating $SrCoO_{2.5}$ region and conducting $SrCoO_{3-\delta}$ region can be assumed for (g) and (h). However, both the parallel and series circuit composed of insulating $SrCoO_{2.5}$ region and conducting $SrCoO_{3-\delta}$ region contribute in the case of (e), which is below the percolation threshold (ϕ_c = 25 %).

References

1 Bezdicka, P. *et al*. Preparation and Characterization of Fully Stoichiometric $SrCoO_3$ by Electrochemical Oxidation. *Z Anorg Allg Chem* **619**, 7-12 (1993).

2 Tambunan, O. T. *et al*. Phase transformation of the brownmillerite $SrCoO_{2.5}$ thin film through alkaline water electrolysis. *J. Korean Phys. Soc.* **64**, 1845-1848 (2014).

3 Liu, X. H. *et al.* In Situ TEM Experiments of Electrochemical Lithiation and Delithiation of Individual Nanostructures. *Adv. Energy Mater.* **2**, 722-741 (2012).

4 Lu, X. *et al.* New Insight into the Atomic Structure of Electrochemically Delithiated O3-$Li_{(1-x)}CoO_2$ ($0 <= x <= 0.5$) Nanoparticles. *Nano Lett.* **12**, 6192-6197 (2012).

5 Pingree, L. S. C. *et al*. Electrical Scanning Probe Microscopy on Active Organic Electronic Devices. *Adv. Mater.* **21**, 19-28 (2009).

6 Ohta, H. *et al.* Field-induced water electrolysis switches an oxide semiconductor from an insulator to a metal. *Nature Commun.* **1**, 118 (2010).

7 Ohta, H. *et al.* Unusually large enhancement of thermopower in an electric field induced two-dimensional electron gas. *Adv. Mater.* **24**, 740-744 (2012).

8 Katase, T. *et al*. Thermopower analysis of the electronic structure around the metal-insulator transition in $V_{1-x}W_xO_2$. *Phys. Rev. B* **90**, 161105(R) (2014).

9 Katase, T. *et al*. Thermopower analysis of metal-insulator transition temperature modulations in vanadium dioxide thin films with lattice distortion. *Phys. Rev. B* **92**, 035302 (2015).

10 Sanchela, A. V. *et al*. Thermopower modulation clarification of the intrinsic effective mass in transparent oxide semiconductor $BaSnO_3$. *Phys. Rev. Mater.* **1**, 034603 (2017).

11 Sanchela, A. V. *et al*. Thermopower Modulation Clarification of the Operating Mechanism in Wide Bandgap $BaSnO_3$-$SrSnO_3$ Solid-Solution Based Thin Film Transistors. *Small* **15**, 1805394 (2019).

12 Jeen, H. *et al*. Orienting Oxygen Vacancies for Fast Catalytic Reaction. *Adv. Mater.* **25**, 6459-6463 (2013).

13 Lu, Q. Y. *et al*. Voltage-Controlled Topotactic Phase Transition in Thin-Film $SrCoO_x$ Monitored by In Situ X-ray Diffraction. *Nano Lett.* **16**, 1186-1193 (2016).

14 Lu, Q. Y. *et al*. Electronic Structure Evolution of $SrCoO_x$ during Electrochemically Driven Phase Transition Probed by in Situ X-ray Spectroscopy. *J. Phys. Chem. C* **120**, 24148-24157 (2016).

15 Long, Y. W. *et al*. Synthesis of cubic $SrCoO_3$ single crystal and its anisotropic magnetic and transport properties. *J. Phys. Condens. Matter.* **23**, 245601 (2011).

16 Lu, N. *et al.* Electric-field control of tri-state phase transformation with a selective dual-ion switch. *Nature* **546**, 124-128 (2017).

17 Ohta, H. *et al.* Giant thermoelectric Seebeck coefficient of two-dimensional electron gas in $SrTiO_3$. *Nature Mater.* **6**, 129-134 (2007).

18 Mclachlan, D. S. *et al*. Electrical-Resistivity of Composites. *J. Am. Ceram. Soc.* **73**, 2187-2203 (1990).

Chapter 6. Solid-State Electrochemical Redox Control of the Optoelectronic Properties for $SrFeO_x$ Thin Films

6.1 Objective of this Chapter

The previous chapter showed that the electrochemical redox using YSZ as the solid electrolyte can be a very effective way to tune the phase and physical properties in $SrCoO_x$ films. Therefore, it is interesting to apply this electrochemical redox method to other oxide systems with functional properties depending on oxygen stoichiometry to further examine the feasibility of YSZ as the solid electrolyte.

This chapter examines the solid-state electrochemical redox reaction of another type of TMOs, $SrFeO_x$. Since the electrical, magnetic, and optical properties of $SrFeO_x$ can be modulated by the oxygen contents, it is suitable as the active material of multifunctional memory devices. It also exhibits topotactic phase transition between brownmillerite (BM) and perovskite (PV).[1-3] However, past approaches are limited by the use of liquid electrolyte, which is not suitable for practical applications.[4,5]

This chapter extends the solid-state electrochemistry of $SrCoO_x$ in the previous chapter to $SrFeO_x$. $SrFeO_x$ epitaxial films on YSZ single crystal substrate were fabricated, and electrochemical redox reaction was performed. The resulting insulator ($SrFeO_{2.5}$) to metal ($SrFeO_{3-x}$) transition is thoroughly discussed.

6.2 Experimental

The films were fabricated by PLD technique. First, ~10-nm-thick GDC (10 mol% Gd-doped CeO_2) was heteroepitaxially grown on a YSZ substrate at 750 °C in an oxygen atmosphere (3 Pa). GDC was used as a buffer layer to prevent the chemical reaction during the electrochemical redox treatment at 300 °C. GDC is also a well-known oxide ion-conducting electrolyte. Focused KrF excimer laser pulses (λ = 248 nm, fluence ~ 1.2 J cm^{-2} $pulse^{-1}$, repetition rate = 10 Hz) were irradiated onto the ceramic target of GDC. Subsequently, ~45−64 nm thick $SrFeO_{2.5}$ film was heteroepitaxially grown on the GDC film at 750 °C in an oxygen atmosphere (1×10^{-3} Pa). The laser fluence was ~ 1.6 J cm^{-2} $pulse^{-1}$. After the bilayer film growth, the sample was cooled down to room temperature in the PLD chamber in an oxygen atmosphere (1×10^{-3} Pa).

The electrochemical oxidation of $SrFeO_{2.5}$/GDC/YSZ/Au multilayer structure sample was performed at 300 °C in air as shown in **Figure 6-1(a)**. First, an Au electrode was sputtered on the back surface of the YSZ substrate. Then, the film surface was mechanically pressed on an Au foil. The current was applied through the Au electrodes under a constant voltage of −5 V. The samples were labelled according to the applied electron density as A (0.15×10^{22} cm^{-3}), B (0.37×10^{22} cm^{-3}), C (0.54×10^{22} cm^{-3}), D (1.43×10^{22} cm^{-3}), E (2.04×10^{22} cm^{-3}), and F (3.99×10^{22} cm^{-3}) (**Figure 6-1(b)**).The applied electron density (Q) was calculated as $Q = (\int I \cdot t)/(V \cdot e)$, where I is the current at time t, V is the volume of the $SrFeO_x$ film, and e is the electron charge. The ideal Q for

converting $SrFeO_{2.5}$ into $SrFeO_3$ is 1.65×10^{22} cm^{-3}. After applying the current, the sample was immediately cooled down to room temperature. After the oxidation treatment, the bulk density and the thickness were measured by the X-ray reflectivity.

6.3 Results and discussion

The bulk density of the as-grown $SrFeO_x$ film was ~5.0 g cm^{-3}, which is slightly larger than that of $SrFeO_{2.5}$ (~4.8 g cm^{-3}), and it gradually increased with Q (**Figure 6-1(b)**). The bulk density of sample F (3.99×10^{22} cm^{-3}) was ~5.5 g cm^{-3}, which is close to that of $SrFeO_3$. Then, the crystalline phase of the resultant $SrFeO_x$ films is analyzed as follows. Only intense diffraction peaks of 00*l* BM-$SrFeO_{2.5}$ are seen in the out-of-plane XRD pattern of the as-grown film (**Figure 6-2(a)**) together with 00*l* GDC / 00*l* YSZ, indicating strong *c*-axis orientation of the BM-$SrFeO_{2.5}$. Upon reaching $Q > 1.43 \times 10^{22}$ cm^{-3}, the diffraction peak of 002 BM disappeared, indicating a phase transition. The diffraction peak around $q_z/2\pi = 5$ nm^{-1} shifted to the right (higher $q_z/2\pi$) with increasing Q. In order to clarify the origin of this peak shift, the diffraction peaks were deconvoluted using Gaussian functions (**Figure 6-3**). With increasing Q, the phase changed step-by-step from $SrFeO_{2.5}$ to $SrFeO_{2.5+x}$ and PV $SrFeO_{3-x}$.

To confirm the crystalline phases, the interplanar distances (*d*-values) were extracted from the magnified XRD patterns (**Figure 6-3**). The *d*-value changed step-by-step from 0.205 nm to 0.198 nm, 0.1955 nm, and 0.194 nm, which were similar to those of $SrFeO_{2.5}$,

$SrFeO_{2.75}$, $SrFeO_{2.875}$, and $SrFeO_3$, respectively. Further, the peak area ratio was analyzed (**Figure 6-2(c)**). According to the peak analysis, the as-grown $SrFeO_{2.5}$ developed into $SrFeO_{2.5+x}$ phase with increasing Q. In the images obtained from atomic force microscopy (AFM) (**Figure 6-3**), several ten-nanometer-sized grain structure was observed in all cases. If $Q > 1.43 \times 10^{22}$ cm^{-3}, square-shaped morphologies were observed, most likely due to the bulk density change. The root mean square roughness was ~0.2 nm, which almost did not change after the oxidation treatment.

Figure 6-5 summarizes the optical transmission spectra of the films. The as-grown film was yellowish-transparent, and the optical transmission at 2 eV was ~70% due to the high optical reflection of YSZ substrate (~25 %). The optical bandgap of the as-grown film is ~2 eV, consistent with the reported value.[6,7] A slight change in the curvature around 2.7 eV is observed, indicating a charge transfer absorption from O 2p to Fe 3d of BM-$SrFeO_{2.5}$.[8,9] With increasing Q, the color changed into dark-brown, and the overall optical transmission gradually reduced. At $Q = 3.99 \times 10^{22}$ cm^{-3}, the optical transmission at 2 eV decreased to ~30%. Two absorptions, located ~1.5 eV and ~2.5 eV, are observed in oxidized $SrFeO_x$, which have been assigned as γ (charge transfer from O 2p to Fe 3d octahedral t_{2g}) and δ (charge transfer from O 2p to Fe 3d octahedral e_g) of perovskite $SrFeO_3$, respectively.[8,9] A similar change in the oxidation state of Co from +3 to +4 has been observed in the $SrCoO_x$ films deposited under varying oxygen pressures.[10] These results clearly indicate that the oxidation state of Fe increased from +3 to +4 with

increasing Q. It is important to emphasize that these change in the optical transmission is reversible; the transmission at 550 nm in wavelength changed from 65% (reduced) to 6% (oxidized) repeatedly (**Figure 6-6**).

Finally, the electrical properties of the films are shown in **Figure 6-7**. The electrical resistivity of the as-grown sample was too high to be measured. After the oxidation treatment, the resistivity decreased drastically from ~10^1 Ω cm to ~10^{-2} Ω cm at room temperature. The thermopower of the samples A, B, and C ($Q < 0.54 \times 10^{22}$ cm^{-3}) was positive (150−200 μV K^{-1}) while that of the samples D, E, and F was negative (−10 μV K^{-1}), indicating a shape change and E_F shift in valence band.[7,9] These results clearly confirm that an insulator to metal transition occurred, which is further confirmed by the temperature dependence of the electrical conductivity (**Figure 6-8**) and the activation energy (E_a) around room temperature. The E_a of the electrical conductivity was ~0.2 eV for samples A, B, and C, which is similar to the reported values from $SrFeO_{2.5+x}$ thin films.[11] The E_a for samples A, B, and C is smaller than the bandgap (~2 eV) of $SrFeO_{2.5+x}$ films, indicating that the Fermi energy is located slightly above the valence band maximum. The E_a significantly decreased upon further oxidation and approached zero, confirming the insulator to metal transition.

6.4 Conclusion

In summary, the solid-state electrochemical redox control of the optoelectronic properties

in $SrFeO_x$ was demonstrated using YSZ substrate as the solid electrolyte. With increasing the degree of oxidation, the phase gradually transfered from $SrFeO_{2.5}$ to $SrFeO_{2.5+x}$, and $SrFeO_{3-x}$. The color of the film changed from yellowish-transparent to dark brown. Although as-grown $SrFeO_{2.5}$ film showed high resistivity ($\rho > 10^1$ Ω cm), the ρ greatly decreased ($\sim 10^{-2}$ Ω cm) with increasing the applied charge density. Simultaneously, the thermopower decreased significantly from ~+200 μV K^{-1} to ~−10 μV K^{-1}. The optical and electrical properties of $SrFeO_x$ were modulated successfully by all-solid-state electrochemical oxidation reaction. The present results clearly show that $SrFeO_x$ has potential as the active material of solid-state multifunctional memory devices.

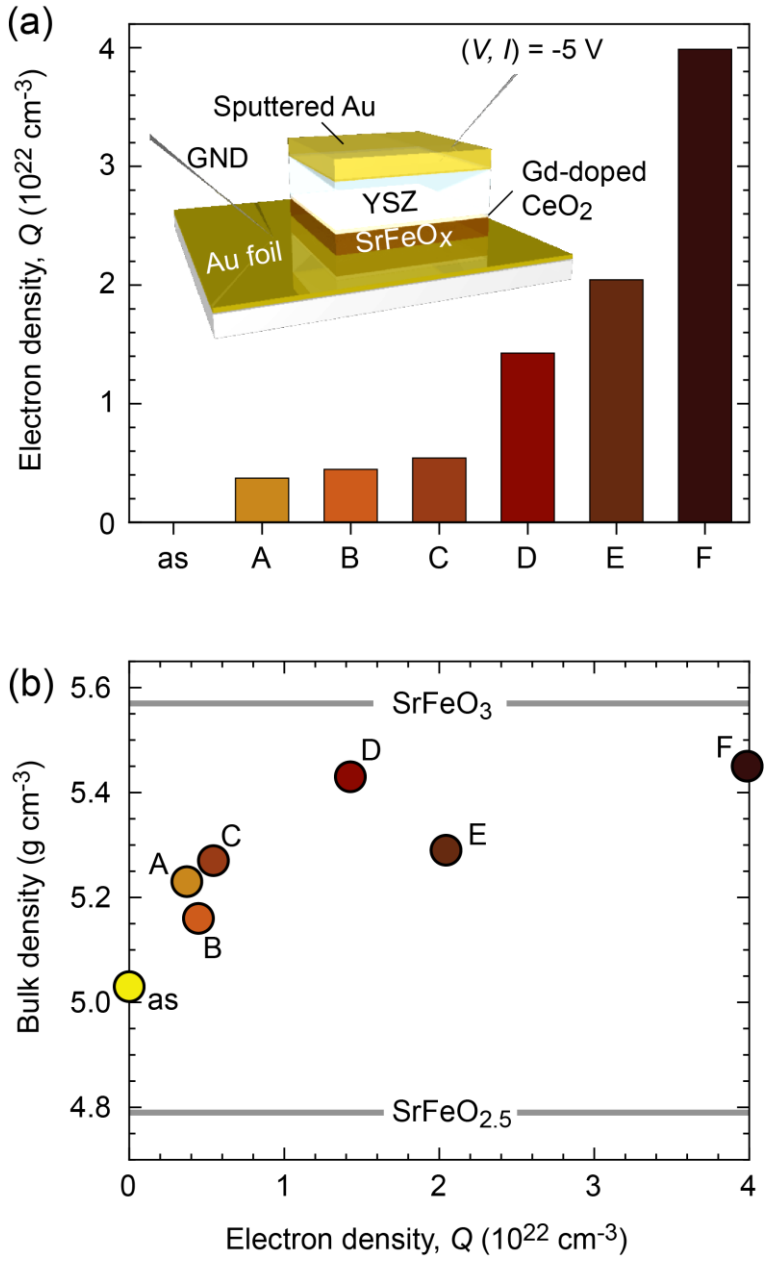

Figure 6-1. Electrochemical oxidation of $SrFeO_x$ films. (a) $SrFeO_x$ film samples oxidized by applying varied electron densities. The inset shows the schematic experimental setup of the electrochemical oxidation. (b) Bulk density of the $SrFeO_x$ films vs. electron density (Q). The bulk density gradually increases with Q.

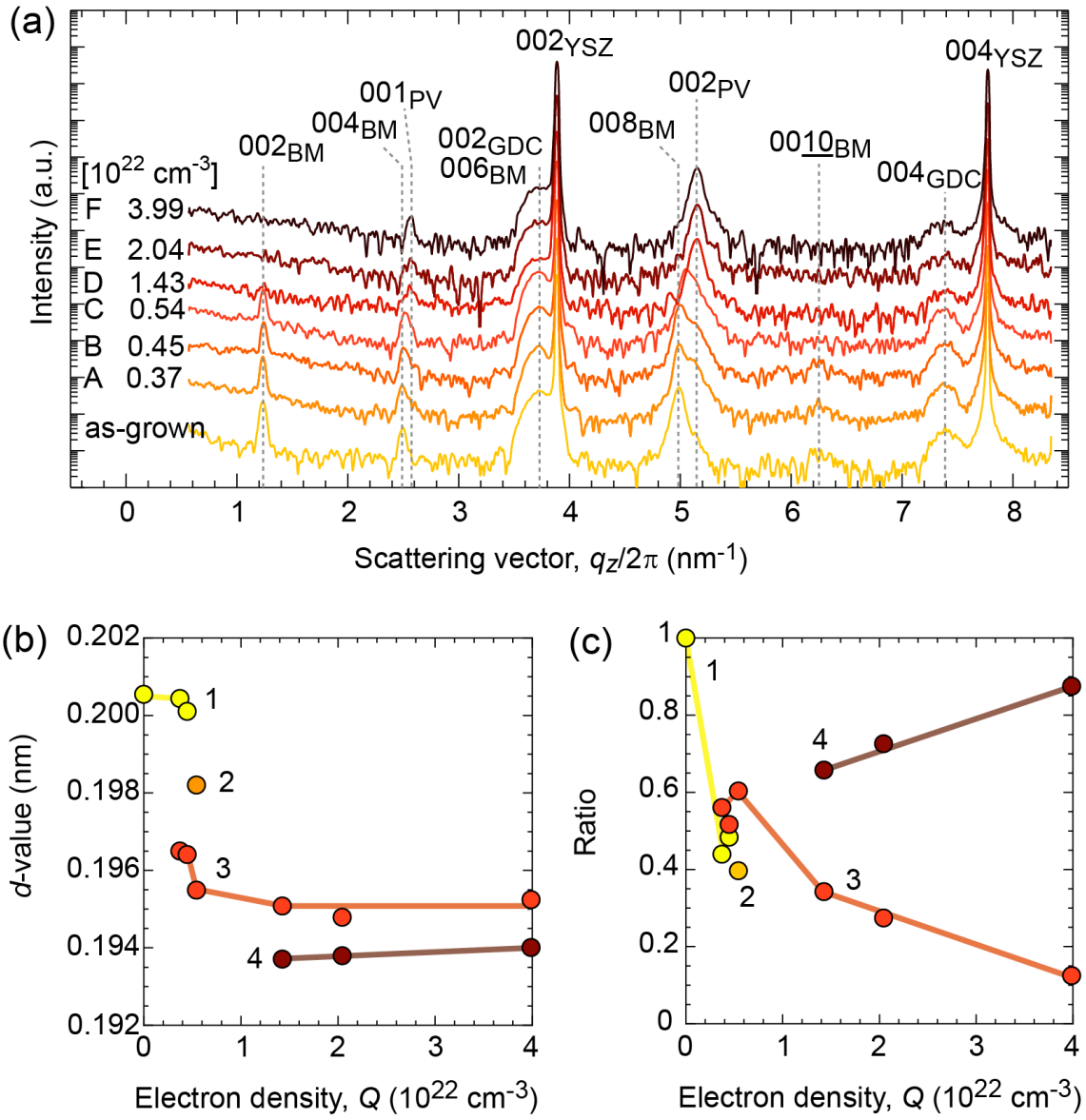

Figure 6-2. Crystalline phases of the resultant $SrFeO_x$ films. (a) Out-of-plane XRD patterns. BM: Brownmillerite, PV: perovskite. With increasing the electron density Q, the BM phase changes into the PV phase. (b) Changes in the *d*-value of 008_{BM} or 002_{PV} as a function of *Q*. 1: $SrFeO_{2.5}$, 2 and 3: $SrFeO_{2.5+x}$, and 4: $SrFeO_{3-x}$. (c) Change in the volume ratio of the phases as a function of *Q*.

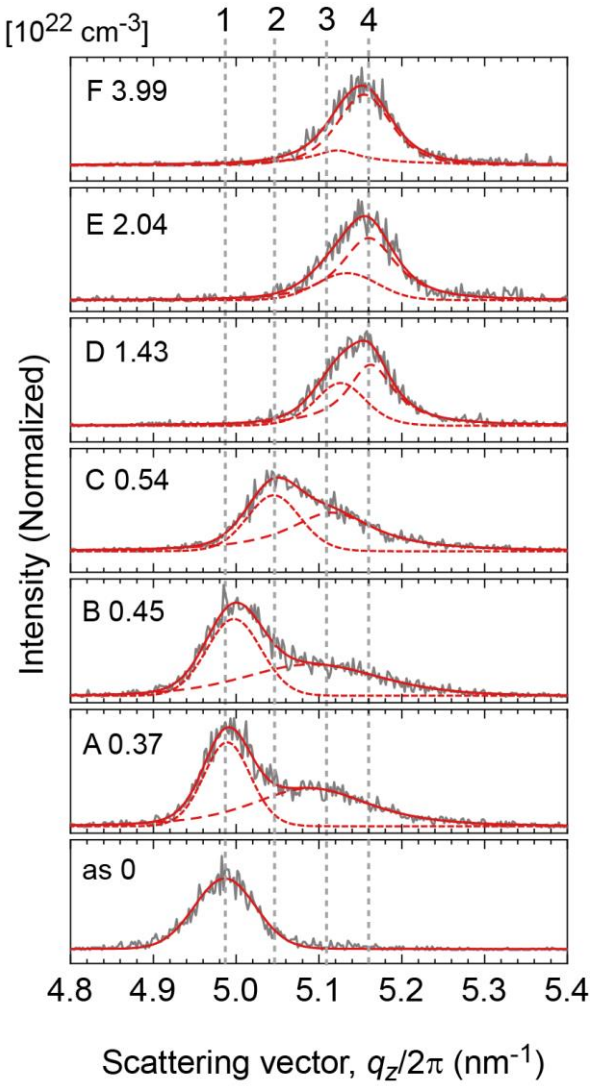

Figure 6-3. Magnified out-of-plane XRD patterns of the resultant $SrFeO_x$ films. The diffraction peaks were deconvoluted using Gaussian functions. 1: $SrFeO_{2.5}$, 2 and 3: $SrFeO_{2.5+x}$, and 4: $SrFeO_{3-x}$.

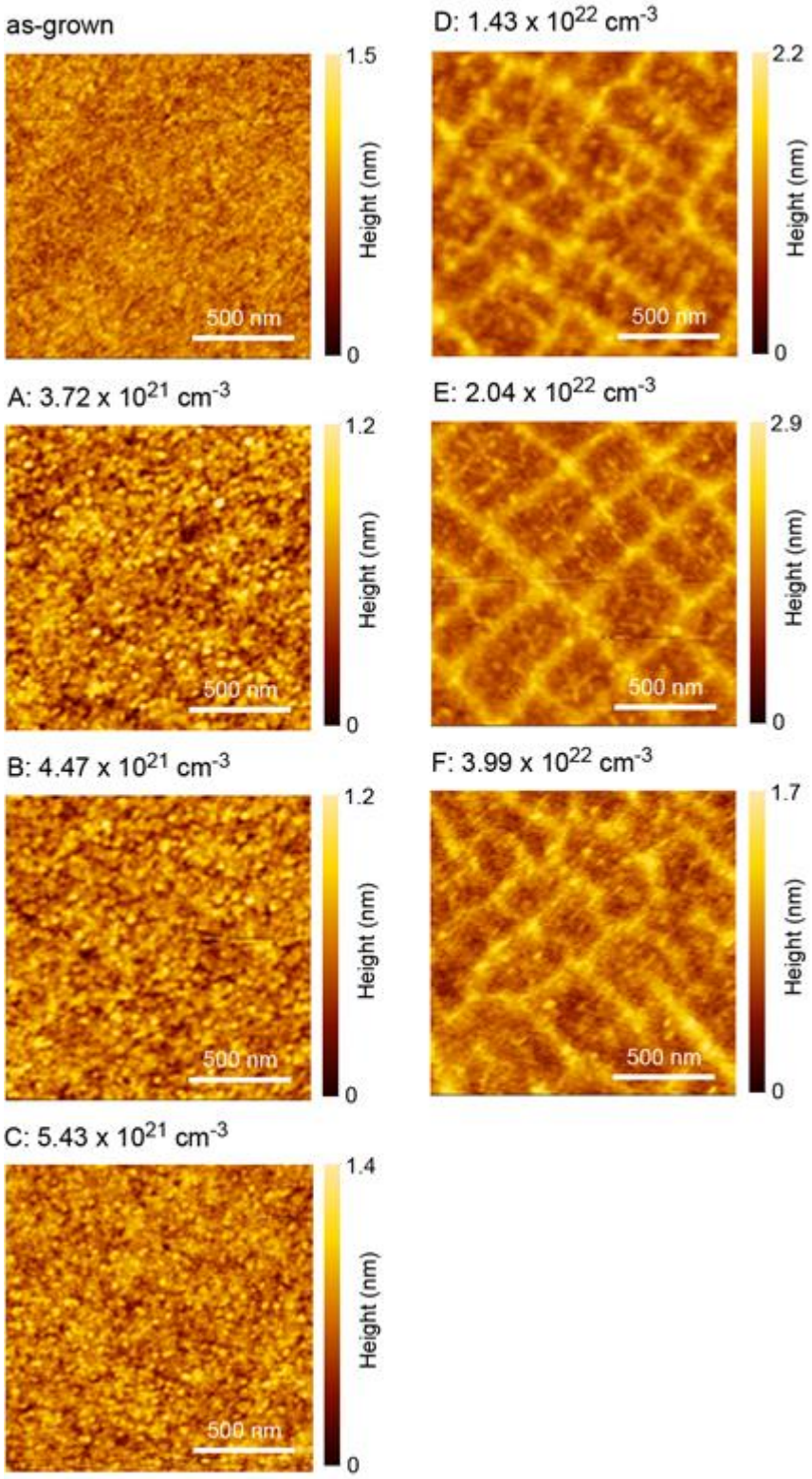

Figure 6-4. Topographic AFM images of the $SrFeO_x$ films.

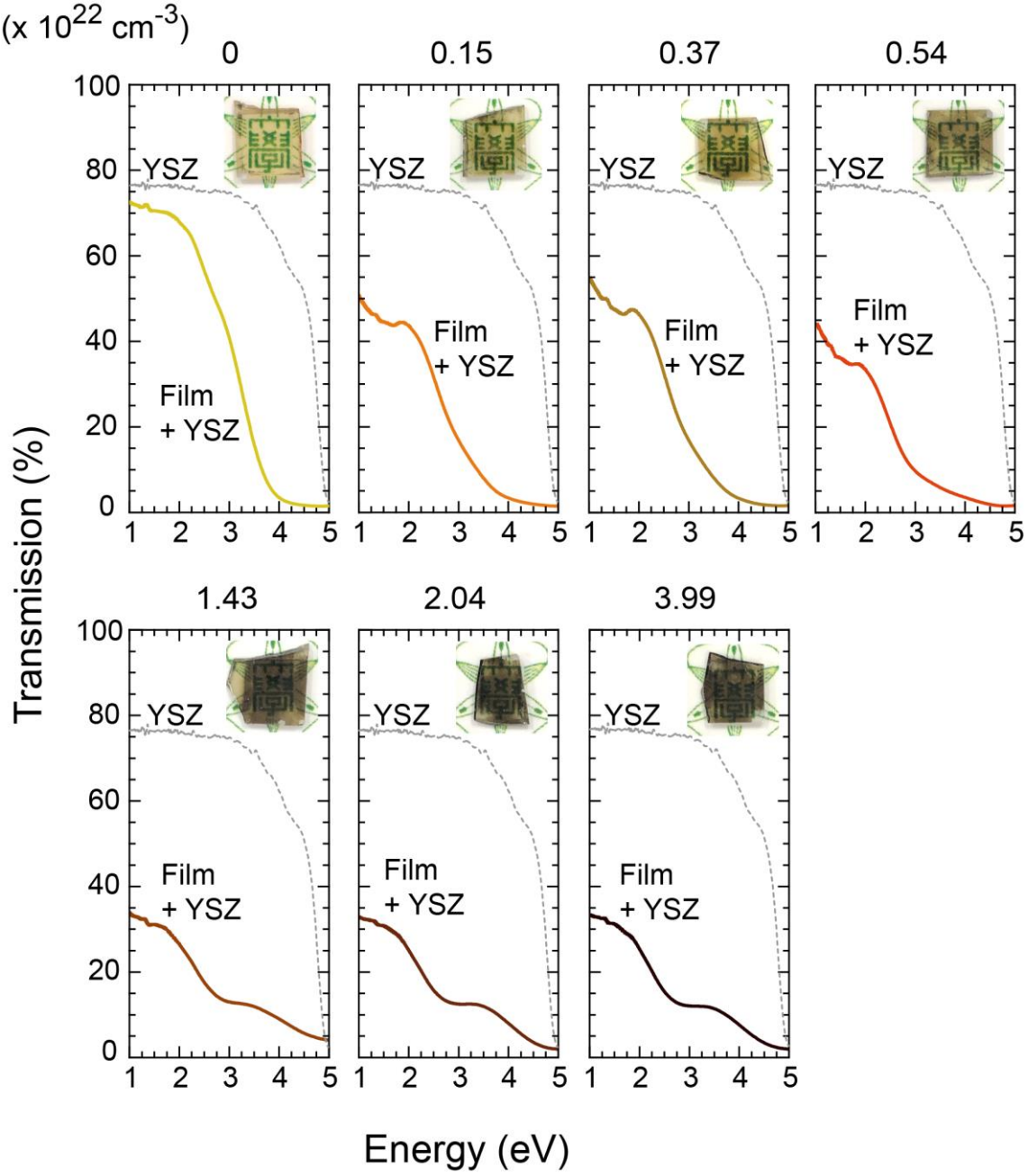

Figure 6-5. Optical transmission spectra of the resultant $SrFeO_x$ films on YSZ substrate. Transmission spectrum of YSZ substrate is also plotted for comparison.

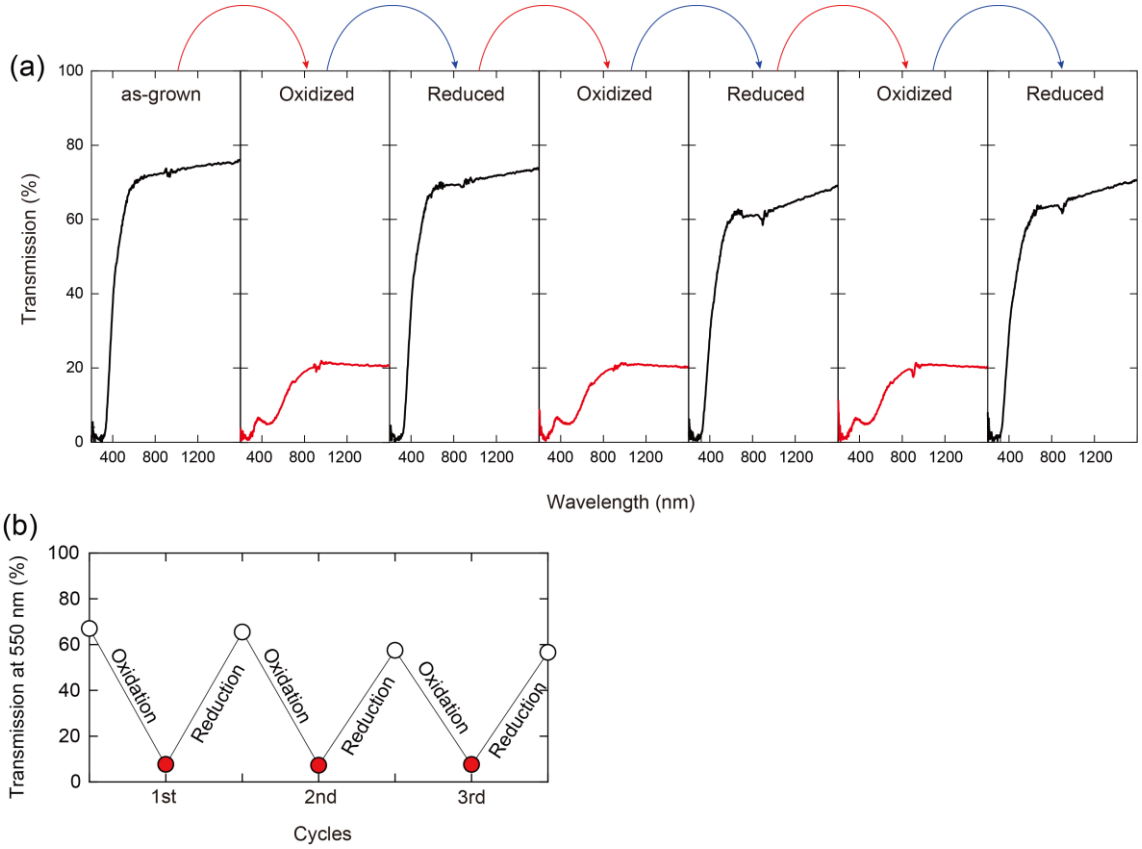

Figure 6-6. (a) Change in the optical transmission spectra of the SrFeO*x* films after the oxidation/reduction cyclic treatment. (b) Change in the optical transmission at 550 nm in wavelength.

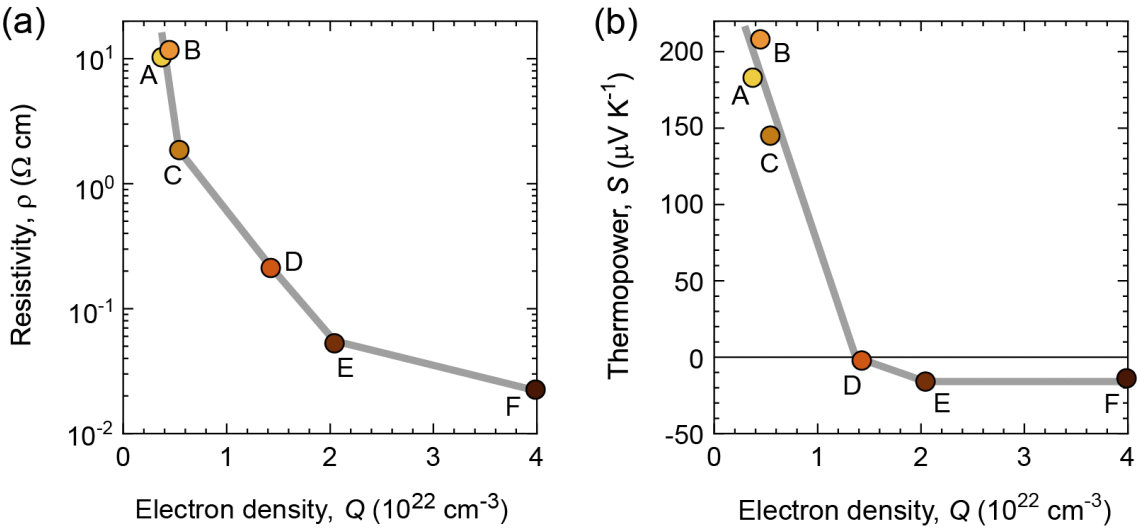

Figure 6-7. Electrical properties of the resultant $SrFeO_x$ films. (a) Resistivity, (b) Thermopower. Although as-grown $SrFeO_{2.5}$ film showed high resistivity ($\rho > 10^1$ Ω cm), the ρ greatly decreased ($\sim 10^{-2}$ Ω cm) with increasing the applied charge density. Simultaneously, the thermopower decreased significantly from ~+200 μV K^{-1} to ~−10 μV K^{-1}.

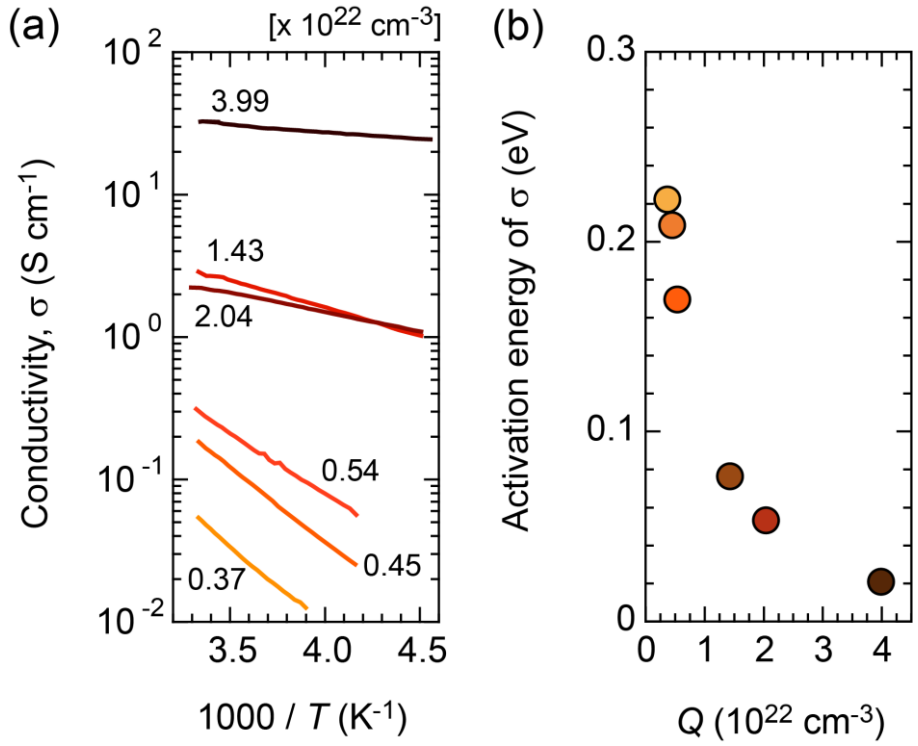

Figure 6-8. (a) Temperature dependence of the electrical conductivity of the $SrFeO_x$ films. (b) Activation energy of the electrical conductivity of the $SrFeO_x$ films around room temperature.

References

1 Maity, A. *et al.* Solid-state reactivity explored in situ by synchrotron radiation on single crystals: from $SrFeO_{2.5}$ to $SrFeO_3$ via electrochemical oxygen intercalation. *J. Phys. D* **48**, 504004 (2015).

2 Nallagatla, V. R. *et al.* Complementary Resistive Switching and Synaptic-Like Memory Behavior in an Epitaxial $SrFeO_{2.5}$ Thin Film through Oriented Oxygen-Vacancy Channels. *ACS Appl. Mater. Interfaces* **12**, 41740-41748 (2020).

3 Nallagatla, V. R. *et al*. Resistive switching behavior in epitaxial brownmillerite $SrFeO_{2.5}$/Nb:$SrTiO_3$ heterojunction. *Appl. Phys. Lett.* **117**, 143503 (2020).

4 Ge, C. *et al.* A ferrite synaptic transistor with topotactic transformation. *Adv. Mater.* **31**, 1900379 (2019).

5 Saleem, M. S. *et al.* Electric field control of phase transition and tunable resistive switching in $SrFeO_{2.5}$. *ACS Appl. Mater. Interfaces* **11**, 6581-6588 (2019).

6 Galakhov, V. *et al.* Vanlence band structure and X-ray spectra of oxygen-deficient ferrites $SrFeO_x$. *J. Phys. Chem. C.* **114**, 5154-5159 (2010).

7 Nallagatla, V. R. *et al.* Topotactic phase transition driving memristive behavior. *Adv. Mater.* **31**, 1903391 (2019).

8 Khare, A. *et al.* Topotactic metal–insulator transition in epitaxial $SrFeO_x$ thin films. *Adv. Mater.* **29**, 1606566 (2017).

9 Wang, L. *et al*. Brownmillerite phase formation and evolution in epitaxial strontium ferrite heterostructures. *Appl. Phys. Lett.* **114**, 231602 (2019).

10 Choi, W. S. *et al.* Reversal of the lattice structure in $SrCoO_x$ epitaxial thin films studied by real-time optical spectroscopy and first-principles calculations. *Phys. Rev. Lett.* **111**, 097401 (2013).

11 Tunney, J. J. *et al*. The electrical conductance of $SrFeO_{2.5+x}$ thin films. *J. Electroceram.* **5**, 63-69 (2000).

Chapter 7. Summary and Future Prospects

This given doctoral research investigated the fundamental functional properties of $SrCoO_x$ and $SrFeO_x$ films and examined the feasibility of utilizing them in all-solid-state device applications. The electronic structure of the films was electrochemically modulated and monitored with X-ray spectroscopy as well as thermopower measurement.

Firstly, in order to study the electronic structure and location of E_F of $SrCoO_x$, the thermopower method was utilized in Chapter 3. The lattice mismatch and surface morphology effects on the E_F were reflected by changes in thermopower values. Although the differences of the electronic structure and the oxidation states among the samples were extremely small, the thermopower significantly changed from +330 μV K^{-1} to −185 μV K^{-1} with a slight increase of lattice and/or absorbed oxygen in the $SrCoO_{2.5}$ films, clearly demonstrating the effectiveness of thermopower to analyze the electronic structure and the oxidation states of TMOs. Chapter 4 addressed the protonation of $SrCoO_{2.5}$ using CAN as the solid electrolyte. With increasing the H^+ concentration, the phases were modulated form $SrCoO_{2.5}$ to $HSrCoO_{2.5}$, $H_{1.5}SrCoO_{2.5}$, and $H_2SrCoO_{2.5}$. In addition, the metal-to-insulator, transparent-to-opaque, and antiferromagnetic-to-ferromagnetic transitions also occurred. This approach solves the liquid leakage problem by using ionic liquid as the electrolyte. Chapter 5 discusses the electrochemical redox of controlling oxygen non-stoichiometry. The topotactic BM → PV phase transition induced by

electrochemical redox reaction utilizing YSZ as the solid electrolyte was visualized macroscopically using conductive AFM, which helps the comprehension of the oxidation direction. Simultaneously, the steep decrease of both resistivity and the absolute thermopower value indicated that the columnar oxidation occurred instead of layer-by-layer oxidation. This electrochemical redox control of phase evolution was extended in another type of metal-insulator transition in $SrFeO_x$ system. Similar electrochemical modulation of oxygen concentration and electrochemically induced phase transition were discussed in Chapter 6. The optoelectronic properties of $SrFeO_x$ thin films were tuned reversibly by the solid-state electrochemical method used to control $SrCoO_x$. Both $SrCoO_x$ and $SrFeO_x$ exhibited the phase transition accompanied by changes in physical properties through electrochemical redox using YSZ as the solid electrolyte.

This research utilized the versatility of transition metal oxides in non-volatile memory application with an emphasis on achieving reversibility in all-solid-states. The results indeed demonstrated successful solid-state modulation of electrical, optical, and magnetic properties of $SrCoO_x$/$SrFeO_x$ films with the use of CAN/YSZ as the solid electrolyte. Based on the results archived in this research, solid electrochemical devices utilizing transition metal oxides as an active layer can be implemented in memory applications. Electrochemical protonation has been proven to be an effective method for altering the physical properties such as electrical, optical, and magnetic properties of TMOs. Therefore, combing these physical properties transition would be valuable for advanced

application. However, one of the key requirements for practical application is the switching speed of electrochemical protonation, and further work needs to be done in this respect. Moreover, the tuning of oxygen concentration may vary properties other than the electrical, optical, and magnetic properties. Very recently, tunable thermal conductivity has been realized by electrochemically inserting H^+ and O^{2-} ions into the $SrCoO_{2.5}$ lattice structure. However, the use of ionic liquid and ion gels as the electrolyte faced the leakage problem of liquid and poor mechanical stability.[1] This research has solved this problem using CAN/YSZ as the solid electrolyte, which would be useful for electrochemical modulation of thermal conductivity. It provides a possibility to fabricate the thermal transistor utilizing transition metal oxides as the active layer.

The contributions from this research push the limitations in current approaches in designing TMO memory devices and establish a pioneering footstep towards developing advanced memory devices suitable for satisfying the demands for the upcoming era of information.

References

1 Lu, Q. *et al.* Bi-directional tuning of thermal transport in $SrCoO_x$ with electrochemically induced phase transitions. *Nat. Mater.* **19**, 655-662 (2020).

Acknowledgements

I have spent five and a half years at Hokkaido University. I would like to thank everyone who used to be or being during my years in Japan.

Firstly, I would like to show my deepest gratitude to my supervisor Prof. Hiromichi Ohta for his guidance. Without his support and encouragement both in my research work and in my life, I could not accomplish this thesis. His persistent exploration of scientific questions, rigorous attitudes on details as well as enthusiasm towards scientific research really inspired me. I learned the right attitude as a researcher from him, it will always be helpful to me in the future.

I really appreciate my thesis committee, Prof. Seiya Kasai, Prof. Tamotsu Hashizume, Prof. Megumi Akai for their valuable advice and support.

I also would like to thank every professor and collaborator who helped me. I am grateful to Prof. Yuichi Ikuhara (U. Tokyo), Prof. Bin Feng (U. Tokyo) and Prof. Jiake Wei (U. Tokyo) for their STEM observations, Prof. Hyoungjeen Jeen (Pusan Nat'l U.) and Dr. Joonhyuk Lee (Pusan Nat'l U.) for XAS and magnetism measurements. Without their kind helps and discussions, I could not finish my thesis.

Of course, this thesis would not be possible without help from every Lab member who used to be or is still at Prof. Ohta's laboratory. I would like to thank Prof. Tsukasa Katayama for all comments and advice on the weekly lab meeting. I would like to give my deep gratitude to Prof. Hai Jun Cho for all discussions and comments in my research work. I really benefit a lot from his patient explanation and countless help on every problem I faced. I am truly grateful to Prof. Yuqiao Zhang (Jiangsu U.). I was so lucky to join Prof. Ohta's group when he was still a lab member. Thanks for teaching me all the manipulation of facilities in the laboratory, for all discussions and encouragements, for listening to my complaints. I will not forget the driving time to Wakkanai and Shiretoko with him and Dr. Ang Tao. Dr. Takaki Onozato (OB), thanks for all things I learned from him. Mr. Binjie Chen, I was always enjoyed having lunch and discussing my questions with him every time, his kindness and knowledge really impressed me. Dr. Xi Zhang, discussing with her inspired and encouraged me a lot, I really learned a lot. Dr. Doudou Liang (USTB), I was really enjoyed driving with her on weekends, her kindness and excellent experiment skills impressed me. Dr. Mian Wei (OG), thanks for her kindness, I will always remember her warm hug that really encouraged me. Prof. Anup Kumar Sanchela (Assistant Professor, Pandit Deendayal Petroleum Univ.), Dr. Gowoon Kim (OG), Mr. Yuzhang Wu, Mr. Lizhikun Gong, Mr. Yugo Takashima (OB), Mr. Liao Wu, Mr. Rui Yu, and Mr. Takashi Fujimoto who really enriched me both in work and in my life, thanks for their countless help. I really spent a wonderful time with them. I also want to thank bachelor students who joined Prof. Ohta's group for teaching me Japanese.

Of course, I would like to deeply thank previous supervisor Prof. Shinichi Kikkawa and Prof. Yuji Masubuchi. I could not come to Japan without their support.

Next, I want to thank my friend, Ms. Xinnan Liu. I was so lucky to meet her at Hokkaido University. Thanks for her accompany during our part-time job, for support in all things, for listening to my complaints in different things, I will always remember our traveling time in Kyushu and Hokkaido. I really really spent a wonderful time with her in Japan.

Lastly, I want to thank my parents, younger brother, and especially, my grandparents for their love, support, and understanding during these years. They always support me unconditionally in every decision I made. Their encouragements have always been the driving force to my study and life when I lost confidence. Thanks for making me who I am today.

A part of my research was financially supported by the Japan Society for the Promotion of Science (JSPS, DC2, 21J1004201).

Qian Yang

Sapporo, Japan

2022.03

List of Publications

(1) **Qian Yang***, Joonhyuk Lee, Hyoungjeen Jeen, Hai Jun Cho, and Hiromichi Ohta*, "Solid-State Electrochemical Protonation of $SrCoO_{2.5}$ into $H_xSrCoO_{2.5}$ (x = 1, 1.5 and 2)", **ACS Appl. Electron. Mater.** 3, 3296–3300 (2021).

(2) **Qian Yang***, Hai Jun Cho, Hyoungjeen Jeen, and Hiromichi Ohta*, "Solid-State Electrochemical Redox Control of the Optoelectronic Properties for $SrFeO_x$ Thin Films", **J. Appl. Phys.** 129, 215303 (2021).

(3) **Qian Yang**, Joonhyuk Lee, Bin Feng, Yuichi Ikuhara, Gowoon Kim, Hai Jun Cho, Hyoungjeen Jeen*, and Hiromichi Ohta*, "Unusually large thermopower change from +330 μV K^{-1} to -185 μV K^{-1} of brownmillerite $SrCoO_{2.5}$", **ACS Appl. Electron. Matter.** 2, 2250-2256 (2020).

(4) **Qian Yang**, Hai Jun Cho, Hyoungjeen Jeen*, and Hiromichi Ohta*, "Macroscopic visualization of fast electrochemical reaction of $SrCoO_x$ oxygen sponge", **Adv. Mater. Interfaces** 6, 1901260 (2019). **Outside back cover**, **Press released**

Other papers

(1) Xi Zhang*, Gowoon Kim, **Qian Yang**, Jiake Wei, Bin Feng, Yuichi Ikuhara, and Hiromichi Ohta*, "Solid-State Electrochemical Switch of Superconductor-Metal-Insulators", **ACS Appl. Mater. Interfaces** 13, 54204-54209 (2021). **Press released**

(2) **<u>Qian Yang</u>**, Yuji Masubuchi*, Mikio Higuchi, “Synthesis of perovskite-type oxynitrides $SrNb(O,N)_3$ and $CaTa(O,N)_3$ using carbon nitride”, **Ceram. Int.** 46, 13941-13944 (2020).

List of Presentations

(1) **Qian Yang**, Joonhyuk Lee, Hyoungjeen Jeen, Hai Jun Cho, and Hiromichi Ohta, "Solid-State Electrochemical Protonation Induced Phase Transition from $SrCoO_{2.5}$ into $H_xSrCoO_{2.5}$ (x = 1, 1.5 and 2)", 薄膜材料デバイス研究会 第 18 回研究集会 in 京都, オンライン, 2021.11.11-12. (Oral) スチューデントアワード

(2) **Q. Yang**, H.J. Cho, H. Jeen, H Ohta, "Solid-state electrochemical redox control of the optoelectronic properties for $SrFeO_x$ thin films", 第 82 回 応用物理学会秋季学術講演会, online, 2021.9.10-13. (Oral)

(3) **Q. Yang**, J. Lee, H. Jeen, J. Wei, B. Feng, Y. Ikuhara, H.J. Cho, and H. Ohta, "Electrochemical Redox reaction of $SrCoO_{2.5}$ films using YSZ oxide ion conductor", 2021 年 第 68 回 応用物理学会春季学術講演会, online, 2021.3.16-19. (Oral)

(4) **Qian Yang**, Joonhyuk Lee, Hyoungjeen Jeen, Bin Feng, Yuichi Ikuhara, Hai Jun Cho, and Hiromichi Ohta, "Solid-state Electrochemical Protonation/Oxidation of $SrCoO_x$ Films", Electronic Materials and Applications 2021 (EMA2021), virtual, Jan. 19-22, 2021. (Oral)

(5) **Q. Yang**, J. Lee, H. Jeen, B. Feng, Y. Ikuhara, H.J. Cho, and H. Ohta, "Realization of $SrCoO_2$ epitaxial films by electrochemical reduction using YSZ solid electrolyte", 第 56 回 応用物理学会北海道支部/第 17 回日本光学会北海道支部合同学術講演会, online, 2021.1.9-10. (Oral)

(6) **Qian Yang**, Joonhyuk Lee, Hyoungjeen Jeen, Bin Feng, Yuichi Ikuhara, Hai Jun Cho, and Hiromichi Ohta, "Electrochemical Redox Control of $SrCoO_x$ Epitaxial Films using YSZ as the Solid Electrolyte (P44)", The 21st RIES-Hokudai International Symposium 間 [ma], online, December 10-11, 2020 (Poster). **Poster Award**

(7) **Qian Yang**, Joonhyuk Lee, Hyoungjeen Jeen, Bin Feng, Yuichi Ikuhara, Hai Jun Cho, and Hiromichi Ohta, "Electrochemical Protonation/Oxidation of $SrCoO_{2.5}$ Films using CAN as the Solid Electrolyte", 薄膜材料デバイス研究会 第 17 回研究会「薄膜デバイスの原点」, November 5-6, 2020. (Poster)

(8) **Qian Yang**, Hai Jun Cho, Hyoungjeen Jeen, Hiromichi Ohta, "Electrochemical Manipulation of the Electron Transports of $SrCoO_x$ Epitaxial Films", Pacific Rim Meeting on Electrochemical and Solid State Science (PRiME 2020), October 4-9, 2020. (Poster)

(9) **Qian Yang**, Bin Feng, Yuichi Ikuhara, Hyoungjeen Jeen, Hai Jun Cho, Hiromichi Ohta, "Solid-State Electrochemical Protonation/Oxidation of Oxygen Sponge $SrCoO_{2.5}$ Films", 2020 年 第 81 回応用物理学会秋季学術講演会, online, September 8-11, 2020. (Oral)

(10) **楊 倩**, Hai Jun Cho, Hyoungjeen Jeen, 太田裕道, "情報記憶材料 $SrCoO_x$ 薄膜における電気化学酸化反応の巨視的可視化", 化学系学協会北海道支部 2020 年冬季研究発表会, 北海道大学（北海道, 札幌市）, 2020 年 1 月 28 日-29 日. (Oral)

(11) **楊 倩**, Hai Jun Cho, Hyoungjeen Jeen, 太田裕道, "熱電特性と導電性 AFM による $SrCoO_x$ の電気化学反応の巨視的可視化", 第 55 回応用物理学会北海道支部/第 16 回日本光学会北海道支部合同学術講演会, 北海道大学（北海道, 札幌市）, 2020 年 1 月 11 日-12 日. (Oral)

(12) **Qian Yang**, Joonhyuk Lee, Bin Feng, Yuichi Ikuhara, Gowoon Kim, Hai Jun Cho, Hyoungjeen Jeen, and Hiromichi Ohta, "Thermopower detection of electronic structure modulation of $SrCoO_{2.5}$ film on lattice mismatched substrates", The 3rd Workshop on Functional Materials Science, Sapporo, Japan, December 18th-20th, 2019. (Poster)

(13) **Qian Yang**, Hai Jun Cho, Hyoungjeen Jeen, and Hiromichi Ohta, "Macroscopic visualization of fast electrochemical reaction of $SrCoO_x$ oxygen sponge", RIES-NCTU Workshop, Hokkaido University, Sapporo, Japan, December 3-4, 2019. (Poster)

(14) **Qian Yang**, Hai Jun Cho, Hyoungjeen Jeen, and Hiromichi Ohta, "Macroscopic visualization of fast electrochemical reaction of $SrCoO_x$ oxygen sponge", The 20th RIES-HOKUDAI International Symposium, Hokkaido University, Sapporo, Japan, December 2-3, 2019. (Poster)

(15) **楊 倩**, Hai Jun Cho, Hyoungjeen Jeen, 太田裕道, "$SrCoO_x$ 酸素スポンジの高速電気化学反応の巨視的可視化", 令和元年日本セラミックス協会　東北北海道支部研究発表会, 新潟大学工学部, 新潟県新潟市, 2019 年 11 月 8 日-9 日. (Oral)

(16) **楊 倩**, ジョ ヘジュン, Joonhyuk Lee, 馮 斌, 幾原雄一, Hyoungjeen Jeen, 太田裕道, "ブラウンミラライト型 $SrCoO_{2.5}$ 薄膜の異常熱電能", 令和元年日本セラミックス協会　東北北海道支部研究発表会, 新潟大学工学部, 新潟県新潟市, 2019 年 11 月 8 日-9 日. (Poster). 優秀発表賞

(17) **Qian Yang**, Hai Jun Cho, Hyoungjeen Jeen, Hiromichi Ohta, "Anomalous Thermopower Behaviour of Brownmillerite $SrCoO_{2.5}$ Epitaxial Films", 26th International Workshop on Oxide Electronics (iWOE26), Kyoto, Japan, September 29 – October 2, 2019. (Poster)

(18) **楊 倩**，Hai Jun Cho，Hyoungjeen Jeen，太田裕道, “$SrCoO_{2.5}$ エピタキシャル薄膜の電気化学酸化と電子輸送特性”, 2019 年 第 80 回応用物理学会秋季学術講演会, 北海道大学 札幌キャンパス, 北海道札幌市, 2019 年 9 月 18 日-21 日. (Ora

List of Awards

(1) **Student Award** “Solid-State Electrochemical Protonation Induced Phase Transition from SrCoO2.5 into HxSrCoO2.5 (x = 1, 1.5 and 2)”,薄膜材料デバイス研究会 第18 回研究集会 in 京都, online, November 11-12, 2021.

(2) **Poster Award** “Electrochemical Redox Control of $SrCoO_x$ Epitaxial Films using YSZ as the Solid Electrolyte (P44)”, The 21st RIES-Hokudai International Symposium 間[ma], online, December 10-11, 2020.

(3) **優秀発表賞** “ブラウンミラライト型 $SrCoO_{2.5}$ 薄膜の異常熱電能”, 令和元年日本セラミックス協会 東北北海道支部研究発表会, 新潟大学工学部, 新潟県新潟市, 2019 年 11 月 8 日-9.

List of Patent

(1)太田裕道, 楊 倩, ジョ ヘジュン, 「熱トランジスタ」, 特願 2021-164181, 2021 年 10 月 5 日 出願